Fraunhofer-Institut für Photonische Mikrosysteme
Dresden

The Optical Outcoupling of Organic Light Emitting Diodes

Presented as part of the requirements for a Doctorate in Natural Sciences
(Doctor rerum naturalium)

Fachrichtung Physik
Fakultät Mathematik und Naturwissenschaften
Technische Universität Dresden

June 2008

Sumbitted By

Duncan Hill

Thesis Examination Committee:

Prof. Dr. Karl Leo
Prof. Dr. Hubert Lakner
Dr. Armin Wedel

Table of Contents

List of Figures

List of Tables

Publications

- K. Schmidt and K. Leo and D. Hill ”Lichtemittierendes Bauelement”; Patent application DE 10 2004 037 096.6-33, (2004)
- D. Hill and K. Leo and J. Amelung ”Leuchteinrichtung mit Organischer Leuchtdiode”, Patent application, (2005)
- D. Hill, K. Leo, G. He and Q. Huang ”Analysis of spatial coherence of organic light-emitting devices through investigation of interference effects observed in top-emitting devices”; *Appl. Phys. Lett.* **90, (2007)**

Chapter 1

Introduction

While electroluminescence in organic materials was first observed in the 1960s, there was a long hiatus until the first practical devices were produced. Since the first production of a multilayer OLED [1], running within a realizable range of parameters for a commercial device, there has been significant development into methods of improving the properties of the devices for use in both lighting and display applications. In both small molecule and polymer OLED devices[2] much of the focus has been, and remains on device production techniques such as spin coating, etching and Vacuum Deposition. A number of methods have been proposed, such as the Vertical In-line Deposition system at the Fraunhofer IPMS[3], as well as small and large scale evaporation and cluster chambers with various methods of sample transport. The chosen materials are also of critical importance for a variety of reasons, from minimizing the cost of the devices, through mechanical properties as well as electrical and optical properties. Choice of materials is also driven by the deposition method, since certain methods cannot deposit certain materials in any practical way, thus increasing costs where these materials are chosen, since multiple techniques must be used in order to build the device, requiring several machines. An example is that spin coating cannot be used to deposit ITO, so polymer devices require that the substrate is first coated with ITO and then transported to the spin coater to deposit the materials, and transported to a vacuum chamber again for deposition of the metal cathode.

The electrical charge transport properties have historically been one of the major points of concern, since thicker layers typically result in deteriorated device performance as a result in the rise in resistance of the layers, meaning that the trade off between enhancing the optical properties of the device and enhancing the electrical properties was complex. More recent work however in the addition of dopants [4] to the organic layers has allowed the better tailoring of the layers to improve the charge transport. For polymers, the aim is to reduce this issue through complex mixing of monomers giving the polymer chains a number of useful properties. These have allowed a much larger range of layer properties and vastly improved the capability of improvement of the optical properties by altering the layer stack structure.

Another issue of critical importance is the efficient use of the excitons within the OLED. The excitons formed within the emission layer may be in either singlet or triplet states, but as the OLED materials contain fluorophores, they may only emit from the singlet states. Since the probability of formation of the singlet or any one of the three triplet states is equal, then 75% of excitons may be lost in this way. Due to the weak spin-orbit coupling in OLED molecules, and the strongly forbidden nature of singlet-triplet transitions, energy in the triplet state is almost all transferred into heat. There is much work, such as the addition of transition metals to induce spin-orbit coupling to mix the states and allow the generation of photons, however this results in red-shifted emission, making blue light more difficult to achieve.

Currently the majority of OLEDs are built on glass or quartz substrates. These materials both provide the rigidity required during deposition, and also good barrier properties against water and air, which rapidly degrade the OLED stack materials. Both the OLED layer stack and the substrate affect the optical emission properties of the OLED devices. The emitters in small molecules are typically isotropic and homogeneous in their properties, but the confining nature of the OLED stack strongly affects the emission properties, both in terms of magnitude, direction and colour. The substrate then further affects the emission properties, principally through wave guiding, in which a significant proportion of the light may be lost within the glass and wasted. Some 80% of the light may be lost through the various device limitations, strongly decreasing the potential efficiency of

OLEDs, and it is the subject of this thesis to address this large loss in light.

This thesis analyses the effects of the layer stack properties on the OLED (Chapter 4); layer thicknesses, material choice in terms of anode and cathode and other issues related to the thin film stack, using a matrix matching method. For the analysis of the substrate and solutions to wave guiding problems, a ray tracing approach has been used (Chapter 5). Solutions to problems and further research are proposed (Chapter 6). A number of out coupling problems have not been considered here, such as losses due to plasmon propagation and wave guiding in the OLED layer.

Bibliography

[1] C.W. Tang and S. Van Slyke. Organic electroluminescent diodes. *Appl. Phys. Lett.*, 51:913, 1987.

[2] J.H. Burroughes, D.D.C. Bradley, A.R. Brown, R.N. Marks, K. MacKay, R.H. Friend, P.L. Burns, and A.B. Holmes. Light-emitting diodes based on conjugated polymers. *Nature*, 347:539, 1990.

[3] M. Schreil, M. Eritt, J. Amelung, K. Leo, U. Hoffmann, and M. Bender. OLED devices manufactured using a vertical inline concept. *SID Symposium*, 35:1376, 2004.

[4] X. Zhou, M. Pfeiffer, J.S. Huang, J. Blochwitz-Nimoth, D.S. Qin, A. Werner, J. Drechsel, B. Maennig, and K. Leo. Low-voltage inverted transparent vacuum deposited organic light-emitting diodes using electrical doping. *Appl. Phys. Lett.*, 81:922, 2002.

Chapter 2

OLEDs and Optics

Organic LEDs are semiconductor light-emitting devices whose emitting materials are built around chains or rings of carbon, as opposed to inorganic elements such as Indium and Silicon, seen in conventional LEDs. This allows for a large range of chemicals to be chosen, whose properties can be picked in order to optimize the device according to requirements such as lifetime, brightness and colour, and can be further tailored to match other electrical requirements such as hole transport ability.

While electroluminescence in organic semiconductors was reported as early as the 1960s [1], it was not until the 1980s that significant development began to take place driven through the work of Tang and Van Slyke [2], who developed a four layer OLED consisting of Indium-Tin-Oxide (ITO), TPD, Alq_3 and a Mg/Ag cathode. Electroluminescence was first reported from conjugated polymers in 1990 [3], and since then OLED technology has diversified along the two main paths of polymer and small molecule devices. OLEDs have many benefits over current lighting and display technologies, such as incandescent lamps, CRT displays, LCD displays and inorganic LEDs. LCDs are currently the main competitor to OLED technology in the display market, and are now rapidly expanding into televisions and monitors, pushing out CRT displays. LCDs work on the principle of blocking polarised light, either transmitted through the display in the case of backlit displays, or reflected light (Fig: 2.1). This structure is far more complex than OLEDs, which do not require

the polarizing and other layers (Fig: 2.2), though these may be added to OLED displays to improve contrast and outcoupling. The disadvantage of using LCDs is that since the light passing through the emitter must be polarized, there is an immediate loss of 50% of the light for unpolarised light sources. This loss increases when colour filters are added in order to produce colour LCD displays. Furthermore, the entire display must be backlit, even the pixels which appear dark.

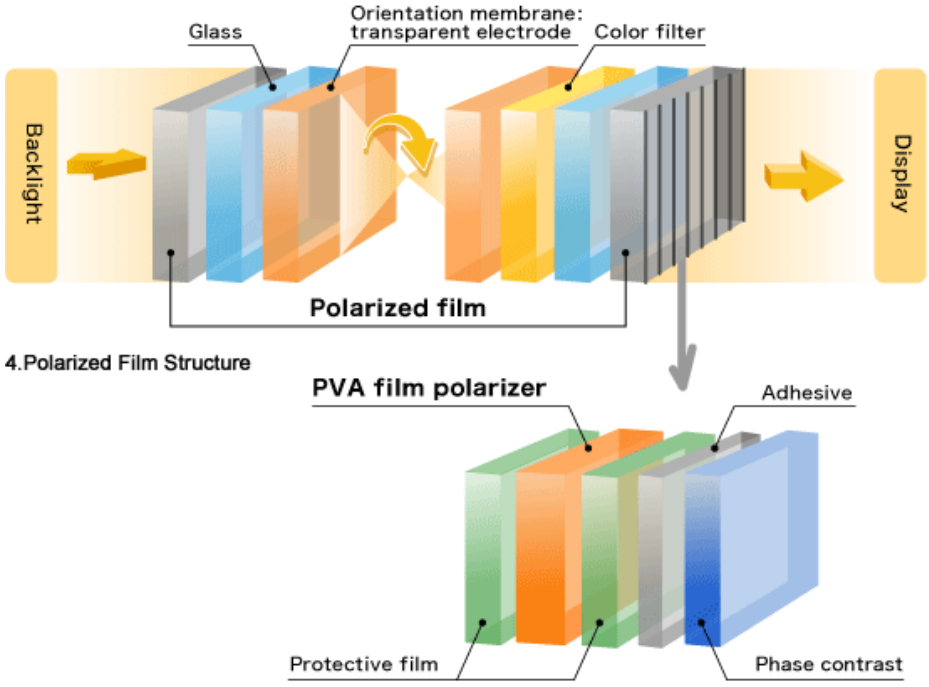

Figure 2.1: Schematic of LCD layer structure

LCD displays also often suffer from directional problems, in that colours and images are strongly distorted at higher angles, though this can be limited somewhat through the use of directional filters, which are becoming increasingly effective. More exotic LCD displays are now even capable of showing multiple images in the left and right visual field [4]. Despite their limitations however, LCD displays are a rapidly growing market in the display sector, with the recent rapid growth of flat screen monitors and other devices as a result of active matrix technology (conventionally called TFT or Thin Film Transistor) technology, which allows for direct control of each pixel, allowing for much more rapid pixel updating leading to much better portrayal of motion and improved colour

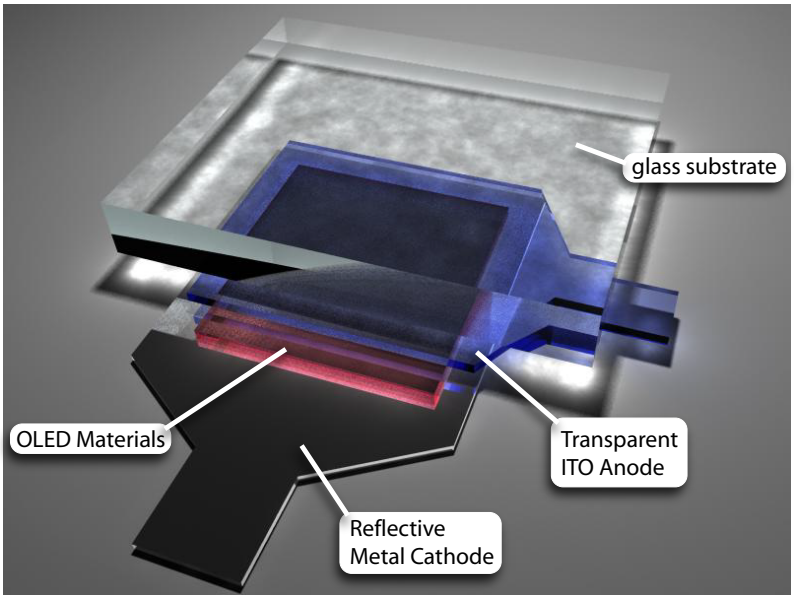

Figure 2.2: OLED structure

and resolution. TFT LCD displays are rapidly becoming the display of choice for a wide range of consumer display devices.

The drop in efficiency due to the loss of light is a particular problem for portable devices such as laptops, mobile phones and gaming devices, as the monitor can consume up to a third of the power of the device as a whole and the ability to reduce the power drain of the display would result in significant battery lifetime extension for the device. OLEDs are a suitable candidate as a solution to this problem as the light does not require polarization, and colour filters are not required, since the OLEDs can emit different colours directly. Additionally the pixel density can be increased using novel arrangements of OLEDs such as the Stacked OLED [5], in which OLEDs of different colours are deposited directly on top of one another, rather than side by side as in normal displays, meaning that the light of each colour is emitted from the whole pixel area, rather than just $^1/_3$ of it. In addition, whereas for a backlit LCD the entire display is lit all the time, and unwanted light is cut out by the LCD filter, for an OLED display, only the active pixels need to be lit. For a screen in typical video mode, this corresponds to a power consumption of approximately 25% of a full white display.

OLED displays can also be designed in both passive matrix, on which the pixels are lit using a strobing row-column format, and active matrix, where each pixel is individually addressed by a transistor. Many currently available commercial OLED systems in mobile phones and low information displays such as those in portable MP3 players are passive matrix, however active matrix technology is being developed and is a growing sector.

2.1 Types of OLEDs

OLEDs can be grouped into two main classifications, molecular and polymer OLEDs. Molecular OLEDs consist of small molecules such as 8-hydroxyquinoline aluminium (Alq_3) (Fig: 2.3) These

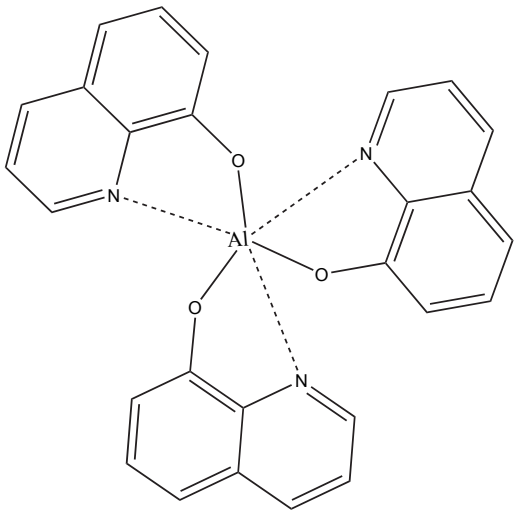

Figure 2.3: Molecular Diagram of Alq3

are principally deposited through thermal deposition processes in a vacuum chamber, with a heater subliming the material from a source onto a substrate. There are a number of deposition technologies, from batch processing such as in standard lab vacuum chambers and cluster tools, through vertical in-line fabrication systems. Different molecules can be sublimed into either adjacent or mixed layers, adjusting the optical and electrical properties of the structure. In general, the optical and electrical properties of small molecules are more tightly constrained than for polymer OLEDs.

In order to overcome this, it is possible during sublimation to mix the molecules with dopants to adjust the electrical and optical properties of the materials. Polymer OLEDs (Fig: 2.4) consist of molecular chains, the entire structure of which can be tailored by choosing subsections with different optical and electrical properties. These polymers may be constructed from a number of different monomer units and side chains, and in a variety of manners, for example block copolymers, consisting of alternating blocks of the same monomer unit covalently bound to blocks of a different monomer unit. Production processes for polymer OLEDs are wide ranging, from batch processes

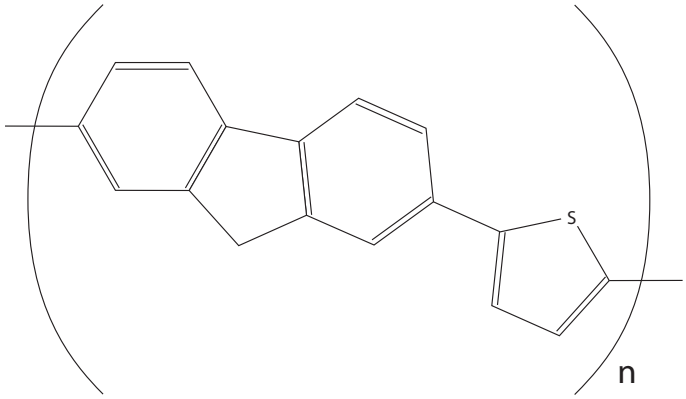

Figure 2.4: Molecular Diagram of a Fluorine-Thiophene polymer

such as spin coating, in which the polymer is dissolved in a solvent which is then dropped onto the substrate and spun at a certain speed in order to reach the required properties, such as thickness, through Ink-Jet printing [6] and reel to reel processing, which would allow continual production line processing, potentially leading to a dramatic increase in output. In all cases, the polymer is first dissolved in an appropriate solvent, and then deposited onto the substrate, either already patterned as in the case of the Ink-Jet, or to be patterned later by photolithography. This strongly limits the numbers and types of layers that can be built up; after a polymer layer has been deposited and dried out, the polymer or material of the next layer must not be dissolved in a solvent that will dissolve the first layer, since this will destroy the device. Although this technique results in a high amount of wasted polymer, spin coating is an extremely cheap deposition method, and is suitable for producing large area devices. The limitation on the number of layers remains a problem, as

it reduces the amount of control over the electrical properties of the device. The pixel resolution of the devices is also often much lower. Lifetime is also another major issue for polymers. Blue lifetimes are currently very short - only 1000 hours at 200cd/m^2. This compares with > 5000 hours for small molecule LEDs and 50,000 hours for conventional inorganic LEDs, though there has been a steady increase. The short lifetime of blue emitters is due to the high energy photons breaking the links between the monomers. Recent work however has suggested the use of the polymers as a charge transport mechanism, with the emission coming from small molecule dopants, leading to devices which can capitalize on many of the advantages of both OLED types. Currently, the large majority of commercially available devices are made from small molecule OLEDs, and they are regarded as technically superior in terms of their display properties, as is clear from their greater market penetration. Prototypes of large OLED displays have been seen in both small molecule and polymer OLEDS, produced by Samsung and Seiko-Epson respectively, and both with a diagonal measurement of 40".

2.2 Current problems facing OLED technology

The efficiency of OLED devices, while in principle much better than for the other display types mentioned above, still faces a number of limitations that have to be overcome. Some possible sources for losses of efficiency include charge injection at the cathode/anode boundaries between the organic and inorganic layers, charge transport within the organic materials, with carriers being lost to imperfections in the devices such as trap states, the photoluminescent efficiency and the outcoupling efficiency between the device and air, as well as electrical and optical effects of vatiation in layer thickness. Other issues rest on the mechanical and environmental properties of OLED displays. Currently, in order to maintain efficient electron injection, the cathode is commonly made from materials such as magnesium, which rapidly corrode when exposed to air. Other materials such as aluminium, which becomes stable after developing a surface oxide layer, may be used, but the cathode must have a low work function in order to ensure efficient electron injection, or

additional layers such as lithium fluoride must be added to improve electron injection [7]. The OLED materials themselves are also vulnerable to exposure to oxygen and air, and hence it is necessary to isolate the display from the atmosphere and where possible include a dessicant in order to remove any unwanted elements that leak in through edges or through the encapsulating materials. When protection from environmental factors is inadequate, there may be a number of failure modes, but the most common are dark spot formation, pixel shrinkage, and device shorts (Fig: 2.5) where spikes of material cut through multiple layers.

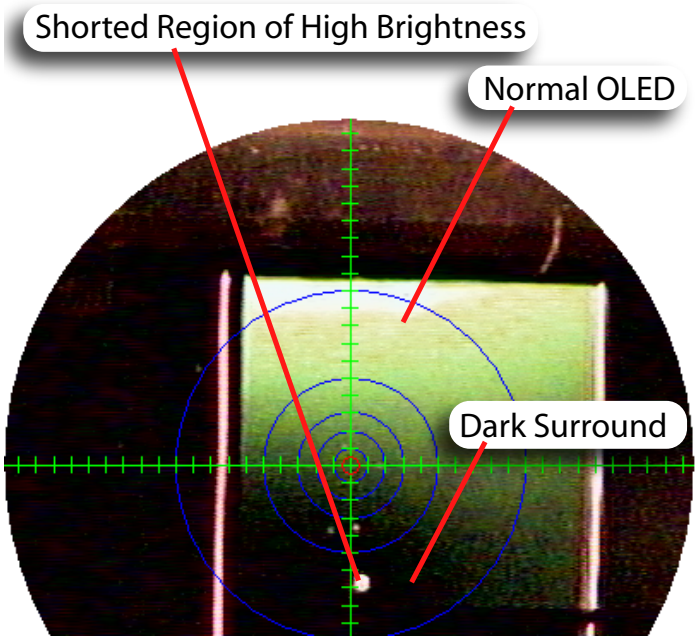

Figure 2.5: Device Short Resulting in Partial Pixel Destruction

This is currently a major limitation to one of the proposed future uses of OLEDs; flexible displays. The materials that are available for flexible displays include thin glass, which is a good barrier material, but suffers from manufacturing difficulties, through metals and plastic, which would be ideal in terms of production, but is currently some ten million times more permeable to oxygen and water than glass [8]. Currently it is possible to make some limited flexible displays, such as curved, but fixed plastics seen in sports watches, and the recent flexible clock manufactured by Citizen, that

employs e-Ink electronic paper [9, 10]. Possible markets for flexible displays are already emerging, and being exploited using inorganic LED technology, such as Philip's "Lumalive" textiles[11].

2.3 Structure of OLED devices

OLEDs typically consist of a number of layers of organic material deposited between a metal cathode and transparent anode, such as ITO (fig: 2.6). The basic structure can be divided into two types depending on which direction the light is emitted relative to the substrate on which the OLED is built - bottom emitting (BE) and top emitting (TE) OLEDs. BE OLEDs emit through the substrate, which is typically glass or Quartz based. A transparent anode such as ITO is first deposited onto the substrate and then the organic layers are sublimed, and finally the metal cathode for electron injection is deposited, before the whole device is encapsulated. Encapsulation isolates the OLED from air, leaving only the electical contacts exposed, and lengthens the device lifetime. The structures of the devices between the anode and cathode can vary from very simple devices [2], through to more complex devices including electron and hole transport and blocking layers, and multiple emitting layers.

2.4 Optics of OLEDs and Displays

2.4.1 Light Detection in the Human Eye

Light is detected by the eye when the photons strike and are absorbed by opsins, which are embedded in the surface membranes, discs (in the rods) and the invaginations in the cones (Fig: 2.7. The opsins contain 11-cis-retinal (sometimes called 11-cis-retinene), which isomerizes and changes shape when it absorbs light, causing a cascade of reactions within the cell, resulting in a hyperpolarization of the cell membrane, which causes a drop in the neurotransmitters released at the synapses. There are two basic cellular types in the eye, the rods, which are not used for discrimination between different colours, and are distributed around the edges of the eye, and the cones, which consist of

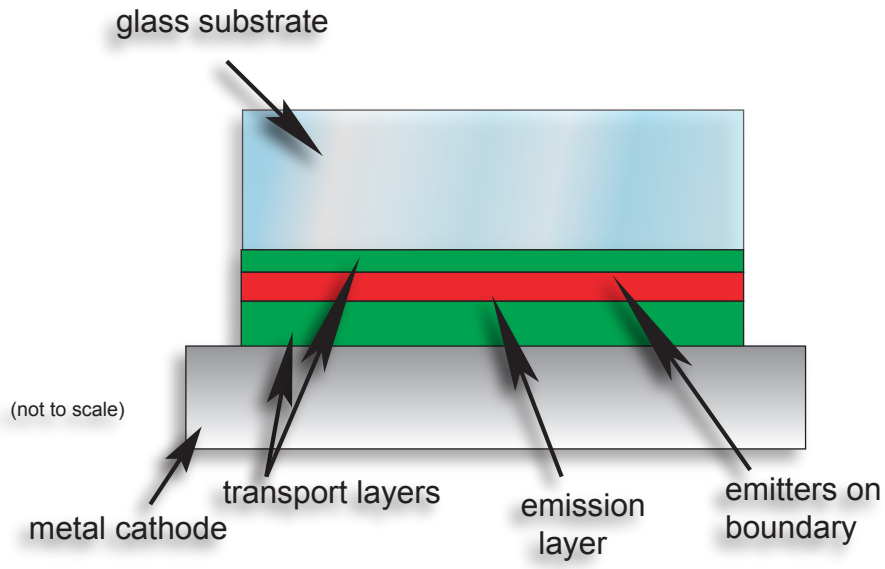

Figure 2.6: Schematic Representation of Bottom Emitting OLED stack

three different types with different opsins, and are most highly concentrated in the fovea, in the center of the eye's field of vision. The different opsins affect the wavelengths which can be absorbed by the 11-cis-retinal, meaning that certain cones can better detect red, others green and blue respectively. After some preprocessing in the retina to improve light/dark contrast, certain colour effects and a variety of other properties, the signals are then sent to the brain. The responsivity of the cones to different wavelengths of light can be measured, and from this the gamut, or range of colours that the human eye can detect. Rods are not taken into account in this calculation, since they are not present in the fovea, and are linked together slightly differently in order to detect lower light levels, but with a corresponding loss of resolution. Quantitative studies of the absorption properties of the eye were carried out as early as the 1930s, resulting in the CIE (Commision Internationale de L'Eclairage) colour matching functions (fig: 2.8[1]). These show the response for the light adapted (photopic) response. The dark adapted (scotopic) response is slightly different, and will not be considered here. The curves can be treated as a probability of absorption for each wavelength, so a "red" opsin is more likely to absorb red light than blue light, but it can still absorb blue light albeit

[1]Image obtained from http://www.wikipedia.com. Further info in Appendix D

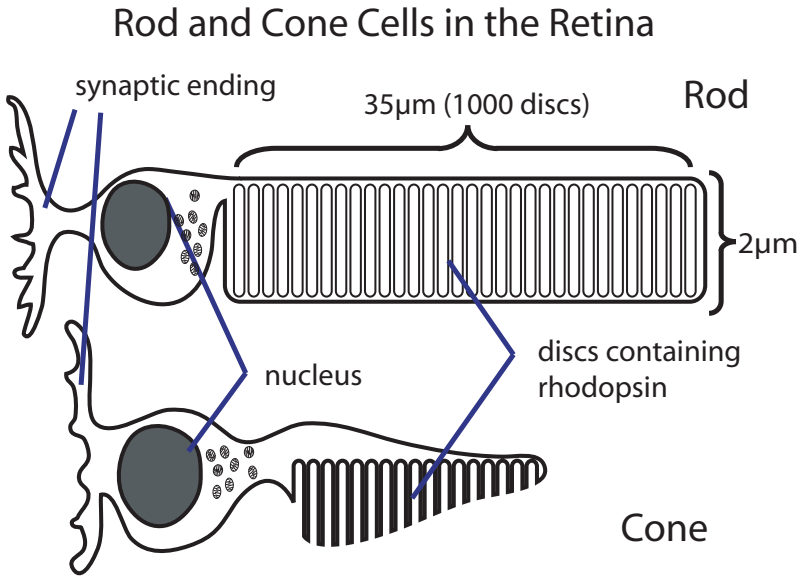

Figure 2.7: Schematic of the rods and cones in the eye

with lower probability, and thus trigger an impulse. However the different firing rates of the different cones allow the brain to determine the colours which nearby cones are absorbing. These response curves can then be used to determine the range of colours and brightnesses detected by the eye, the so-called colour gamut (Fig: 2.9[2]).

2.4.2 Displays and Colour Gamut

Colour displays typically consist of three emitters of different basic colours, at different points in the gamut, one in the red, green and blue. Different proportions of emission from the emitters can allow the display to simulate a wide range of colours within the triangle formed by their emissions (Fig:2.10[3]). The two main display ranges for commercial televisions are known as NTSC, and PAL, both having different colour gamuts (Table: 2.1). Other displays such as LCD displays have different gamuts depending on the emitters or colour filters chosen. The colour coordinate of an emitter can be determined through convolution of the colour matching functions with the emission spectrum of

[2]Image obtained from http://www.wikipedia.com. Further info in Appendix D
[3]Image obtained from http://www.wikipedia.com. Further info in Appendix D

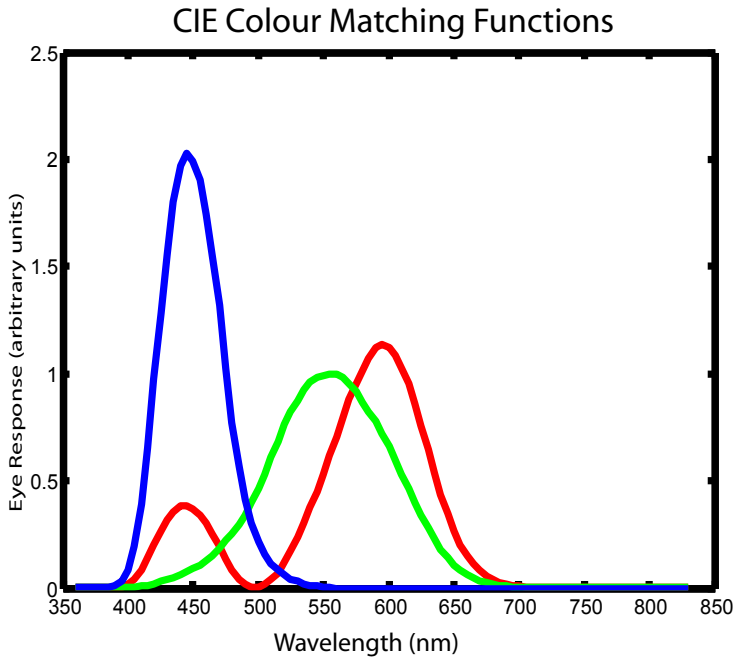

Figure 2.8: The CIE Colour Matching Functions.

the emitter. Despite having rather broad emission spectra, OLEDs can display an excellent colour gamut and high saturation.

2.5 Optical Properties of OLEDs

Since their discovery in the 1960s, red and green LEDs (and other longer wavelengths, such as infra-red) rapidly became very common. They were limited however in their use due to the lack of a good blue LED, which is required to display the full gamut of colours visible to the human eye. It was not until 1993 that a working blue LED was made by the Nichia Corporation, with widespread availability in the late 1990s. White LEDs can be made either through combination of a blue, red and green LED, alternatively, a blue Gallium Nitride (GaN) LED is coated with a yellowish phosphor such as cerium-doped Yttrium Aluminium Garnet ($Ce^{3+} : YAG$) which absorbs some of the blue light and converts it into a broad band emission centered on yellow. The strong blue peak

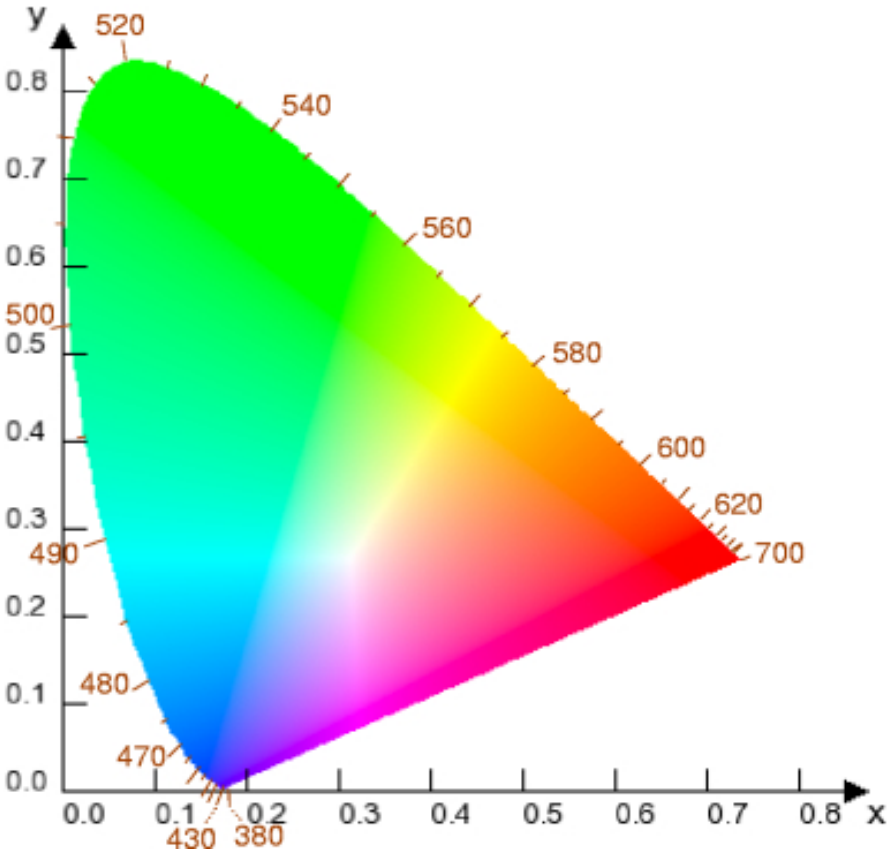

Figure 2.9: Total Gamut of the Human Eye.

however leads to a cold white dubbed as “Lunar White”. Other approaches however can improve the quality of the white. Recent developments are improving on this, for example coating a blue LED with a layer of quantum dots, to give a white much closer to that of an incandescent lamp [14]. LEDs however have not seen widespread use in high information content consumer displays since the pixels must be grown and individually deposited on the device, and there is often variation in the die leading to colour variations and the necessity to tune each pixel. They have seen widespread use as lighting sources, indicators, remote controls, low information displays such as clocks and some very large display screens, such as those seen in sports stadiums and in street advertising. There is still significant commercial investment into LEDs, with the production of LED lasers and high brightness LEDs[15]. Conventional LEDs such as InGaAs made from inorganic materials are

CIE Coordinates for Different Display Types		
ITU-R BT.709 Standard		
Colour	x	y
Red	0.64	0.33
Green	0.30	0.60
Blue	0.15	0.06
NTSC		
Colour	x	y
Red	0.67	0.33
Green	0.21	0.71
Blue	0.14	0.08
PAL		
Colour	x	y
Red	0.64	0.33
Green	0.29	0.60
Blue	0.15	0.06
OLED (IPMS OLEDs)		
Colour	x	y
Red	0.67	0.32
Green	0.35	0.60
Blue	0.15	0.19

Table 2.1: Common CIE Colour Coordinates[12, 13]

typically quite narrow band, with a FWHM of around 25nm (fig: 2.11[4]).

OLEDs however are broad band emitters, whose emission wavelengths can be more simply tailored through doping with different emitter molecules. Despite the broad band emission, they still give good saturated light, and can be used in devices with a wide colour gamut.

OLEDs as we have seen, consist of a series of layers deposited on a thick substrate, usually with one reflecting electrode as the cathode, and a transparent anode. Additional options for the cathode are available, such as Luxell's Black Layer Structure [16], which reduces reflection of incident light and improves contrast, but stops light recycling from light reflected or emitted toward the cathode. The layers are typically in the order of tens to hundreds of nanometers thick, and hence must be treated through explicit solution of Maxwell's wave equations for thin films. The substrate can be

[4]Image obtained from http://www.wikipedia.com. Further info in Appendix D

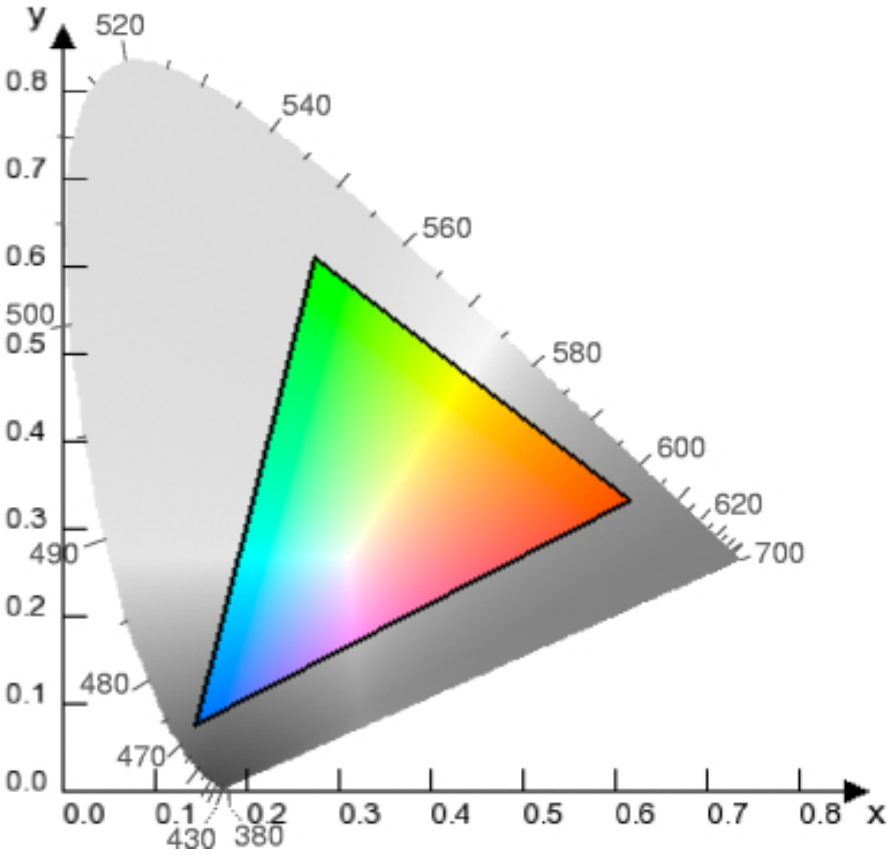

Figure 2.10: Gamut of a Typical CRT display.

treated as a thick layer, for which conventional ray optics is appropriate, on the condition that there are no additional diffractive structures or structures on the order of the wavelength of light, in which case these layers must be treated appropriately. Interactions with the surfaces can be treated simply with the use of the Fresnel Equations.

The emitters are embedded within the thin film structure, often close to a highly reflective cathode, and this alters the allowed emission modes. As OLEDs are broad band isotropic emitters, this can lead to strong angular dependence of intensity and strong angular effects on colour. When modelling the emitter, it is acceptable to treat the emitter as an oscillating dipole embedded within the thin film stack. The emission is then treated using typical thin film physics, treating the device as an optical microcavity, with the metal layer as infinitely thick, emitting into a semi-infinite emis-

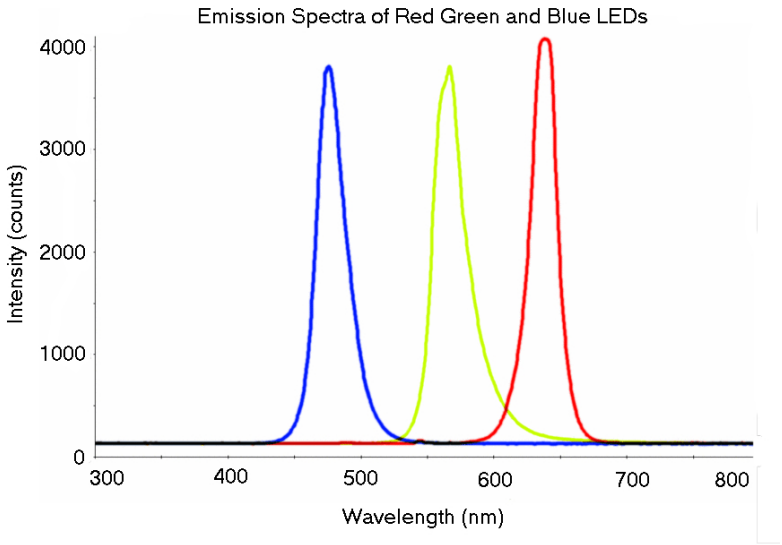

Figure 2.11: Comparison of Red, Green and Blue LED spectra.

sion zone, however the thickness of the device also creates an overall cavity, suppressing forward emission.

The major issues for OLEDs are emission from the high refractive index region of the OLED layer stack (typically with n=1.7) though the substrate (for glass, n=1.5) and into air (n=1) This creates a limited escape cone, with all the light outside the cone trapped in waveguided modes in the substrate and OLED itself. Those within the OLED are rapidly attenuated through repeated interference with the metal cathode, and those trapped with in the glass can easily propagate to the edges of the device

Additional layers are often required, such as passivation layers and encapsulation layers, in order to stop the encroachment of oxygen and water as described above.

Bibliography

[1] M. Pope, H. Kallmann, and P. Magante. Electroluminescence in organic crystals. *J. Chem. Phys.*, 38:2042, 1963.

[2] C.W. Tang and S. Van Slyke. Organic electroluminescent diodes. *Appl. Phys. Lett.*, 51:913, 1987.

[3] J.H. Burroughes, D.D.C. Bradley, A.R. Brown, R.N. Marks, K. MacKay, R.H. Friend, P.L. Burns, and A.B. Holmes. Light-emitting diodes based on conjugated polymers. *Nature*, 347:539, 1990.

[4] Sharp to mass produce worlds first LCD to simultaneously display different information in right and left viewing directions. Press Release, Jul 2005.

[5] S.R. Forrest, P.E. Burrows, Z. Shen, G. Gu, V. Bulovic, and M.E. Thompson. The stacked OLED (SOLED): A new type of organic device for achieving high-resolution full-color displays. *Synth. Met.*, 91:9, 1997.

[6] T.R. Hebner, C.C. Wu, D. Marcy, M.H. Lu, and J.C. Sturm. Ink-Jet printing of doped polymers for organic light emitting devices. *Appl. Phys. Lett.*, 72:519, 1998.

[7] L.S. Hung, C.W. Tang, and M.G. Mason. Enhanced electron injection in organic electroluminescence devices using an Al/LiF electrode. *Appl. Phys. Lett.*, 70:152, 1997.

[8] K.J. Allen. Reel to reel: Prospects for flexible displays. *IEEE Proceedings*, 93:1394, 2005.

[9] Citizen and eInk demonstrate portable bendable clock. Press Release, Dec 2005.

[10] Y. Chen, J. Au, P. Kazlas, A. Ritenour, H. Gates, and M. McReary. Electronic paper: Flexible active-matrix electronic ink display. *Nature*, 423:136, 2003.

[11] `http://www.research.philips.com/newscenter/archive/2006/060901-lumalive.html`.

[12] `http://www.w3.org/Graphics/Color/sRGB`.

[13] `http://www.dcs.ed.ac.uk/home/mxr/gfx/faqs/colorconv.faq`.

[14] M.J. Bowers, J.R. McBride, and S.J. Rosenthal. White-light emission from magic-sized cadmium selenide nanocrystals. *J. Am. Chem. Soc.*, 127:15378, 2005.

[15] `http://www.osram-os.com/ostar-lighting/index.php?lan=eng`.

[16] J.A. Dobrowolski, B.T. Sullivan, and R.C. Bajcar. Optical interference, electroluminescent device having low reflectance. United States Patent 5,049,780, September 1991.

Chapter 3

Emission Properties of OLEDs

3.1 Important Units

All light detection devices from photodiodes to the human eye have different responses to different wavelengths of light. When calculating the amount of light detected by a particular detector type, it is important to take this into account, so that the actual light incident on the detector can be calculated. The most fundamental units for measurement of light are the radiometric units, and these describe the power of the light in terms of basic physical units. Photometric units are adjusted by the response of the human eye, and are measured in terms of the Candela (Appendix F).

Overview of Key Units	
Radiometric Units	
Unit	SI Units
Spectral Radiance	$W \cdot sr^{-1} \cdot m^{-2} \cdot nm^{-1}$
Radiant Intensity	$W \cdot sr^{-1}$
Radiance	$W \cdot sr^{-1} \cdot m^{-2}$
Photometric Units	
Unit	SI Units
Luminous Flux	$cd \cdot m^{-2}$
Luminous Intensity	cd
Luminance	$cd \cdot m^{-2}$

Table 3.1: Overview of Units

3.2 Measurement of OLED emission properties

3.2.1 Measurement Devices

When considering the experimental measurement of possible outcoupling methods, it is important to determine the data that can be obtained from particular measurement methods, the limitations on these methods, and additional problems posed through the set-up of the devices. The light is collected and then transported to a device such as a photodiode connected to a diffraction grating, to collect a particular wavelength of light, or a CCD (Charge Coupled Device). These detectors can measure the radiometric properties of the device, such as radiant intensity ($W \cdot sr^{-1}$) and spectral radiance ($W \cdot sr^{-1} \cdot m^{-2} \cdot nm^{-1}$). Additional properties such as current, voltage, device area and angle are required to calculate key values, such as quantum efficiency. In order to calculate photometric properties such as luminous flux, the radiometric properties must be converted using the experimentally determined luminosity functions (Appendix: F). The main measuring tools for quantitative device measurements are typically a spectrometer mounted to a goniometer, and an integrating sphere, both of which typically collect light onto a CCD for measurement.

Goniometers allow the accurate measurement of angle, and consist of a rotational mounting which may be either manually or computer controlled. The detector may be mounted either directly on the rotating arm, or connected to it via a fibre optic cable (Fig: 3.1). This set-up has the advantage that it can measure the optical output at particular angles, and using this data, the output properties of the device can be measured, however assumptions have to be made when calculating efficiency, and also losses through waveguiding cannot easily be measured. Additionally there may be difficulties when measuring the light outcoupling from very thick substrates and structures which affect the focal points and distances of the goniometer. Typically the emission from an ordinary OLED on a flat substrate is assumed to be Lambertian, though since OLEDs often have a strong angular dependency due to the wide spectral width and the thin film structure, this assumption is not always valid. Through repeated measurements of luminance with angle, it is possible to develop a numerical fitness function, allowing a correct calculation of luminous efficiency from luminance values [1].

For further details, see Appendix A.2. This method allows for both the angular properties and spectral radiance properties to be measured, as well as the overall efficiency of the device, though is only valid for devices where the emission is circularly symmetric.

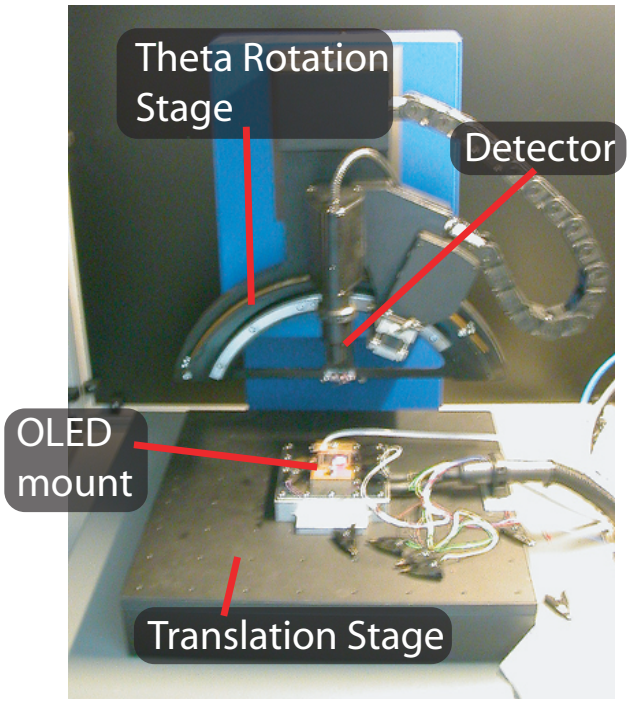

Figure 3.1: Autronic Melchers DMS 101 Goniometer Setup

Integrating spheres generally consist of a hollow sphere in with there is an aperture or mounting for the emitting component under investigation and another aperture for a detector. The inner surface of the sphere is coated with a diffuse broad spectrum reflective material, such as barium oxide. The multiple reflections allow capture of light emitted from the device into all angles onto the detector (Fig: 3.2), which is important for calculating the efficiency of the device. The disadvantage of this method however, is that detailed angular information is lost. Waveguided light (Fig:3.3) must be carefully treated in integrating spheres - if the edges of the glass are not covered, then waveguided light will be included in the overall emission efficiency of the device, which can result in overly optimistic readings.

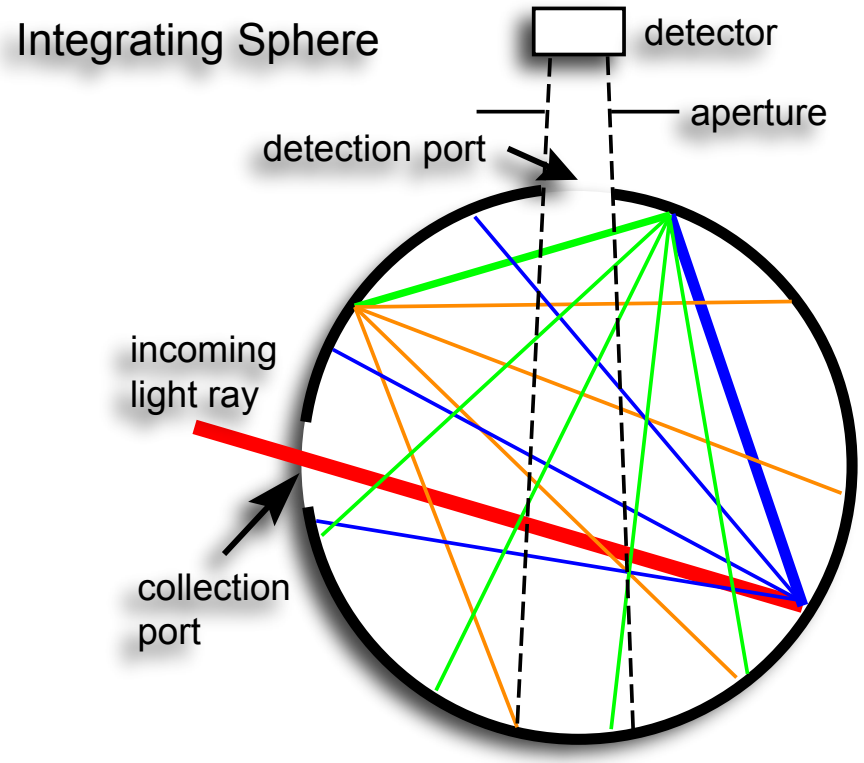

Figure 3.2: Typical Integrating Sphere setup

3.3 Understanding the Limitations of Outcoupling of Light from OLED Devices into Air

3.3.1 Substrate Outcoupling

Before dealing with the current progress in the field in outcoupling of OLED devices, it is important to determine the main areas in which light production and outcoupling are limited. The light is initially generated as a result of recombination of electrons and holes in the OLED molecules, and then takes a path through the OLED and is either emitted or lost. The measure of device efficiency is known as the Electroluminescent (EL) Quantum Efficiency η_{ext}. The ELQE can be found by combining the Radiation Luminous Efficacy K_r , a factor determined from the angular distribution

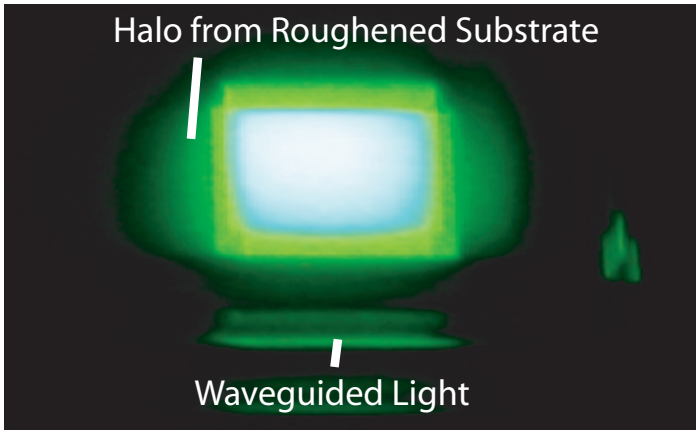

Figure 3.3: Waveguided Light Emitted from edge of OLED

of the light f_D and the current efficiency η_e

$$K_r = \frac{\Phi_V}{\Phi_e} = K_m \frac{\int_{380}^{770} \Phi_e(\lambda) V(\lambda) d\lambda}{\int_0^{\infty} \Phi_e(\lambda) d\lambda} \tag{3.1}$$

and

$$f_D = \frac{1}{\pi I_{v_I 0}} \int_0^{\pi/2} \int_{-\pi}^{+\pi} I_v(\theta, \phi) \sin\theta d\phi d\theta \tag{3.2}$$

where $I_{v_I 0}$ is the luminous intensity in the forward direction and $I_v(\theta, \phi)$ is the angular distribution of the light, which for a Lambertian is $\cos\theta$.

Combining these gives the Quantum Efficiency:

$$\eta_Q = f_D \pi \eta_e \frac{e}{K_p E_{mean}} \tag{3.3}$$

where E_{mean} is the average photon energy.

This value can also be treated as the product of the internal quantum efficiency ϕ_{int} and the outcoupling factor χ ($\eta_{ext} = \chi\phi_{int}$) [2]. Control of ϕ_{int} is primarily an electrical and material issue rather than an optical issue, though significant gains in ϕ_{int} have been demonstrated.

Once the light escapes the OLED structure, it will pass through the substrate and interact with

the boundaries according to Maxwell's Equations. The most simple treatment for a single interface results in Snell's Law and the Fresnel Equations [3] for the transverse electric and magnetic modes (Formulae 3.4 to 3.7).

$$r_{\perp} = -\frac{\sin(\theta - \theta')}{\sin(\theta + \theta')} \tag{3.4}$$

$$t_{\perp} = \frac{2\sin(\theta')\cos(\theta)}{\sin(\theta + \theta')} \tag{3.5}$$

$$r_{\parallel} = \frac{\sin(\theta')\cos(\theta') - \sin(\theta)\cos(\theta)}{\sin(\theta)\cos(\theta) + \sin(\theta')\cos(\theta')} \tag{3.6}$$

$$t_{\parallel} = \frac{2\sin(\theta')\cos(\theta)}{\sin(\theta + \theta')\cos(\theta - \theta')} \tag{3.7}$$

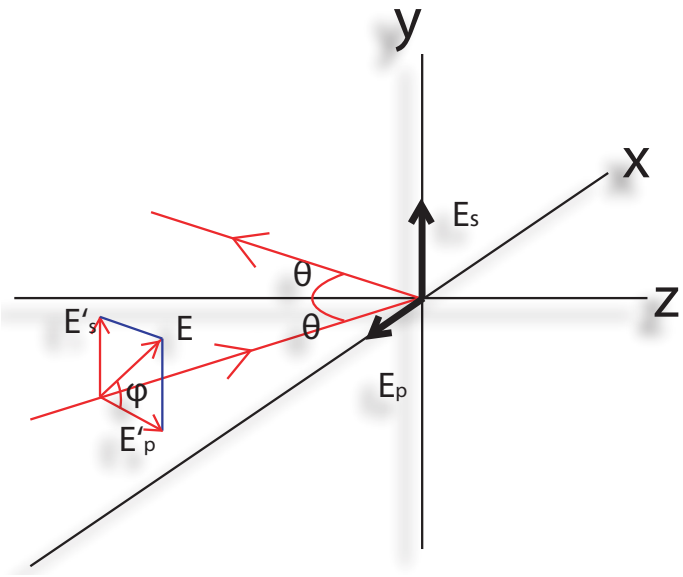

Fig 3.4 shows the perpendicular (s) and parallel (p) polarizations of the light incident in the x-y plane, interacting with a plane surface in the x-y plane. The s-polarised light is oriented such that its electric field component is perpendicular to the plane of incidence and p-polarized light with the electric field component in the plane of incidence. Light with its polarization oriented at an angle ϕ to the normal will have s and p components (E'_s and E'_p). s and p polarizations may also be referred to as Transverse Electric (TE) and Transverse Magnetic (TM) respectively.

Figure 3.4: Perpendicular and Parallel polarizations

Using these we can determine for a single planar interface and approximate maximum outcoupling for a Lambertian emitter. For an OLED of n=1.7, it is found that the outcoupling will be only

19% of the total emitted light. When considering multiple reflections from the interfaces emission will be slightly higher than predicted for a single pass. The amount of recycled light is highly dependent on the reflective qualities of the OLED stack itself, however all light emitted above the angle of total internal reflection will be lost for a totally planar device (Fig: 3.5). As a result, some 50-80% of the light can be lost to waveguiding in the device. For emission from a standard glass substrate ($n = 1.5$) into air ($n = 0$) the critical angle θ_c is 42^o. Outcoupling this light can lead to significant increases in overall efficiency, and a number of methods have been proposed.

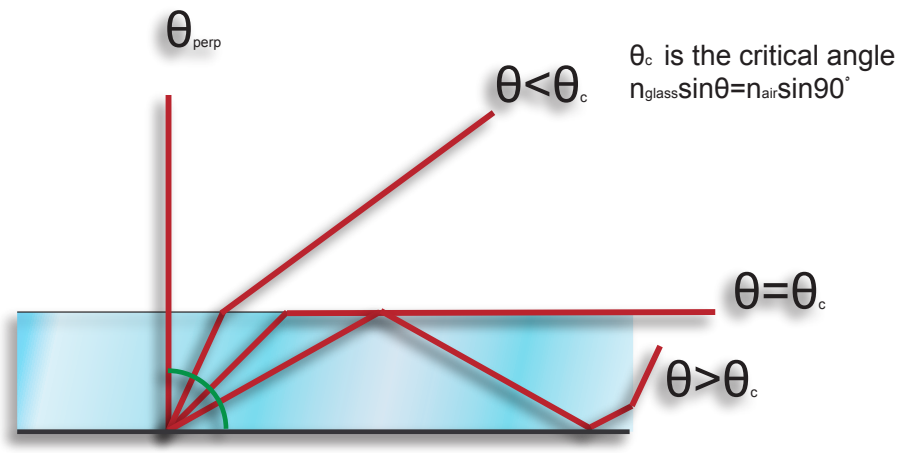

Figure 3.5: Waveguiding in OLED structure

3.3.2 Thin Film Stack Outcoupling

Outcoupling from the thin films is also an issue of critical importance. The light is emitted from within the stack, generally adjacent to a metallic cathode (for bottom emitting devices) which reflects some of the light back toward the substrate. As a result of this, interference can occur, influencing the emission, particularly in the forward direction. As the OLED is a broad band emitter, this will have different effects on different regions of the emission spectrum, depending on the particular device architecture. Additionally any refractive index mismatch between the OLED layers and the substrate can further exasperate the problem. Emitted light may also become locked to surface plasmons, forming polaritons which stop the outcoupling of this light [4].

3.4 Current Solutions to the Outcoupling Problems

There are a number of possibilities for improvement of outcoupling from the substrate to air, including refractive and holographic elements, scattering elements, and surface structuring.

3.4.1 Substrate Structuring

Substrate structuring is one possible method of light outcoupling for OLED displays. The main aim is to reduce the amount of light lost to internal reflections, by providing a number of alternate possible interaction angles (Fig: 3.6). When the light interacts with an interface, the reflected component stands a much higher chance of escape since the next interaction with the interface is likely to occur at a different angle, giving more opportunities for escape. If the light is multiply reflected however, it may eventually be lost to edge emission or be attenuated through absorption in the OLED and substrate layer. The difficulty with this possible solution is that the methods for manufacture of these

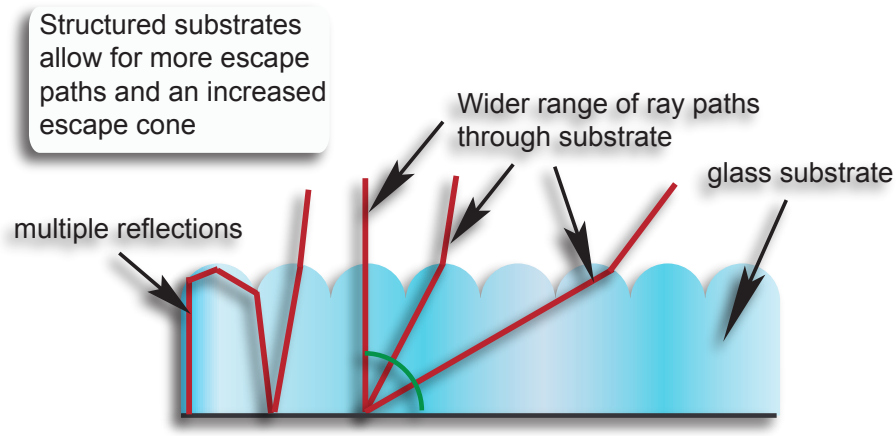

Figure 3.6: Multiple Reflections in Structured Substrate

structured substrates, which generally involve photolithography techniques such as the melting resist technique. These are costly and time consuming and so not ideally suited to mass production. A wide variety of potential structures have been investigated, from microlens arrays [5] to a range

of pyramid structures [6], prismatic structures and Fresnel Lenses.

3.4.2 High Index Substrates

It is found that a significant amount of light is trapped in the OLED structure itself, due to the refractive intensity mismatch between the OLED layer and the substrate n=∼1.7 and n=∼1.5 respectively. In principle it is possible to avoid much of this loss, by using high refractive index substrates such as flint glasses containing varying amounts of lead oxide, which also have low dispersion properties. The disadvantages of these however include higher cost and the necessity to use poisonous materials during manufacture, though the latter can be avoided by using alternate elements such as titanium dioxide and zirconium dioxide. One possible future opportunity of OLED devices is their production on flexible substrates, though currently use of these is limited due to them having poor barrier properties to oxygen and water and hence drastically shortening the lifetime. In general plastics have a similar refractive index to glass, in the region of 1.5, however again, there may be opportunity for producing high index substrates.

Used alone, no advantage is seen from using high index substrates, since while the light may be couple more efficiently from the OLED to the substrate, there is a corresponding decrease in coupling between the substrate and air, since the angle of total internal reflection is lower, and so the additional light is lost. Though use of additional methods of outcoupling, additional gains can be seen providing an overall advantage, since there are less sources of loss initially.

Use of a high refractive index substrate in the region, or higher than the index of the emitting layer results in a sharp increase in the amount of light coupled into the substrate, and with the use of microlens arrays etched directly onto the substrate, significant gains of 65% have been reported [5] with little effect on colour at high angles. Scattering effects are observed from these microlens arrays, but to date have not been quantified.

3.4.3 Outcoupling Films

There are a large range of commercial outcoupling films, with a number of different properties. These typically consist of a structured plastic layer which is attached to the surface of the substrate using a suitable adhesive to ensure good index matching. The structures are typically prismatic in nature, and as such there is a rotational asymmetry in their properties. The effect of these is described in the same manner as the structured substrates above, however there is inevitably more loss using films due to the additional reflections on the substrate-film interfaces. However the advantages of these over direct substrate structuring is lower cost, since these plastic films can be produced in large volumes. Flexible substrates, as mentioned in section 3.4.2 could quite easily combine the advantages of both since simpler stamping and roll techniques used in these outcoupling films could then be used directly on the substrate.

3.4.4 Holographic and Refractive Layers

The range of options offered by structured substrates is relatively limited, and fabrication of particular structures may be expensive and costly. An alternative possibility is the construction of holographic layers which form a diffractive layer that imitates the properties of a more complex structure. Holograms can initially be produced using conventional optical techniques (Fig: 3.7), then they can be produced as a stamp, through photolithographic methods, and finally mass produced and added to OLED devices. Recent research has shown some promise in coupling out additional light formerly lost to waveguiding [7] into forward directed light (Fig: 3.8) However some of the light emitted into the forward direction is then directed into a total internal reflected mode, though this can again be recovered on the next pass. This results in ghost images which appear to the sides of the OLED. The offset distance of the ghost images is proportional to the thickness of the substrate. Even in the absence of good outcoupling enhancement, it may still be possible to use this technique for illuminated signs.

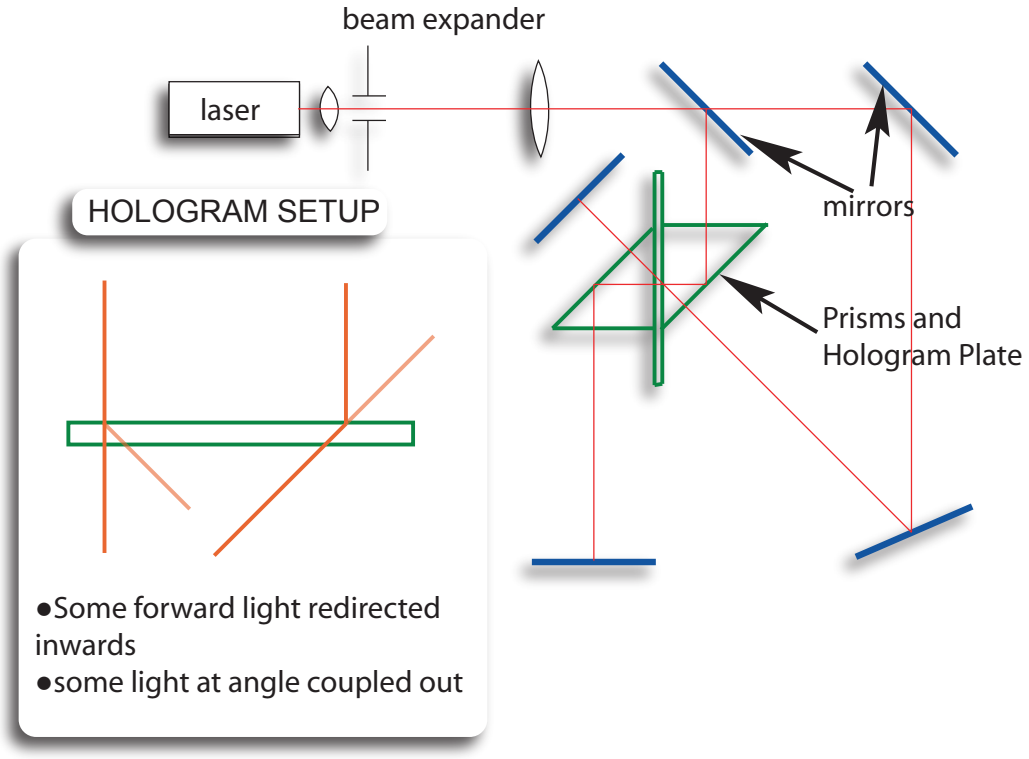

Figure 3.7: Basic Hologram Production

3.4.5 Additional Substrate Layers

There are two possible approaches to additional substrate layers. One is the addition of thin film layers as anti reflection coatings in order to reduce the amount of reflection on the surfaces. This is a well understood technique, which is commonly used lens coatings in order to ensure maximum transmission. Anti-reflection coatings however are in general strongly wavelength and angularly dependent, for the same reason as the OLED stack itself, and are not always appropriate. One possibility however is the use of "giant birefringent" structures, in which the difference in the refractive index between the different optical axes of one layer is of the order of the difference in refractive index between adjacent layers [8]. This can allow a much larger range of outcoupling layers to be produced. Inclusion of a very low refractive index element between the OLED and the substrate (Fig: 3.9) has been suggested [9] as a method of improving outcoupling for surface emissive

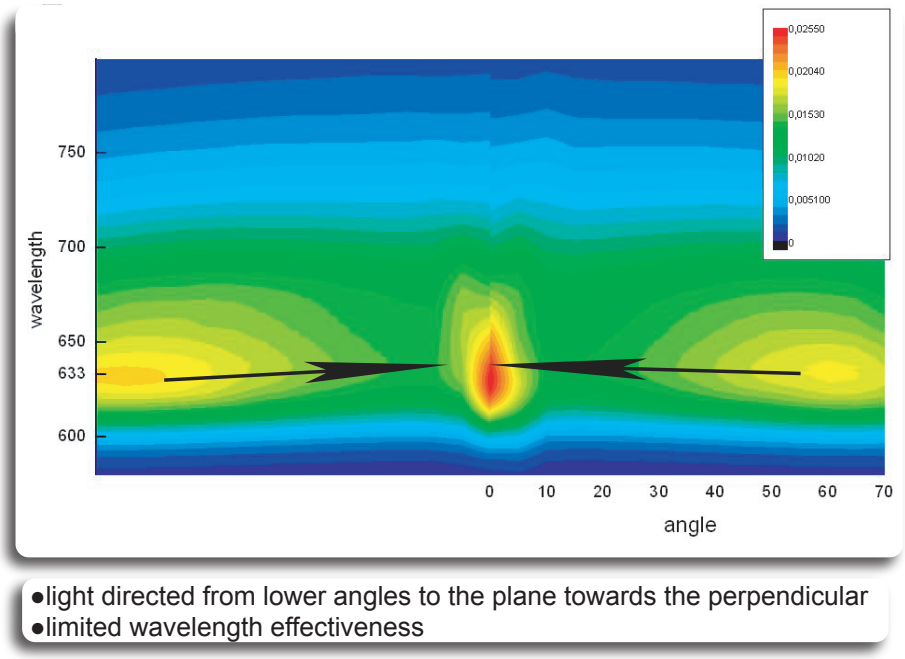

Figure 3.8: Enhanced forward light outcoupling with Holographic Layer.

devices. This would allow the light from the surface to be emitted into a low refractive material, bending it toward the normal, before entering the substrate and bending it away again. In principle this should eliminate almost all the light waveguided in the glass.

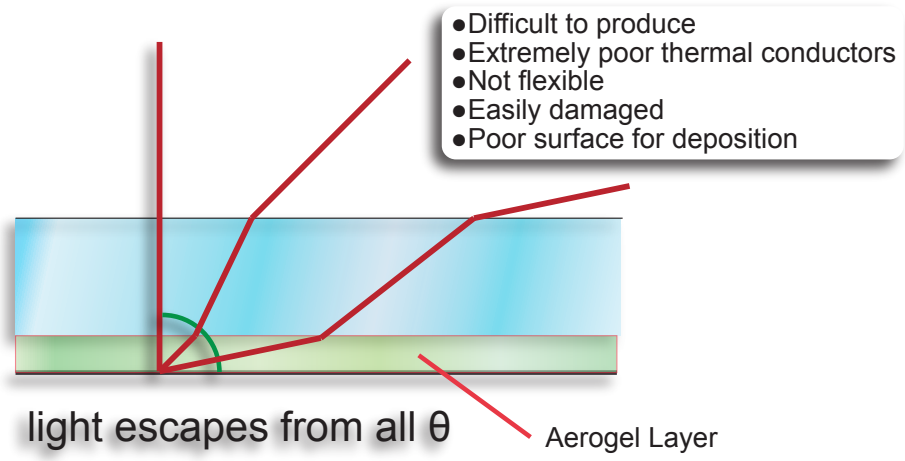

Figure 3.9: Inclusion of Aerogel Layer to enhance outcoupling

The main class of materials suitable for this are aerogels, which consist of a highly porous silica matrix containing air. Reports have found these aerogels to have refractive indices only a fraction above that of air. The difficulty with the use of these materials is that they are rigid, brittle, expensive to produce, difficult materials to deposit thin film layers on and while they are suitable for surface emission, they would increase the amount of light trapped in the OLED layer.

3.4.6 Optimization of the layer stack

The layer stack itself may be optimized to adjust the optical properties. However there is a complex interplay between the emission properties, the reflection properties and the electrical properties. In general as the thickness of the layers increases, the electrical properties deteriorate, due to increased sheet resistance. Correspondingly, layers that are too thin, may also suffer from penetration by local spikes in adjacent layers, resulting in electrical shorts, damaging the device properties. Use of dopants however can mitigate these problems [10], and with more complex layer structures, the emission can be controlled to a more defined region, allowing greater control over the optical emission zone. The peak emission zone occurs on the layer boundaries, typically on the boundary between the emitting layer and hole transport layers, since electron injection and transport is generally more efficient, leading to a surplus of electrons and a higher probability of them reaching this interface. Both theoretical and experimental studies have shown that the majority of the emission occurs in the 15nm of the emission layer closest to this boundary [11]. Careful positioning of this layer within the stack can increase outcoupling by adjusting the interference effects of the stack, such that constructive interference occurs in the forward direction. The largest benefit is seen when the peak of constructive interference occurs at the peak of electroluminescent emission. As with the addition of anti-reflection layers however, this method is in general not so suitable for light with a broad spectrum emitted over high angles. Addition of spacer layers can also be employed to control these optical properties without affecting the electrical properties of the layer stack itself. If required, this effect can also be used in order to tune the emission properties of the OLED.

3.4.7 Other Structures

Some recent work investigating the light emitting and reflecting properties of a number of biological organisms such as butterflies and squid has revealed some remarkable optical properties [12, 13, 14, 15] of photonic crystals. Indeed some of these structures are already in use in high brightness semiconductor LEDs [16] and as anti-reflection coatings. With further development and improved technology it may be possible to implement some of these features in future devices. This coupled with additional cathode patterning to reduce the losses to surface plasmons can result in further outcoupling improvements. Bragg scattering has also been reported by formation of periodic micro structures on the OLEDs [17]. These devices were made from polymer OLEDs which were spin coated onto a substrate corrugated with the desired Bragg grating. These structures strongly changed the emission, and an enhancement factor of 2 was reported.

3.5 Theory

3.5.1 Thin Film Theory

The theoretical understanding of optical outcoupling rests principally on solutions of Maxwell's equations with appropriate boundary conditions for each of the layer interfaces. Thin films are layers of the order of the wavelength of light, or thicker. For visible light this means in the range of 500nm. Since the OLED structure consists of a number of layers of the order of 10 - 100 nm thick, the OLED must be treated as a thin film stack. An additional layer of complexity is present as the emitting sources are contained within a thin film structure, with a metal interface nearby, built on an optically thick substrate. For small molecule OLEDs the directions of the emitters are in general regarded as isotropic, this is unlike polymer OLEDs which have a stronger preference for polarization and direction. The refractive index properties again, are generally regarded as homogeneous and isotropic for the former, and not necessarily so for the latter. This makes modeling of small molecule OLEDs simpler, since particular distributions of polarization do not occur within the emitting layer. For the purposes of modeling, it is possible to treat the emitters as oscillating

dipoles within a thin film stack [18]. The field is described by constructing a Green's function for the dielectric layer stack containing the emitters, and has been used to describe the changes in excitation lifetimes used in electroluminescent OLEDs. A classical treatment of this system has been well understood for some years [19, 20]. The system may also be treated quantum mechanically [21] however the disadvantage of the QM treatment presented, is that it cannot take into account non-radiative losses or absorption, the latter of which can affect the outcoupling.

3.5.2 Thick Substrate Theory

The substrates on which the OLEDs are built are typically of the order of micrometers to millimetres thick. In this regime we can ignore the wave nature of light and treat the light as rays, tracing their paths through the device and calculating the interactions on each interface. Since the substrates cannot be defined in terms of their phase thickness, this means that there can be no analytic solution, and so to determine the properties of the device, one must rely on numerical means. One example of this is the attempt to derive the amount of light output through a plane from a single surface. In this case the average transmission on the first pass can be calculated from the Fresnel coefficients, and also taking into account energy conservation on the surface

$$T_{av} = \left(\frac{n' \cos(\theta')}{n \cos(\theta)} \times \left(\frac{(2 \sin(\theta') \cos(\theta))^2}{\sin^2(\theta + \theta')} + \frac{(2 \sin(\theta') \cos(\theta))^2}{(\sin(\theta + \theta') \cos(\theta + \theta'))^2} \right) \right) / 2 \tag{3.8}$$

For a simple bottom emitting OLED we can calculate the total fraction of transmission T_T for a particular angle θ. The fraction of light initially passing through surface 2 is simply T_2, but some light R_2 is reflected to the substrate, reflected again R_1 and then may escape. So after the first pass, the amount of escaped light $T_T = T_2 + T_T R_1 R_2$. Repeated passes continually add more light:

$$T_T = T_2 + T_2 R_1 R_2 + T_2 {R_1}^2 {R_2}^2 + + T_2 {R_1}^3 {R_2}^3 + ... \tag{3.9}$$

which simplifies to

$$T_T = \frac{1 - R_2}{1 - R_1 R_2} \tag{3.10}$$

though more complex systems cannot be solved, since when calculating the reflection and transmission in even a three layer system (Fig: 3.10), we must find the amount of light from the adjacent layer, however the light from the adjacent layer is itself a function of the light in the layer being analysed, leading to equation sets which cannot be solved (Eqn: 3.12).

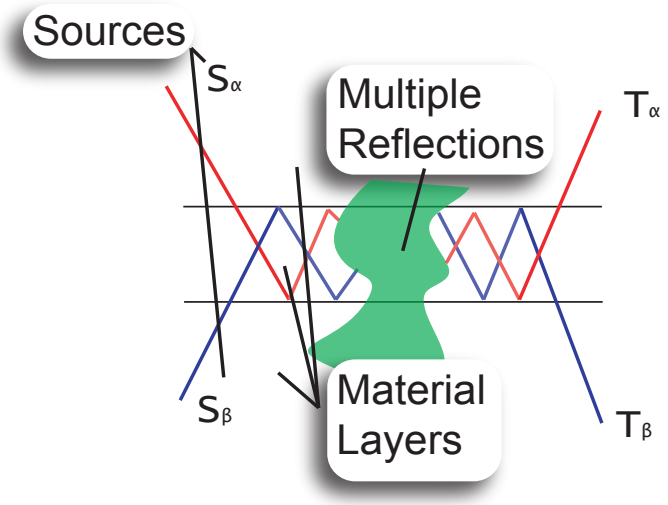

Figure 3.10: Reflection in Two Adjacent Thick Layers

$$R_T = \frac{S_1\left(T_\beta{}^2 R_\alpha + R_\beta - R_\beta{}^2 R_\alpha\right) + S_2 T_\alpha T_\beta}{\left(1 - R_\alpha R_\beta\right)} \tag{3.11}$$

$$T_T = \frac{S_2\left(T_\alpha{}^2 R_\beta + R_\alpha - R_\alpha{}^2 R_\beta\right) + S_1 T_\alpha T_\beta}{\left(1 - R_\alpha R_\beta\right)} \tag{3.12}$$

Where S_α and S_β are the light coming from the adjacent layers and T_α and T_β are the light transmitted from this layer into the outer layers respectively. For the outermost layers, only one source term exists. However, since the majority of the light within the escape cone can escape on

each pass, ray tracing rapidly approaches the real values for even small numbers of passes.

The above equations however can show some useful results for TE OLEDs. Typically top emitters must be covered by a glass encapsulation sheet for the reasons outlined in section 2.3. These themselves will reflect light back to the OLED, and this can, if not carefully controlled, damage the emission properties of the device as discussed in 4.8. We find that the fraction of light P reflected back to a substrate from a glass plate is

$$P = \frac{2R(1-R)}{1-R^2} \tag{3.13}$$

3.5.3 Ray Tracing

For a ray tracer, the light is given a vector, start location and an intensity. The ray is then traced through the device until it intersects with a surface. The coefficients of reflection and transmission (where it occurs) are calculated at the surface, along with the angles. This forms two new rays which are then propagated further using the same principles. The intensity of the light is split between the two new rays according the reflection and transmission coefficients. For more complex types of interaction, such as scattering, the initial ray can be split into a number of rays for further propagation. Accurate device descriptions can be extremely processor intensive, consisting of many interactions and many rays, however the use of Monte Carlo methods can be employed in order to reduce processor load, and hence time taken for the ray tracing of a full device. Monte Carlo methods use a pseudo-random sequence of numbers in order to take a statistical sample of a large number of possibilities, for example the emission location of each ray may be determined randomly, requiring a smaller number of rays to describe the total device output. This method can also be used for the modeling of substrates, where the perturbations on layer thickness are small compared to the mean layer thickness - one can even potentially model model non-random structures in this method. For example a square pyramid structure with a 90 degree apex has four possible surface normals, and the normal can be randomly chosen. Alternatively to lower the numbers of polygons and simplify the device description, techniques such as normal mapping can be used. A Normal

Map is a bitmap whose colour channels (R-G-B) each represent a perturbation to the surface normal on which they are superimposed. Care has to be taken with these perturbation techniques though, since they cannot deal with sequential interactions with the same layer interface (Fig: 3.11)

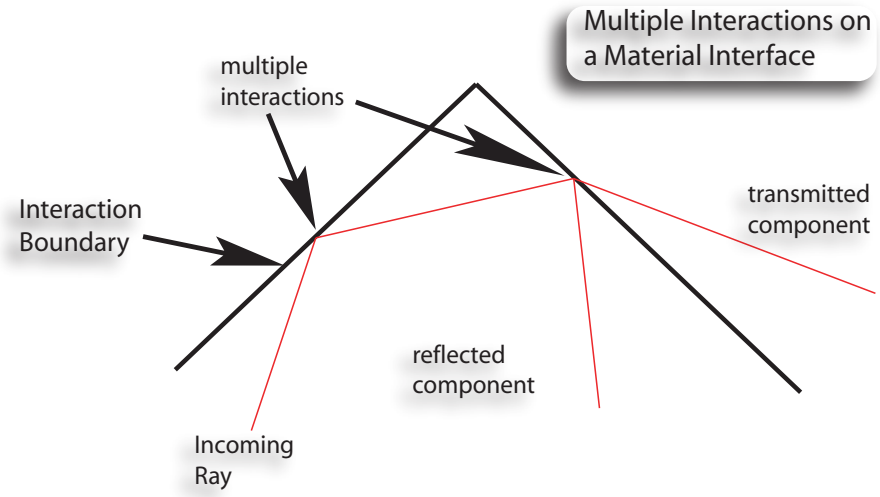

Figure 3.11: Multiple Interactions with the same Layer Interface

Where multiple interactions are expected to be rare, Normal Mapping and Normal Perturbations can be used. See Chapter 5 for more details.

Bibliography

[1] T. Tsutsui and K. Yamamato. Evaluation of true power luminous efficiency from experimental luminance values. *Jpn. J. Appl. Phys.*, 38:2799, 1999.

[2] M.H. Lu and J.C. Sturm. Optimization of external coupling and light emission in organic light emitting devices: modeling and experiment. *J. Appl. Phys.*, 91:595, 2002.

[3] E. Hecht. *Optics (4th (International) Ed.)*. Addison Wesley, 2002.

[4] P.A. Hobson, J.A.E. Wasey, I. Sage, and W.L. Barnes. The role of surface plasmons in organic light emitting diodes. *IEEE J. Selected Topics in Quantum Electronics*, 8:378, 2002.

[5] H.J. Peng, Y.L. Ho, C.F. Qiu, M. Wong, and H.S. Kwok. Coupling efficiency enhancement of organic light emitting devices with refractive microlens array on high index glass substrate. *SID Digest 04*, 1:158, 2004.

[6] S. Tanaka, Y. Kawakami, and Y. Naito. Improvement of the external extraction efficiency of OLED by using a pyramid array. *Proceedings of SPIE*, 5519:184, 2004.

[7] K. Schmidt, K. Leo, and D. Hill. Lichtemittierendes Bauelement. Patent application DE 10 2004 037 096.6-33, September 2004.

[8] M.F. Weber, C.A. Stover, L.R. Gilbert, T.J. Nevitt, and A.J. Ouderkirk. Giant birefringent optics in multilayer polymer mirrors. *Science*, 287:2451, 2000.

[9] T. Tsutsui, M. Yahiro, H. Yokogawa, K. Kawano, and M. Yokoyama. Doubling coupling-out efficiency in organic light emitting devices using a thin silica aerogel layer. *Adv. Mater.*, 13(8):1149, 2001.

[10] J. Blochwitz, M. Pfeiffer, T. Fritz, and K. Leo. Low voltage organic light emitting diodes featuring doped phthalocyanine as hole transport material. *Appl. Phys. Lett.*, 73:729, 1998.

[11] T. Granlund, L. Petterson, and O. Inganäs. Determination of the emission zone in single layer polymer light-emitting diode through optical measurements. *J. Appl. Phys*, 89:5897, 2001.

[12] P. Vukusic, J.R. Sambles, and C.R. Lawrence. Colour mixing in wing scales of a butterfly. *Nature*, 404:457, 2000.

[13] P. Vukusic, J.R. Sambles, C.R. Lawrence, and R.J. Wootton. Now you see it - now you don't. *Nature*, 410:36, 2001.

[14] P. Vukusic and I. Hooper. Directionally controlled fluorescence emission in butterflies. *Science*, 310:1151, 2005.

[15] W.J. Crookes, L.L. Ding, Q.L. Huang, J.R. Kimbell, J. Horwitz, and M.J. Mcfall-Ngai. Reflectins: The unusual proteins of squid reflective tissues. *Science*, 303:235, 2004.

[16] A.A. Erchak, D.J. Ripin, S. Fan, P. Rakich, J.D. Joannopoulos, E.P. Ippen, G.S. Petrich, and L.A. Kolodziejski. Enhanced coupling to vertical radiation using a two-dimensional photonic crystal in a semiconductor light-emitting diode. *Appl. Phys. Lett.*, 78:563, 2001.

[17] J.M. Lupton, B.J. Matterson, and I.D.W. Samuel. Bragg scattering from periodically microstructured light emitting diodes. *Appl. Phys. Lett.*, 77(21):3340, 2000.

[18] R.R. Chance, A. Prock, and R. Silbey. Molecular fluorescence and energy transfer near interfaces. *Adv. Chem. Phys.*, 37:1, 1978.

[19] P. Yeh. Electromagnetic propagation in birefringent layered media. *J. Opt. Soc. Am. (1917-1983)*, 69:742, 1979.

[20] O.H. Crawford. Radiation from oscillating dipoles embedded in a layered system. *J. Chem. Phys*, 89:6017, 1988.

[21] V. Bulovic, V.B. Khalfin, G. Gu, P.E. Burrows, D.Z. Garbuzov, and S.R. Forrest. Weak microcavity effects in organic light-emitting devices. *Phys. Rev. B.*, 58:3730, 1998.

Chapter 4

Modeling the Thin Film Structure of Organic LED Displays

4.1 Important Symbols and Quantities

The following tables outline the main symbols and quantities used repeatedly throughout this section. Where possible, consistency is maintained, though standard conventions take priority.

Symbols		
Symbol	Description	Unit
H	The Magnetic Field Strength	Am^{-1}
E	The Electric Field Strength	$Vm-1$
D	The Electric Displacement	Cm^{-1}
B	The Magnetic Induction	T
j	The Electric Current Density	Am^{-2}
ρ	The Electric Charge Density	Cm^{-3}
σ	The Electric Conductivity	Sm^{-1}
ϵ	The Permittivity of a Material	Fm^{-1}
μ	The Permeability of a Material	Hm^{-1}

Table 4.1: Important Symbols

Quantities		
Symbol	Description	Value
c	The Speed of Light in Vacuum	$2.99793 \times 10^{8} ms^{-1}$
μ_0	Permittivity of Free Space	$4\pi \times 10^{-}7 Hm^{-1}$
ϵ_0	Permeability of Free Space	$8.85 \times 10^{-12} Fm^{-1}$

Table 4.2: Important Quantities

4.2 Basic Overview

While the effects of thin film interference were observed by Hooke, Boyle and Newton in the 17th Century, it was not until 1801 that the wavelike nature was given a more solid grounding through analysis of interference effects by Thomas Young. Joseph Fraunhofer in 1817 was possibly the first to make anti-reflection coatings, though he did not appear to realize that the lower reflection that he observed would result in a higher transmission of light. In 1873 it was possible to understand in a more fundamental way the wave nature of light through the work of James Clerk Maxwell in "A Treatise on Electricity and Magnetism"[1]. In an isotropic medium, the integral form of the equations describing the electric and magnetic field are:

$$\oint_S D.dA = \int_V \rho.dV \tag{4.1}$$

$$\oint_S B.dA = 0 \tag{4.2}$$

$$\oint_C E.dl = -\frac{\partial}{\partial t} \int_S B.dA \tag{4.3}$$

$$\oint_C H.dl = \int_S J.dA + \frac{\partial}{\partial t} \int_s D.dA \tag{4.4}$$

$$j = \sigma E \tag{4.5}$$

$$D = \epsilon E \tag{4.6}$$

$$B = \mu H \tag{4.7}$$

From these we can also deduce the integral forms [2] These become much more complex for anisotropic media, as covered by Yeh [3]. For an Organic LED, whose construction consists of a number of thin film layers deposited on a thick substrate, it is necessary to describe the electromagnetic field explicitly, taking into account the field on each boundary. Due to the structure and varying refractive indices of the layers, it is critical that the various optical effects, from transmission and reflection, to frustrated total internal reflection and such, can be taken into account. As the film thicknesses are on the scale of the wavelength of light, and well understood, the thicknesses can be described in terms of the phase thickness, relative to each particular wavelength of light. In addition to the thin film stack, the OLED also consists of at least one reflective metallic interface, usually the cathode. The emitting region is centred on each molecule, and as such, the size of the oscillating region is very much smaller than the wavelength of light. This allows the oscillator to be treated as a point dipole. The effect of the nearby presence of a metallic layer on the temporal properties (fluorescence lifetime τ and oscillation frequency ω) of the oscillating dipole has been studied in depth [4]. While the lifetime of the dipole is not a concern for the optical properties of OLEDs, the effects on emission frequency are important and cannot be ignored. Once the effect of embedding within the thin film stack has been considered, the next step is to determine the effect of the stack on the radiated intensity $I_{N+1}(\theta, \phi)$. Having calculated these, the final emission properties of the OLED, and the field within the OLED itself can be determined.

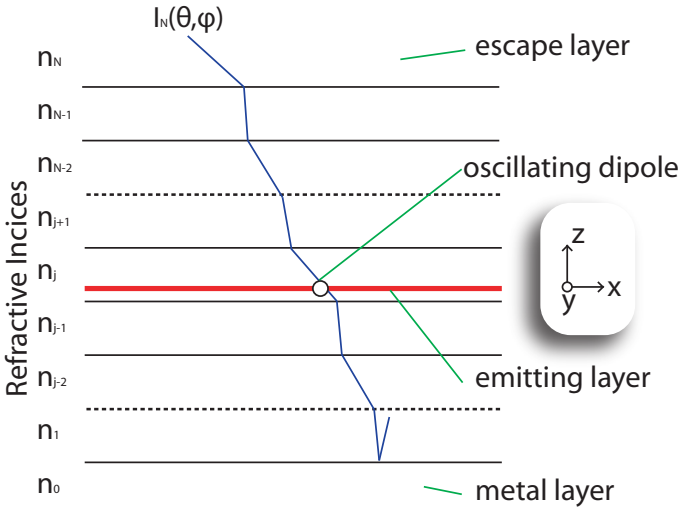

The oscillating dipole is embedded in the layer structure (region with refractive index n_j), which is surrounded by two semi infinite regions, the metallic cathode of index n_0 and surface substrate of index n_N. The effect of the layer stack has a strong effect on the emitted intensity $I(\theta, \phi)$. The OLED is treated as an infinitely large plane in the x and y directions.

Figure 4.1: The Layer Structure for OLED systems

4.3 Description of the Thin Film Stack

The same convention as described in Figure: 3.4 will be followed. For an isotropic medium, the relationship between $\hat{E}$ and $\hat{H}$ is fixed by [2]

$$\hat{H}_0 = \sqrt{\frac{\epsilon_r \epsilon_0}{\mu_r \mu_0}}\, \hat{s} \times \hat{E}_0 \tag{4.8}$$

where $\hat{s}$ is a unit vector in the direction of the plane wave propagation and is perpendicular to $\hat{E}$ and $\hat{H}$

taking $\mu_r = 1$ and $n = \sqrt{\epsilon_r}$ Equation 4.8 becomes

$$\hat{H}_0 = n \sqrt{\frac{\epsilon_0}{\mu_0}}\, \hat{s} \times \hat{E}_0 \tag{4.9}$$

from this, we can deduce the generalized refractive indices u_n for the s and p polarizations;

$$u_p = \frac{H_p}{E_p} = \frac{H}{E\cos(\theta)} = \frac{n}{\cos(\theta)} \tag{4.10}$$

and

$$u_s = \frac{H_s}{E_s} = \frac{H\cos(\theta)}{E} = n\cos(\theta) \tag{4.11}$$

The energy flow can now be described as

$$P_n = u_n E_n^2 \tag{4.12}$$

with the subscript n representing either 's' or 'p' as above.

With the exception of the semi infinite metal and emission layers, for a given wavelength of light, each emission layer j has a physical thickness d_j, a refractive index n_j. For light emitted into an angle θ the phase thickness g_j can be calculated by

$$g_j = k n_j d_j \cos\theta_j \tag{4.13}$$

where θ_j can be calculated using Snell's law. For metal layers, n_j is complex, and thus results in complex angles. Given that the interfaces are lossless, the sum of the incident and reflected electric field must be the same for both sides of the interface, i.e.

$$E_j = E_{j+1} = E_j^+ + E_j^- = E_{j+1}^+ + E_{j+1}^- \tag{4.14}$$

and similarly for the magnetic field component. Taking into account the relationship between the electric and magnetic field strengths allows us to find the matrix describing the details of the film in terms of effect on the propagation of light:

$$\begin{pmatrix} E_{j+1} \\ H_{j+1} \end{pmatrix} = \begin{pmatrix} \cos g_j & \frac{i}{u_j}\sin g_j \\ i u_j \sin g_j & cos g_j \end{pmatrix} \cdot \begin{pmatrix} E_j \\ H_j \end{pmatrix} \tag{4.15}$$

the 2x2 matrix $\left(M_j\right)$ relates the properties of light on one side of layer j to those on the other side of the film at $j+1$. Adding additional layers is simply achieved through the addition of further

matrices, and the properties of a number of layers can be combined through concatenation of the matrices.

$$\begin{pmatrix} E_0 \\ H_0 \end{pmatrix} = M_1 \cdot M_2 \cdots M_{N-2} \cdot M_{N-1} \begin{pmatrix} E_N \\ H_N \end{pmatrix} \tag{4.16}$$

This can then be used to calculate the field through the layer stack, when the field at some point is defined. For common thin film calculations, this is normally defined as the incident field, however in this case the sources of the field are embedded within the layer stack itself.

$$E^-_{qj} e^{\eta_j z_{j-1}} = t^{(j)}_{qij} E^-_{q1} e^{-\eta_1 z_1} + r^{(j)}_{qjj} E^+_{qj} e^{i\eta_j z_{j-1}} \tag{4.17}$$

$$E^+_{qj} e^{i\eta_j z_j} = r^{(N-j+1)}_{qj,j-1} E^-_{qj} e^{-\eta_j z_j} \tag{4.18}$$

for which q represents either the perpendicular ($\perp$) or parallel ($\|$) polarization (as described in Fig: 3.4).

4.4 Determining the nature of the Source Terms

In the description of the emitter, we must first consider the sources embedded within the layer stack. The sources consist of oscillating dipoles, of arbitrary orientation. The fields within the structure can be split into 's' and 'p' modes as previously described (Fig: 3.4). These will be indicated by the symbols $\perp$ and $\|$ respectively. Hence when describing the source terms, we do so in terms of the coupling between horizontal $\hat{P}_h$(where the direction of the polarization vector points in the plane of the OLED) or vertical $\hat{P}_v$ (where the orientation is parallel or anti-parallel to the OLED normal) dipoles (Fig:4.2), with the electrical components of the 's' $\hat{E}^{\perp}$or 'p' $\hat{E}^{\|}$ fields. When we consider the coupling of the electric field to the dipole, the coupling is proportional to the dot product $\hat{E}.\hat{P}$, so

$$\hat{E}.\hat{P} = \aleph \tag{4.19}$$

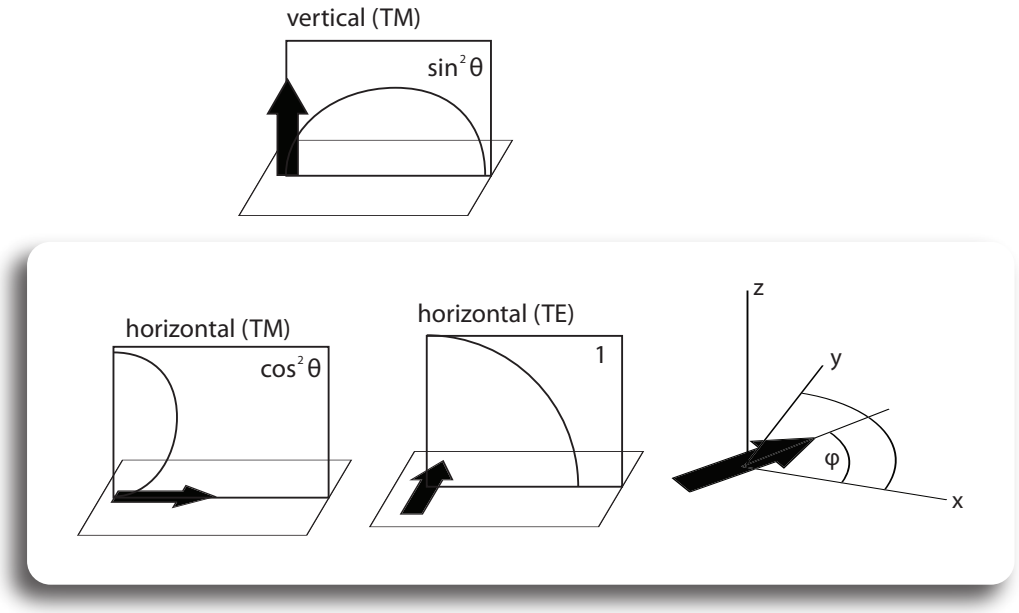

Figure 4.2: Schematic of dipoles and their electric fields

where $\aleph$ is a normalization factor. For the horizontal dipole, the coupling with the TE and TM modes is as follows:

$$\hat{E}^{\perp}.\hat{P}_h = \aleph_h \tag{4.20}$$

$$\hat{E}^{\parallel}.\hat{P}_h = \aleph_h \cos(\alpha) \tag{4.21}$$

and for the vertical dipole

$$\hat{E}^{\parallel}.\hat{P}_v = \aleph_v \sin(\alpha) \tag{4.22}$$

since the vertical dipole has no component in the x-y plane, and $E^{\perp}$ has no component in the z direction

$$\hat{E}^{\perp}.\hat{P}_v = 0 \tag{4.23}$$

These results are observed graphically in (Fig: 4.3)

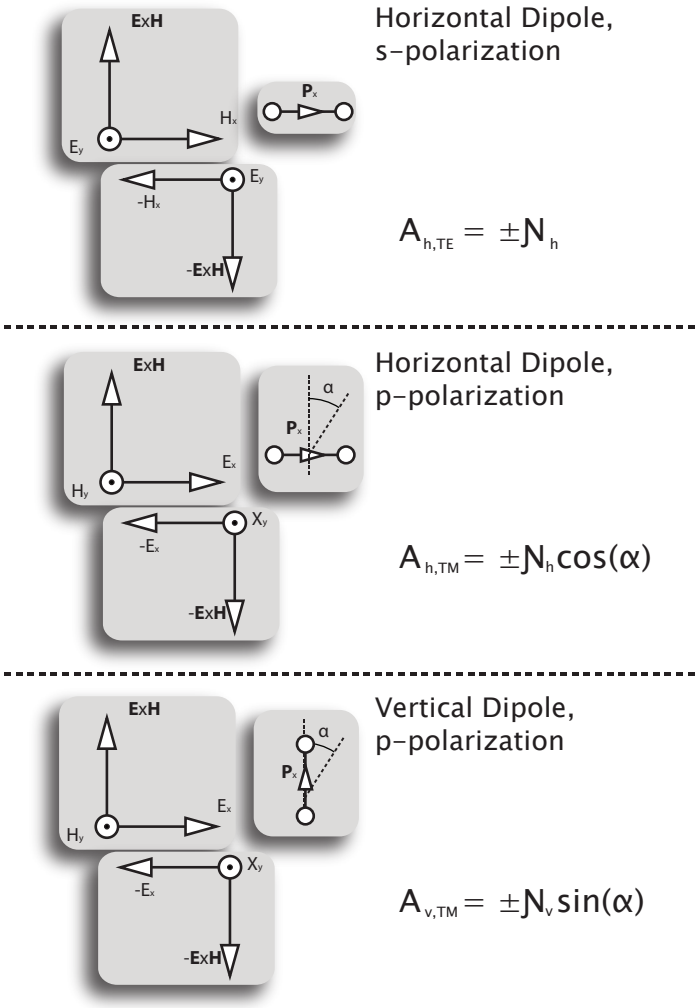

Figure 4.3: Interactions of Dipoles with Fields

The source terms are treated as additive terms to the scalar field representing the electromagnetic waves. As such we find that

$$\begin{pmatrix} A_{\uparrow}\theta_1 \\ A_{\downarrow}\theta_1 \end{pmatrix} = \begin{pmatrix} E^{<}_{1\uparrow}\theta_1 \\ E^{<}_{1\downarrow}\theta_1 \end{pmatrix} - \begin{pmatrix} E^{>}_{1\uparrow}\theta_1 \\ E^{>}_{1\downarrow}\theta_1 \end{pmatrix} \tag{4.24}$$

Where the subscript of the source term indicates the layer number in which the term is present (Fig: 4.1) and the superscripts > and < indicate the field immediately adjacent to the source layer at points higher and lower than the source term layer respectively. The fields outside the device can then be described by constructing the appropriate matrix from the source point to the escape layer using equation 4.16 to give

$$\begin{pmatrix} E^{>}_{1\uparrow} \\ E^{>}_{1\downarrow} \end{pmatrix} = \begin{pmatrix} m^{>}_{11} & m^{>}_{12} \\ m^{>}_{21} & m^{>}_{22} \end{pmatrix} \cdot \begin{pmatrix} 0 \\ E_0\theta_0 \end{pmatrix} \tag{4.25}$$

and

$$\begin{pmatrix} E^{<}_{1\uparrow} \\ E^{<}_{1\downarrow} \end{pmatrix} = \begin{pmatrix} m^{<}_{11} & m^{<}_{12} \\ m^{<}_{21} & m^{<}_{22} \end{pmatrix} \cdot \begin{pmatrix} E_2\theta_2 \\ 0 \end{pmatrix} \tag{4.26}$$

Similar to the field above, the > and < superscripts indicate the matrix elements describing the structure above and below the source layer, respectively.

Since the field in the structure will vanish in the metal case, we are not interested in the E_2 term and determine the overall field by calculating E_0 using

$$E_0 = \frac{m^{<}_{21}A_{\uparrow} - m^{<}_{11}A_{\downarrow}}{m^{>}_{22}m^{<}_{11} - m^{<}_{21}m^{>}_{12}} \tag{4.27}$$

Using the matrix formalism, the electric field can then be found at any point within the structure. Points inside layers are found by splitting the layer into two layers, whose total thickness is the thickness of the original layer, but is otherwise identical. Stepping through the layers in this manner then allows the construction of the field profile of the stack. The metal cathode is split into two sections. One is the infinite half space required for description of the structure, and the second

is a thinner layer, allowing the description of the field within the cathode. This field is a rapidly decaying field, as expected due to the complex component of the refractive index.

This method allows the description of planar arrangements of emitters in a plane parallel to the plane of the OLED. OLEDs are extended sources, since the emitting region covers a finite, non-zero thickness and may have multiple non-adjacent emission layers such as in stacked OLED devices. In both the case of a single and multiple emitting layers, the recombination rate and hence the emission rate itself may be a function of the z position in the device $R(z)$. Hence it is necessary to calculate the emission from a number of small elements of the emitting layer, the relative magnitudes of the emissions from each slice can then be modified by an appropriate weighting function. The emitting layer is split into two or three layers, with an active emitting band for which the emission is calculated and passive regions where the emission is not calculated. This is possible in the matrix method formalism, since the ϵ and μ for the active and passive regions are identical, and so are treated as invisible boundaries.

4.5 Emission from Surface Substrate

The thin film model calculates the emission from the thin film stack, however measurement of bottom emitting OLEDs requires the light to pass through the glass substrate into air. Modeling the substrate using the thin film code is inappropriate, due to the thickness of the glass being much larger than the wavelength of light, and the low spatial and temporal coherence of the OLED. For top emitting OLEDs conversely, the OLED is often encapsulated under a glass layer, with an intermediate air gap that may be of the order of a few micrometers thick. Assuming that the thickness of the air gap is equal over the entire area of the OLED, then this may result in Fabry Perot type optical effects (Section 4.30). Differences in the thickness of the air gap result in interference fringes, such as seen in Newton's rings, and are visible to the naked eye. In this case the air gap can also be included into the optical model and the interference fringes observed. While in principle this effect is easily studied, detailed analysis is more complex, as the precise properties of the air gap are difficult

to measure, since the thickness varies strongly between OLEDs, and often the properties of the air gap are such that the effect is not visible at all.

For bottom emitting OLEDs, since the use of the thin film code to describe the substrate is inappropriate, the emission is calculated only into glass, and then Snell's Law and the Fresnel Equations are applied to calculate the final output.

4.6 Calculation of final OLED emission

The code assumes white light emission, and calculates the optical output regardless of the properties of the actual emitter. OLEDs however have specific spectral properties regarding emission that are independent of the properties of the stack or structure in which they emit, as a result of the various properties of the chemical bonds and binding energies. The azimuthal angle is θ, with 0^o being the normal to the device, and ϕ is the circular angle. These angles apply to both this model and the ray tracing model (Fig: 4.4).

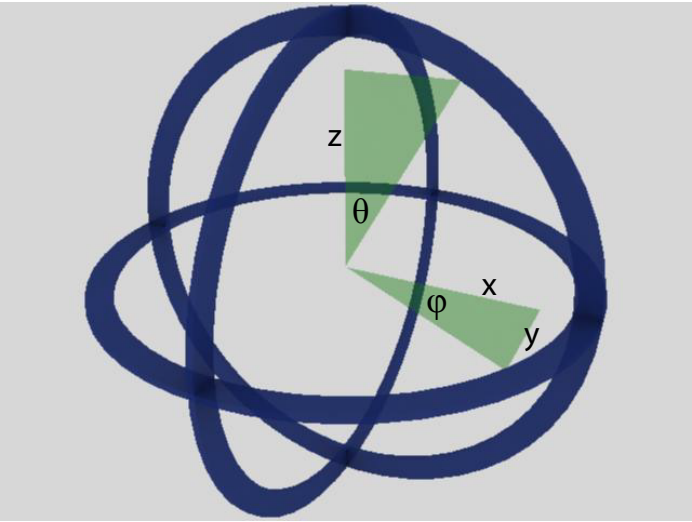

Figure 4.4: Representation of θ, ϕ and the directions for the two optical models

As a result, it is necessary to include the effect of the OLED emitter itself, and this is achieved through a convolution of the emission properties of the device and the photoluminescent emission

spectrum of the OLED (Fig: 4.5). Ideally the photoluminescent spectrum should be taken from a sample of the material with physical properties such that there are little or no interference effects. If the photoluminescence spectrum is taken from a thin film stack for example, the emission will be modified by the peculiar properties of that stack, and will not be a true representation of the spectral range of that emitter.

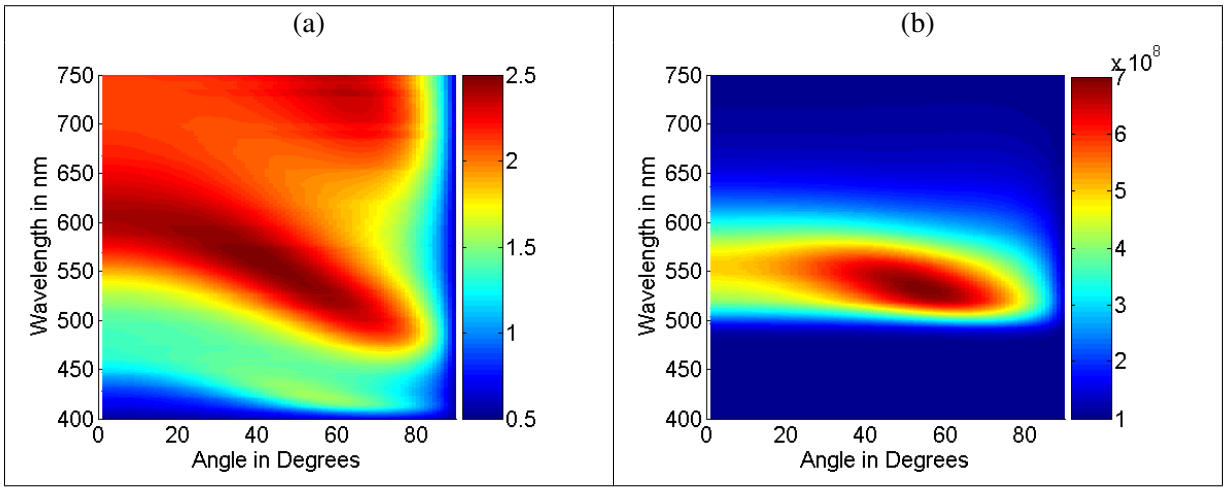

Figure 4.5: Emission from device (a) before and (b) after Convolution of Device Affinity with Photoluminesence Spectrum

4.7 Variation of Layer Properties

Manipulating the thicknesses of individual layers can have a strong effect on the optical and electrical properties of a device. The efficiency of a device K is a function of the electrical efficiency η_e the optical efficiency η_o and the outcoupling efficiency η_c; $K = \eta_e\eta_o\eta_c$. In general, increasing the layer thickness will result in a reduction of the electrical efficiency η_e as a result of increasing the resistance over the area, and thus requiring a higher voltage to generate the same current. Addition of dopants however can mitigate this effect [5] and so with the use of this technique the restrictions on the layer stack are reduced and the layers can be therefore designed to improve optical properties including η_o, with less concern for the counterbalancing loss in electrical performance η_e.

The Layer Structure

The layer structure in the following analyses (Fig: 4.6) will be based on the same structure, except where indicated. The structure consists of a transparent anode (ITO unless otherwise indicated), metal cathode (Ytterbium, unless otherwise indicated), and a series of organic layers. The hole transport and electron transport layers (HTL and ETL respectively) are doped layers. The hole blocking and electron blocking layers (HBL and EBL respectively) are undoped layers, which also provide a buffer layer between the doped transport layers, and the emitting layer in order to minimise diffusion of the dopants into and from the emitting later, and finally the emitting layer itself. The refractive indexes for all material are frequency dependent, and were found through measurement using an ellipsometer.

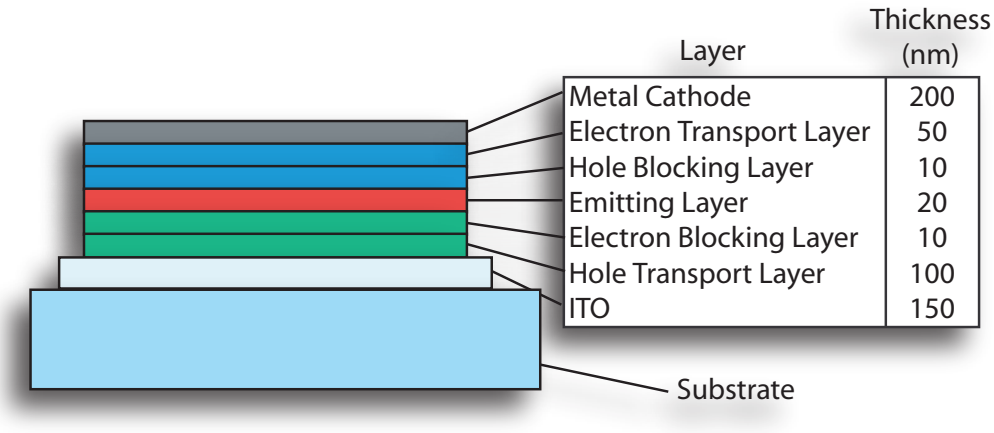

Figure 4.6: Detailed Standard Layer Structure

4.7.1 Different Metal Cathodes

The cathode is typically chosen to be a metal, due to the good electron transport properties and good properties as reflecting surfaces, depending on the metal in question. Where possible, the work function should be low, or close to that of the organic layers, in order to ensure good electron injection, however where this is not possible, as is the case in aluminium, an additional layer such

as lithium fluoride (LiF) of a few nanometres can be added to improve injection. Materials such as magnesium and calcium suffer the problem of oxidization, and unlike aluminium, do not form stable protective oxide layers, thus are prone to burning away and reacting strongly with encroaching water and oxygen. Other metals such as ytterbium may also be used. Other reasons for particular material choices include cost, and physical properties limiting their use as cathodes, for example, aluminium requires high temperatures for deposition, result in substrate heating which may damage the organic layers and the aluminium sources may be very short lived. Ytterbium provides a convenient metal in terms of these physical properties, and can be deposited in the Vertical In-Line Deposition System, within the operational parameters of the machinery. Optically the metals are almost purely reflecting layers: Their complex refractive index leads to very rapid attenuation of the electric field within the metal layer, dropping exponentially toward zero within a few nanometres, however, due to the large refractive index mismatch between the metal and subsequent layers, they make good reflecting surfaces, hence their common use in mirrors. The absorption properties vary with wavelength and material, but for metals such as aluminium and silver, they show a reflection of roughly 80-90% over most of the visible spectrum. Metals such as gold are much better in the red and infra red, however are poor reflectors in the blue. The different metals most commonly used in OLED production are aluminium, magnesium, calcium, silver and more recently ytterbium. Since the thickness of the cathode layer mist be in the order of a hundred or so nm, variation of thickness is largely irrelevant, since most of the transmitted light will have attenuated anyway, and so we will only consider the difference between the different metals as related to the emission of the whole device in the bottom direction. The following analysis considers devices otherwise identical except for the particular metal of the cathode. No additional layers such as LiF have been included. The following analyses the effects of choosing three different metals (magnesium, silver and ytterbium) as the cathode.

Effects of Choosing Magnesium, Silver or Ytterbium as the Cathode Metal

The refractive indices of three common cathode metals are analysed. Two standard stacks are studied, one optimized for red emission and another optimized for blue emission. The refractive indices

for the three metals (Figs: 4.7,4.8 and 4.9) were measured, and used in the simulation. The white light output for the tests was compared directly, in order to analyse the effects of different metal choices on the emission of light. For each wavelength and azimuthal angle, the ratio was found between the emissions of the devices with different metals in order to determine the effectiveness of the metals as cathodes, as a function of their optical properties (Figs: 4.10, 4.11 and 4.12). The overall white light emission was compared (Table: 4.3), and also the total emission (Tables: 4.4, 4.5), for the emission modified to take into account the spectral properties of the emitter.

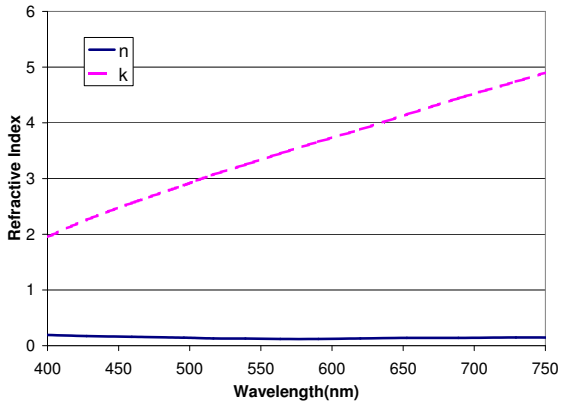

Figure 4.7: Refractive Index of Silver

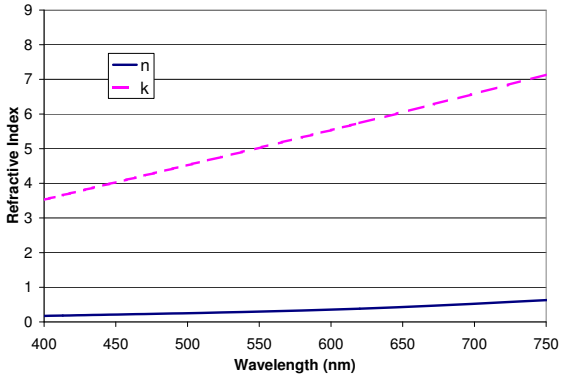

Figure 4.8: Refractive Index of Magnesium

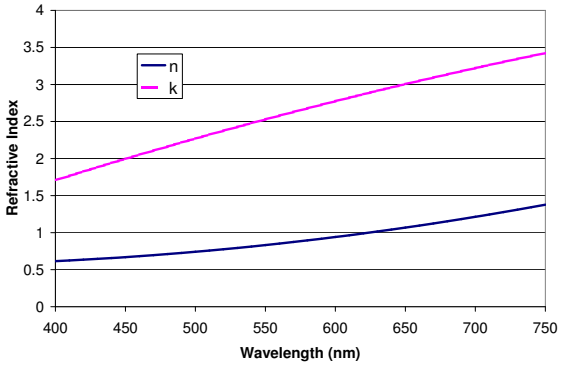

Figure 4.9: Refractive Index of Ytterbium

Results

Ratios of Total White Emission for Different Metals			
	Metal (Denominator)		
metal (numerator)	Mg	Ag	Yb
Mg	1.0	1.0	0.79
Ag	1.0	1.0	0.81
Yb	1,26	1.237	1.0

Table 4.3: Comparison of Total Outputs for White Light Emission

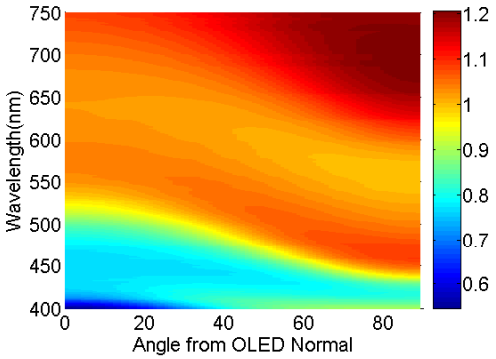

Figure 4.10: Ag:Mg Emission Ratio

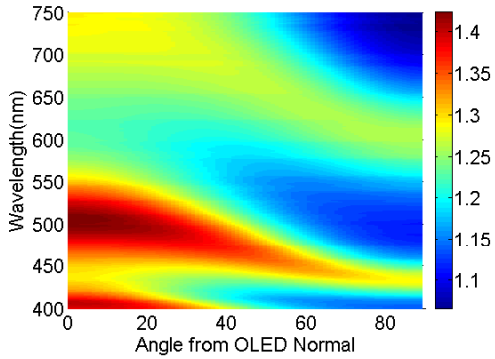

Figure 4.11: Ag:Yb Emission Ratio

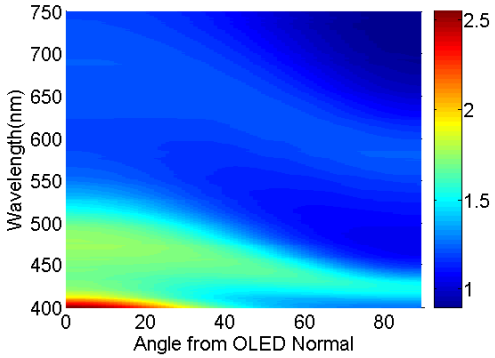

Figure 4.12: Mg:Yb Emission Ratio

Ratios of Total Green Emission for Different Metals			
	Metal (Denominator)		
metal (numerator)	Mg	Ag	Yb
Mg	1.0	1.02	0.83
Ag	0.98	1.0	0.82
Yb	1.2	1.226	1.0

Table 4.4: Comparison of Total Outputs for Emission taking into account the Green Electroluminescent Spectrum

Ratios of Total Blue Emission for Different Metals			
	Metal (Denominator)		
metal (numerator)	Mg	Ag	Yb
Mg	1.0	0.94	0.73
Ag	1.06	1.0	0.79
Yb	1.36	1.27	1.0

Table 4.5: Comparison of Total Outputs for Emission taking into account the Blue Electroluminescent Spectrum

Discussion

As expected, the devices show poorer performance in the blue for those containing ytterbium, due to the refractive index components. This is stronger for the blue device than the green device, since the emission of the blue device is more strongly affected. This is a fundamental property of the ytterbium, and there is no trivial way to counteract this. Silver and magnesium perform in a quite similar fashion, with Mg the better reflector in the green, and Ag the better reflector in the blue. While the overall performance does vary between metals, it is clear that the peak wavelengths for emission from the devices are not significantly altered, and so devices optimized for particular colours with one metal will also be optimized for other metals.

4.7.2 Different Anode Materials

Since the earliest multi-layered OLEDs [6], indium tin oxide (ITO) has been the anode of choice as a result of its useful properties; A high transparency in the visible range combined with high conductivity and high work function, making it a suitable hole injector. Disadvantages however include high cost, as a result of the rarity of indium, and diffusion of indium into the organic layers, resulting in degraded device performance [7]. Alternative materials such as aluminium doped zinc oxide (ZAO) have been studied [8, 9, 10] [1] and show promise for replacing ITO as the anode of choice in bottom emitting OLEDs, due to their lower costs and useful electrical and optical properties. Differences remain however and it is important to ensure that these do not significantly reduce the effectiveness of the device. For a thickness of 200nm ZAO deposited in the Vertical In-Line System at the Fraunhofer IPMS has n and k values as shown in figure 4.13, and also a low sheet resistance, making it a suitable material for use as an OLED anode. These values however do vary with the thickness of the layer, and other deposition conditions such as the temperature of the source and substrate, speed of oscillation, etc. and so to perform these calculations on different thicknesses of ZAO requires measurement of those particular layer properties.

A typical ITO thickness for OLED devices is 150nm, and the particular properties depend

[1] [8] refers to ZAO as AZO

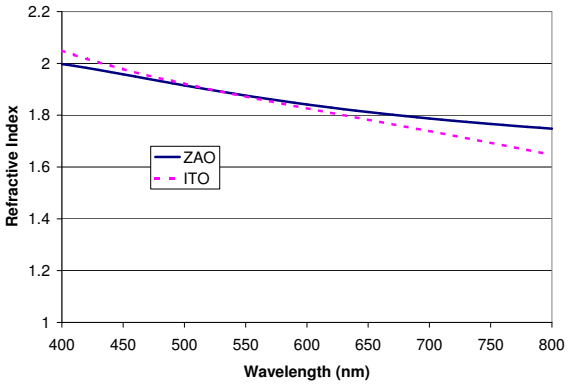

Figure 4.13: measured n and k values for ITO and ZAO deposited at the IPMS

strongly on the deposition as well as annealing and other post-deposition processes [11, 12]. For the Vertical In-Line System ZAO may be deposited directly, though there are no opportunities for annealing processes. For typical deposition conditions, each pass of the substrate under the ZAO source results in a layer of ZAO some 90nm thick. Two passes are carried out, resulting in a layer thickness between 180 and 200nm. The refractive index of the layers is measured, and the same device deposited on the substrate.

As can be seen, this results in the peak wavelength shifting to lower longer wavelengths. The principal reason behind this is the difference in the layer thickness, and closer analysis shows that for a given thickness the change in the output of the device when changing between ITO and ZAO is negligible, making ZAO a suitable replacement in terms of optical properties.

4.7.3 Hole Transport Layer (HTL) thickness Variation

Adjusting the dopant concentration can improve the current transport properties of the OLED, such that the same distribution of excitons in the emitting layer can be maintained. As a result this allows for an extra degree of freedom in adjusting the layer properties, since the current and voltage properties can be maintained for a variety of transport layer thicknesses. The following analysis

details the effects of changing the thickness of the Hole Transport Layer, while maintaining all the same parameters for other layers. The particular stack chosen (Fig: 4.6) will be used again in adjustment of electron transport layer (ETL) thickness (4.7.4).

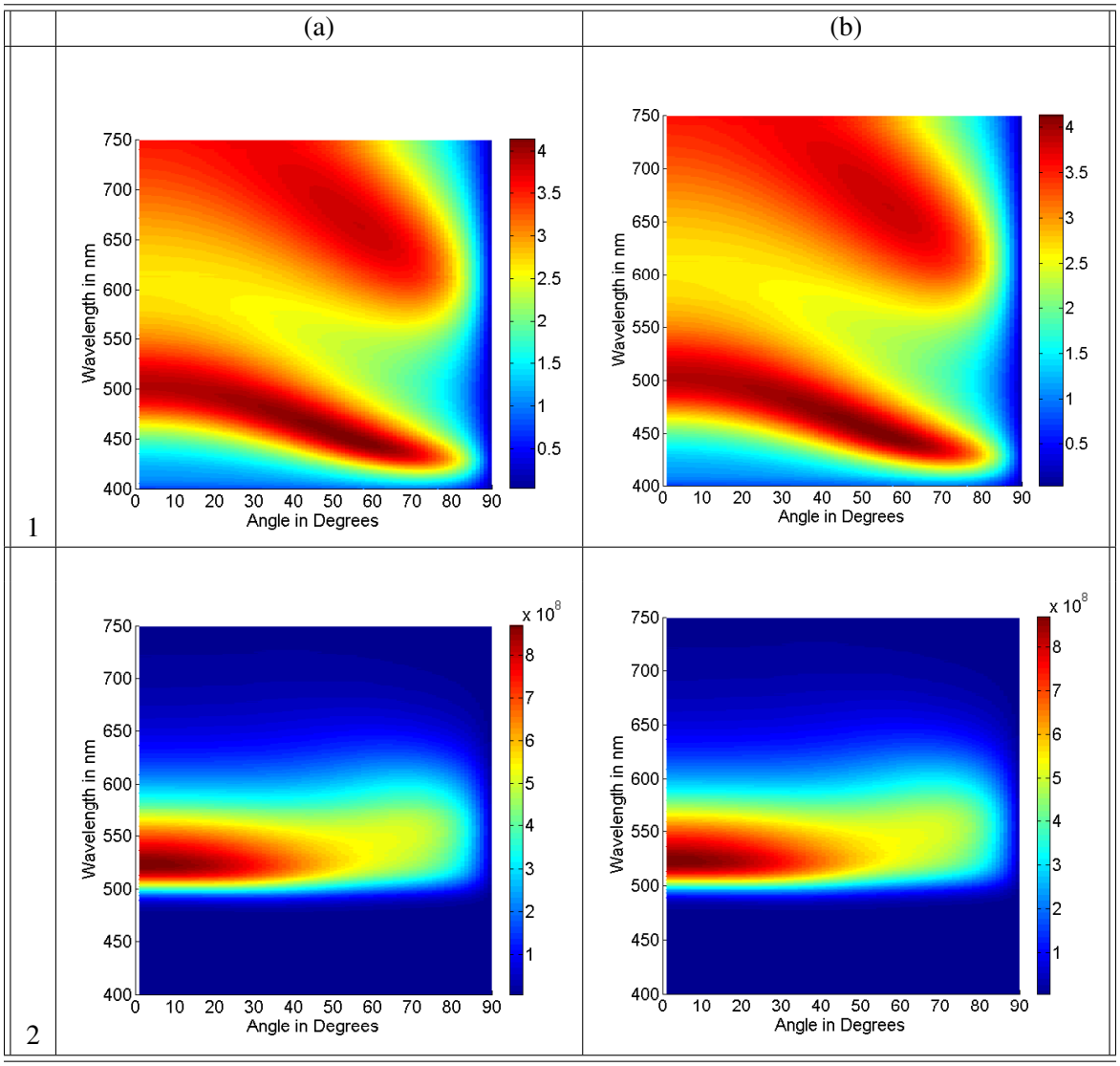

Figure 4.14: Theoretical (1) affinity and (2) emission from standard device with green emitter, replacing (a) 150nm ITO with (b) 200nm of ZAO

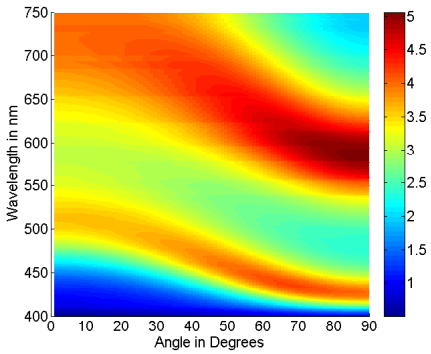

Figure 4.15: 80nm HTL, Affinity

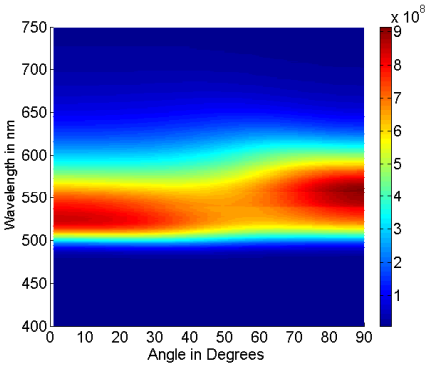

Figure 4.16: 80nm HTL, Emission

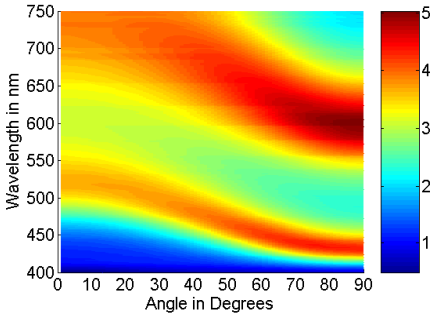

Figure 4.17: 90nm HTL, Affinity

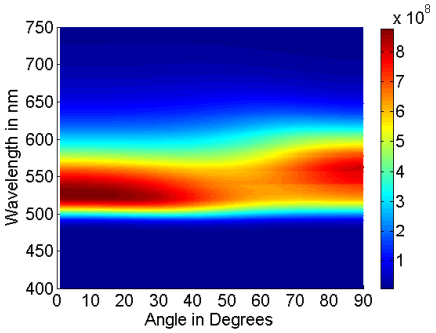

Figure 4.18: 90nm HTL, Emission

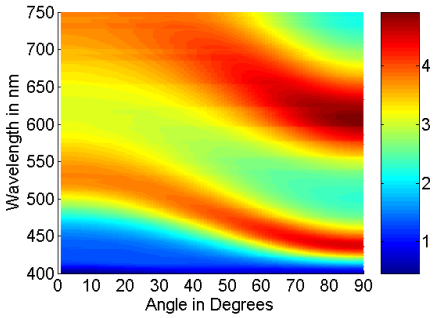

Figure 4.19: 100nm HTL, Affinity

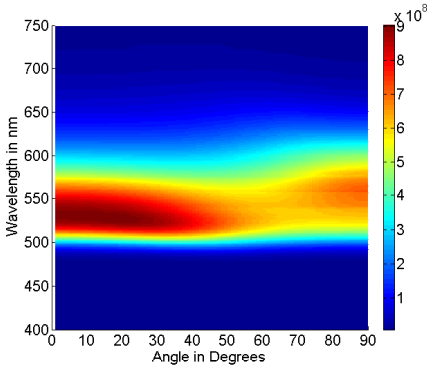

Figure 4.20: 100nm HTL, Emission

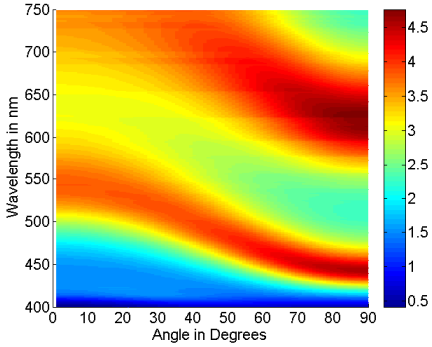

Figure 4.21: 110nm HTL, Affinity

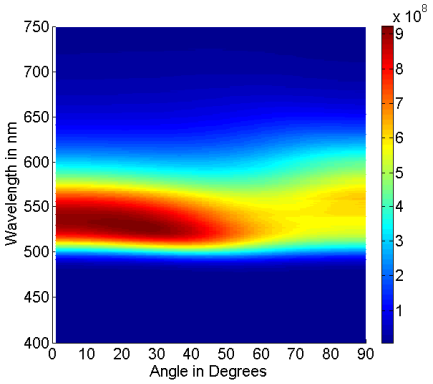

Figure 4.22: 110nm HTL, Emission

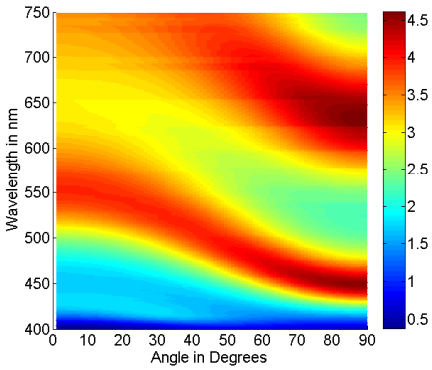

Figure 4.23: 120nm HTL, Affinity

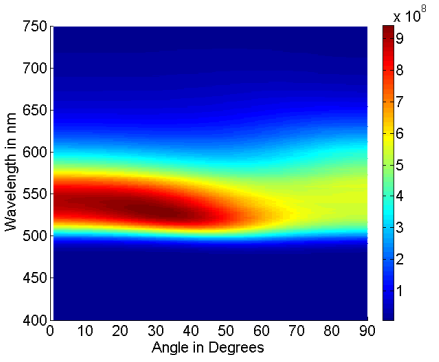

Figure 4.24: 120nm HTL, Emission

Figures 4.15, 4.17, 4.19, 4.21 and 4.23 show the affinities for a variety of devices, and Figures 4.16, 4.18, 4.20, 4.22 and 4.24 show the affinities convolved with the photoluminescent spectrum, to show the output of a device. These show that as the hole transport layer gets thicker, the peak wavelength of the emission drifts to longer wavelengths. It can be seen in Fig: 4.23, that as the layer gets thicker, new peaks begin to emerge; between 400 and 450nm, a new peak is starting to form.

For a discussion of experimental results, see section 4.9.

4.7.4 ETL thickness variation

The distance between the cathode and the emitter is a much more critical distance than between the anode and emitter. The cathode provides a highly reflective surface, resulting in strong interference properties, and also the presence of free electrons allows the formation of mirror dipoles, which again may cause interference effects. Other effects not covered here, such as the formation of surface plasmons also result in the reduction of the efficiency of the device.

As the thickness of the layer increases, we see a rise in the emission up to the optimal value, when the distance of the emitting layer from the cathode for a given wavelength is $^{\lambda}/_{4}$ This is the ideal distance from the emitter, as the π phase shift on the metal-glass interface results in constructive interference. Thicker layers see a dip in the emission as we approach regions of destructive interference, then continue to rise and fall. The thicker the device gets, the more of these peaks there are, as increasingly large numbers of wavelengths can fit in the region. Thicker devices present a problem to optimization of OLED devices, as larger numbers of peaks are more sensitive to variations in layer thicknesses. The ideal thickness of a device is to have the peak of emission of the particular OLED emitter at the peak of affinity for that particular device, taking into account also, the drop off in emission efficiency either side of the peak. For different angles, the affinity of the device changes, with the peak wavelengths forming a band, with lower wavelengths seeing higher emission, for higher angles. This results in variation of the colour coordinates with angle, even for a device otherwise optimized for emission in the forward direction. Considering a particular angle, as the thickness of the ETL is increased, the peak is seen to move in the direction of higher

wavelength. This is expected, since as the thickness increases the wavelength for which the optimal emission point is $^{\lambda}/_{4}$ also increases (Figs: 4.25 to 4.30).

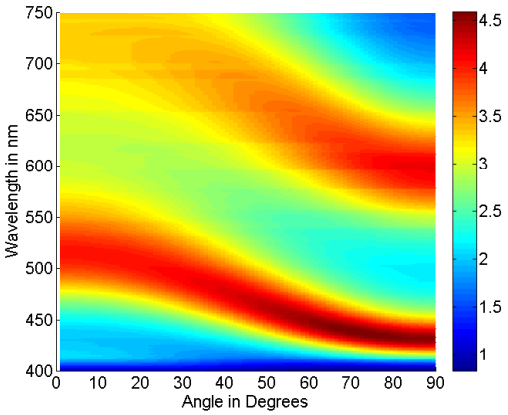

Figure 4.25: 30nm ETL, Affinity

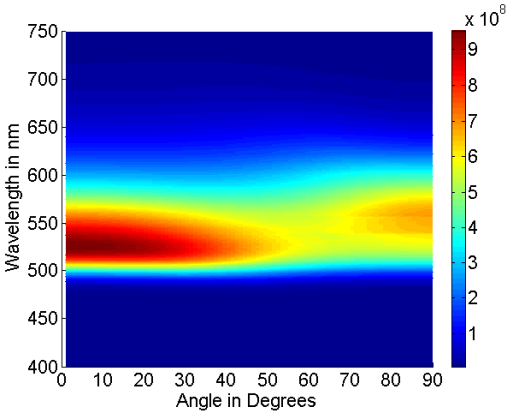

Figure 4.26: 30nm ETL, Emission

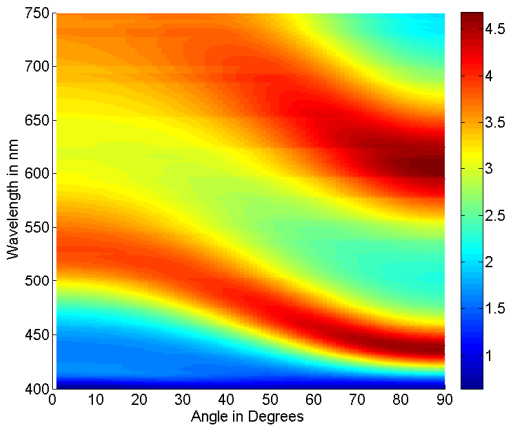

Figure 4.27: 40nm ETL, Affinity

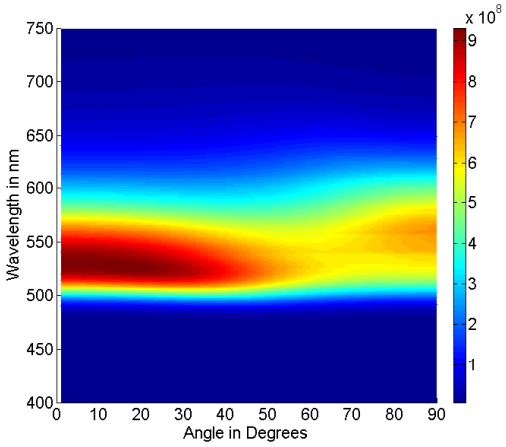

Figure 4.28: 40nm ETL, Emission

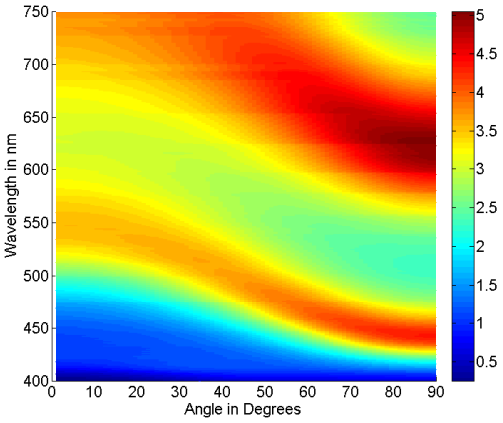

Figure 4.29: 50nm ETL, Affinity

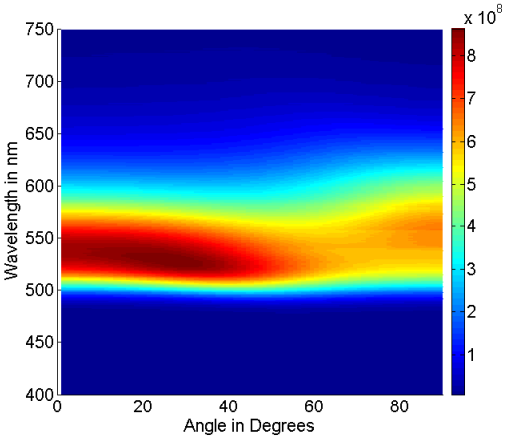

Figure 4.30: 50nm ETL, Emission

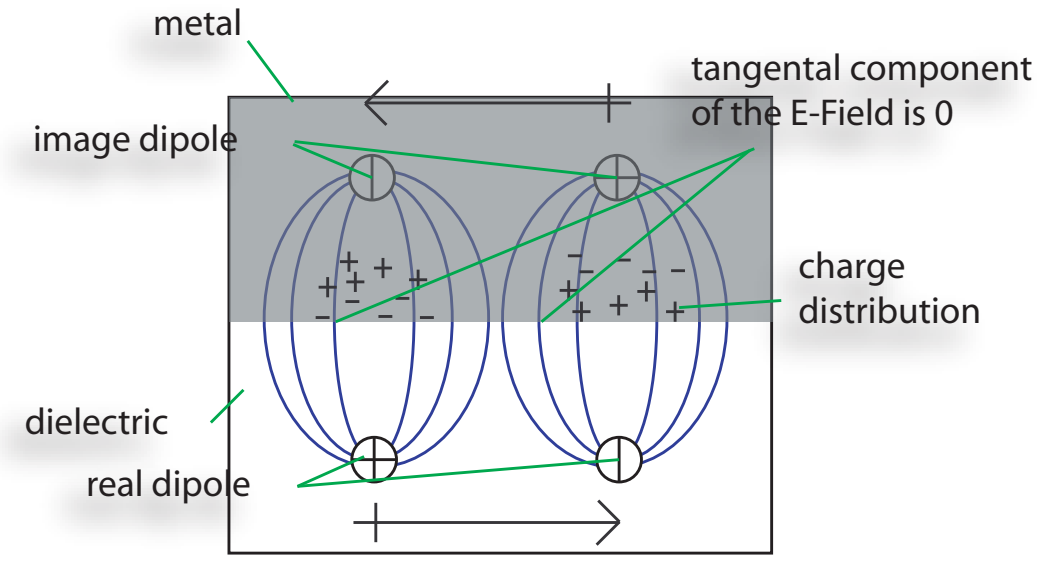

Figure 4.31: The location of the Image Dipole

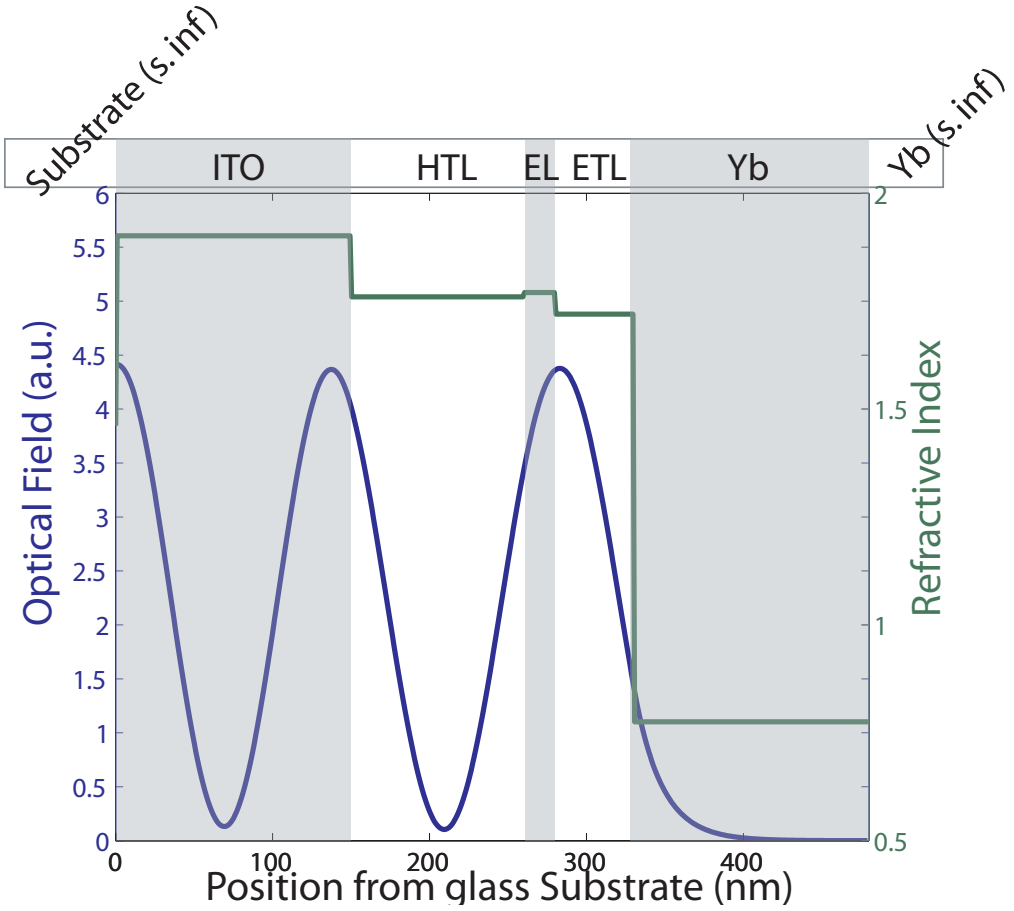

Figure 4.32: The Field Structure of the OLED device within the layer stack ("s. inf" layers are optically thick)

Explanation for effects of Layer Thickness Alteration

Physically, the changes seen in altering the thickness of the ETL are the result of the effect of the induced dipole in the metal layer (Fig: 4.31). For a charge close to the metal boundary, we must consider the boundary conditions by application of the appropriate Maxwell Equations (Equations 4.1, 4.3 and 4.4). The induced dipole lies within the metal layer at a distance d from the boundary, where d is also the optical distance from the emitter to the boundary. For large distances, the effect of the image dipole diminishes, and normal interference effects dominate. The location of the emitting layer is of critical importance when the distances are within this range, ideally the emitting layer for the peak emission wavelength, should be at a physical distance of $d_p = \frac{\lambda}{4n(\lambda)}$ for a single layer between the emitter and metal. More complex structures with multiple refractive indices must take the varying layer properties into account, such that for k layers, the physical thicknesses of the layers d_j must be related to the quarter wavelength by

$$\sum_{j=1}^{j=k} d_j n_j(\lambda) = \frac{\lambda}{4} \tag{4.28}$$

The induced dipole oscillates with a phase shift of π when compared to the emitting dipole. For peak emission at a given wavelength of light the optimal distance is $\lambda/4$, putting the image a distance of $\lambda/2$ away from the emitter. This results in the emitted photon constructively interfering with the effect of the image dipole, allowing for a local maximum emission. When the peak of the field is in the same location as the emitting layer (Fig: 4.32), this allows for maximal emission from the layer for that particular wavelength. Since the strength of the electric field due to the dipole drops off as

$$E(\mathbf{r}) = \frac{1}{4\pi\epsilon_0 r^3}\left(3\left(p \cdot \hat{r}\right)\hat{r} - p\right) \tag{4.29}$$

where

E is the electric field.

$\hat{r}$ is the unit vector parallel to r.

r is the vector from the position of the dipole to the point at which the field is being measured.

r is the distance from the dipole to the field.

p is the vector dipole moment.

ϵ_0 is the permittivity of free space.

This differs from the HTL case, in which the effect on the emission is principally the result of interference due to the reflection from the OLED-glass boundary. The latter effect is much weaker than the effect due to the ETL thickness change, especially where the ETL thickness puts the emission layer close to the metal layer.

For a discussion of experimental results, see Section 4.9.

4.8 Analysis of Air Gap Thickness and Spatial Coherence of OLEDs

In a top emitting OLED, it was noticed that there were a number of interference fringes which decayed with angle[13] (Fig: 4.33). It was thought that this was caused by the air gap between the OLED and the cover glass (Section 4.5) and slight variations in the thickness of the gap over the area of the OLED. The fringes were also visible by eye when illuminated with a fluorescent lamp (Fig: 4.34). It was decided to study this effect in more detail to determine possible ramifications of this interference.

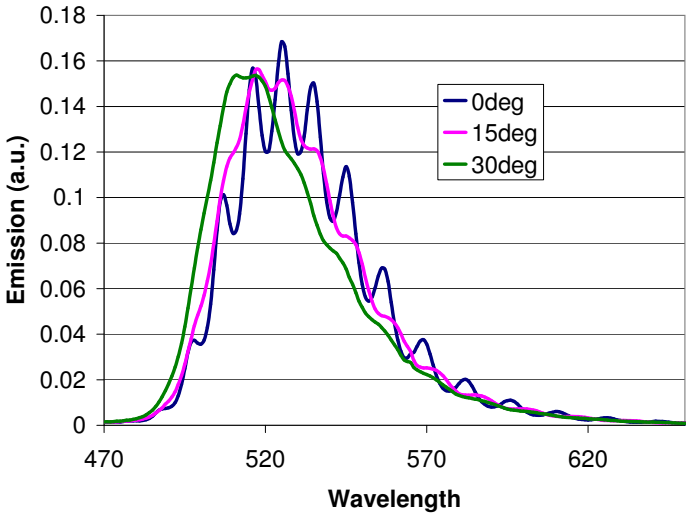

Figure 4.33: Interference fringes with angle and wavelength

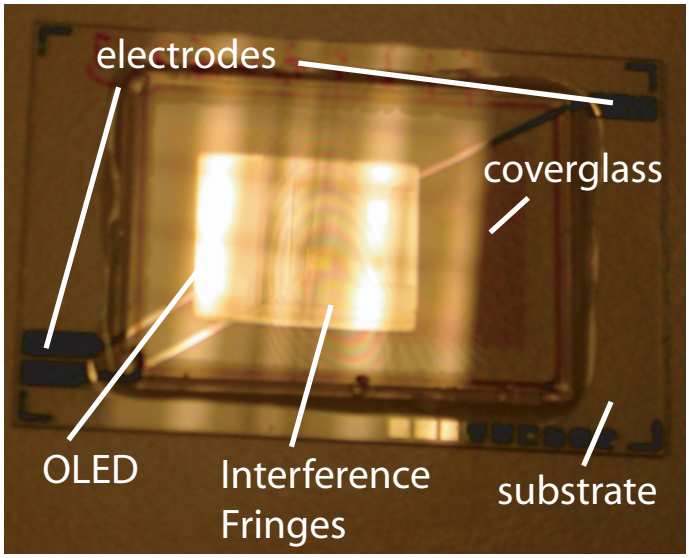

Figure 4.34: Observed fringes for an OLED illuminated by a Fluorescent Lamp

The devices investigated were green emitting OLEDs vacuum-deposited onto a silver coated glass substrate. The organic layer sequence begins with a 45nm thick N',N'-tetrakis(4-methoxyphenyl)-benzidine (MeO-TPD) layer doped with 4 mo% of 2,3,5,6-tetrafluoro-7,7,8,8,-tetracyanoquinodimethane, followed by a 15nm thick 2,2',7,7'-tetrakis-(N,N-diphenylamino)-9,9'- spirobifluorene (Spiro-TAD) electron blocking layer, an emitting layer consisting of 5nm of tris(2-phenylpyridine) iridium ($IR(ppy)_3$) doped 4,4',4''-tris(Ncarbazolyl)-triphenylamine (TCATA), and similarly doped 2,2',2'' -(1,3,5-benzenetriyl) tris[1-phenyl-1Hbenzimidazole] (TBPI) of thickness 10nm, both with a doping concentration of 8 wt%. Finally a 10 nm 4,7-diphenyl-1,10-phenanthroline (BPhen) hole blocking layer, followed by a 25nm thick co-evaporated layer of BPhen and cesium (Cs) and a 15nm thick silver layer are deposited.

Analysis of the OLED before covering did not show this interference pattern, and the pattern only appeared in approximately 10% of produced devices and so was most likely the result of the peculiar properties of the individual covers and the thickness of the glue adhering the cover glass to

the substrate resulting in adequate reflection properties to allow the fringes to form. While it is not possible to determine the exact properties of the air gap, it is known from the design of the cover glass, that the gap thickness is in the order of $15\mu m$. By measuring the distance between adjacent peaks, it is possible to determine the air gap thickness, since the peaks correspond to points where positive interference occurs, we know that the number of whole waves fitting in the air gap for two adjacent peaks must differ by $^1/_2$ since the advancement of one half wavelength (an increase in the phase thickness of π will result in a total path length increase of one full wavelength between the initial emission, and reflection from the emitting surface). Hence, if we have an air gap thickness t, then $t = n\lambda_2 = \left(n + \frac{1}{2}\right)\lambda_1$ where n is some unknown number of waves, and λ_1 and λ_2 are the wavelengths at which two adjacent peaks occur and $\lambda_1 < \lambda_2$. Solving for t leads to

$$t = \frac{\lambda_1^2}{2 \times (\lambda_2 - \lambda_1)} \tag{4.30}$$

For the device analyzed, it was found that the thickness of the air gap was in the order of $14\mu m \pm 5\%$, which agrees with expectations. An alternate approach is though determining the Full Width at Half Maximum (FWHM) of one of the peaks and from this calculating the finesse of the etalon, and then calculating the thickness of the etalon. Using

$$\delta\lambda = \frac{\lambda_0^2}{2nl\cos(\theta)} \tag{4.31}$$

where $\delta\lambda$ is the FWHM, λ_0 is the central wavelength, n is the refractive index of the etalon, l is the thickness of the etalon and θ is the angle from the normal. This can be simply rearranged to find l given that we know the other parameters. The difficulty however can be in determining the width of the FWHM, since the fringes are convolved with the emission spectra, and so are themselves distorted. The best position to determine the fringe widths is in the regions where the rate of change of emission with wavelength is flat. In the case of the device measured in Figure 4.38. $\delta\lambda = 10 \pm 0.5$, $\lambda_0 = 525 \pm 1$, $n = 1$ and $\theta = 0$. Solving for l, gave a value of $13,800\mu m \pm 5\%$. The error in the final result is due principally to the error in finding the FWHM. By repeating this

for multiple independent measurements over the device, the error can be further reduced. The same calculations were performed on a number of Top Emitting OLEDs produced in the same run, and each gave similar results to within a couple of micrometers. The range of values is due to the slight difference in devices.

Analysis of figure 4.35 gives a standard deviation σ of 8.4^o, so at a deviation of 3σ, or at an angle of 25.2^o 99.7% of effects due to interference will have occurred and the strength of interference will be nominally zero. Considering the distance that the light will have traveled along the device at various angles, should show the spatial coherence of the OLED device as a function of the angle. At 25^o, there is effectively no spatial coherence, and this corresponds, given the thickness of the air gap to a distance of $14\mu m$. The presence of the normal distribution suggests that the decay in the interference effects is due to the spatial coherence of the OLED(Fig: 4.36).

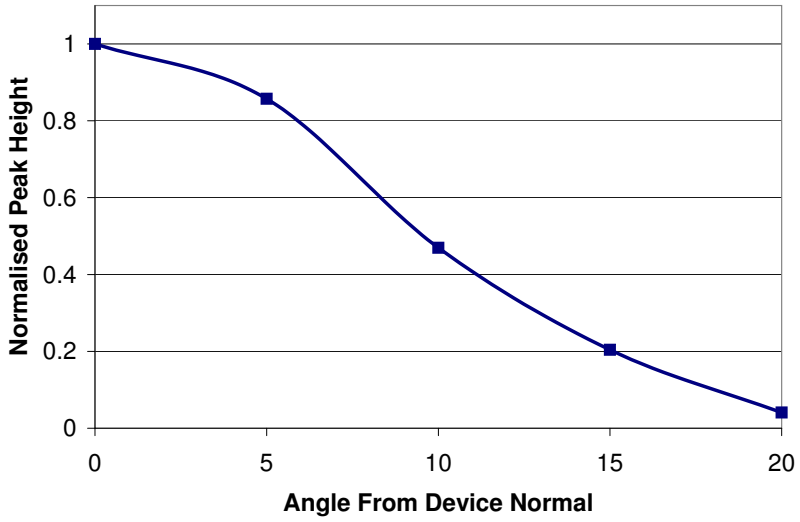

Figure 4.35: Decay of peak heights, normalized to height of forward peak

Each reflection point (numbered) is also an emission point. As the distance between reflection points increases with angle, the coherence between the reflections and emission from that point also decreases, destroying the fringes. Effects on the color coordinates of the device were insignificant and effects on the normally nominally Lambertian emission of the devices were also weak (Fig 4.37), and it was not possible to determine effects on efficiency.

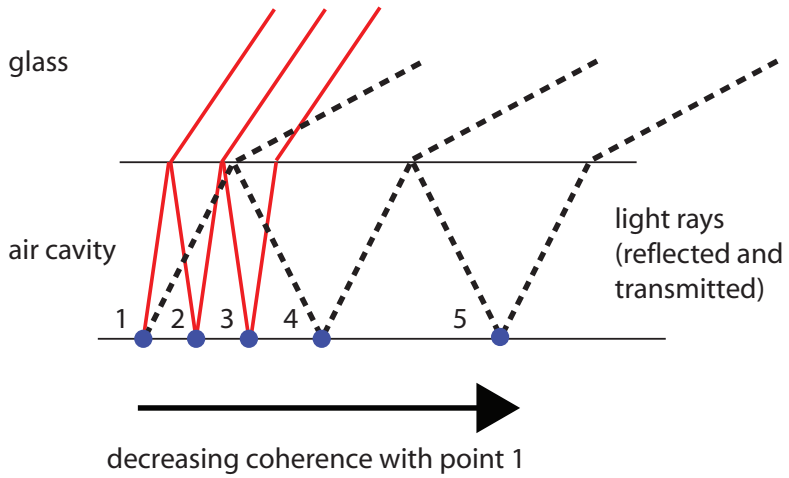

Figure 4.36: Reflections in device and effect on coherence

The justification for the decay of the interference effect with angle is not immediately clear, however it is likely that it is due to perturbations in the thickness of the air gap, and also the spatial coherence of the OLED. Using this method could in principle allow much better characterization of the spatial and temporal coherence of the OLED materials and displays, and give a better indication of the range of structures which the OLEDs can function within acceptable parameters. The comparison between the modelled results (Fig: 4.38a) and the experimental results (Fig: 4.38b) shows a good agreement in the forward direction in terms of the number of peaks, although the peaks are slightly sharper in the modelled results. For the higher angles, 15^o and 30^o again the agreement is good in terms of the basic form and shift of the emission spectra, although the washing out of the peaks becomes far more prominent in the experimental results.

4.9 Experimental determination of layer thickness using Optical Parameters

One of the characteristic features of the affinity spectrum of the OLED display, is the number and position of potential emission peaks. As seen in 4.7.3 and 4.7.4 as the optical thickness of the layers between the cathode and emitting layer are increased, the peaks are seen to move in the direction of

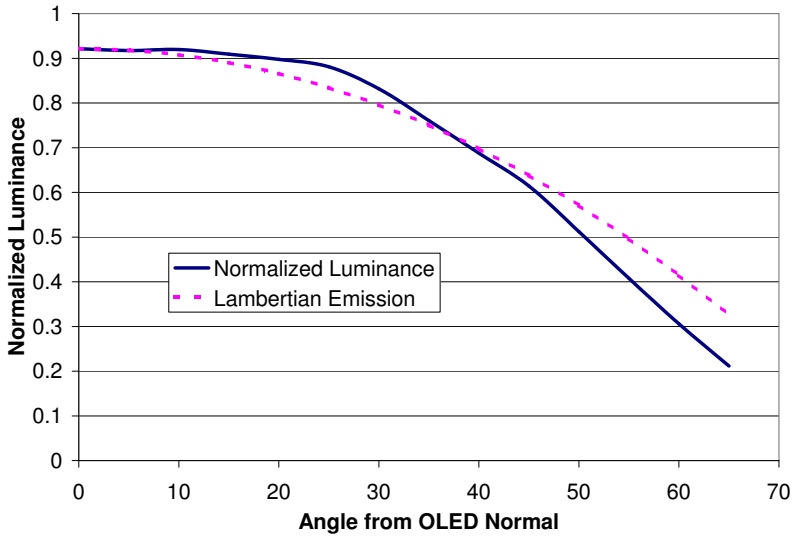

Figure 4.37: Comparison of Luminance with Lambertian Emission

higher wavelengths, and as the optical thickness between the anode and emitting layer are increased, the peaks are seen to move toward higher wavelengths. Since the position of the peak is also a function of the angle, with higher angles having the peaks in the lower wavelengths also, then analysis of the peak position can be a good indicator as to the thickness of certain layers. In the most extreme cases, the photoluminescent emission peak of the OLED can occur in an emission trough for the particular layer structure. This results in very low light output, however, the phenomenon of peak shifting becomes much stronger, as the emission for the whole device is split into two peaks, the relative heights of which are strongly dependent on the thickness of the various layers. This phenomenon can be observed both theoretically and experimentally (Figures:4.39 and 4.40 respectively). In order to test this, a range of OLED devices were prepared, varying the thicknesses of a single layer to demonstrate a good range of peak shifting. The peaks of emission of each of the devices was found, and then plotted. The devices were also modelled, and the positions of the peaks according to the simulation were then plotted alongside the experimental data.

In order to compare the thicknesses of the layers to the theoretical results more precisely, the ratios between the different peak heights was measured at three angles, a ratio between the peak emission at 0^o and 35^o, and a ratio between the emissions at 35^o and 60^o. These were plotted for

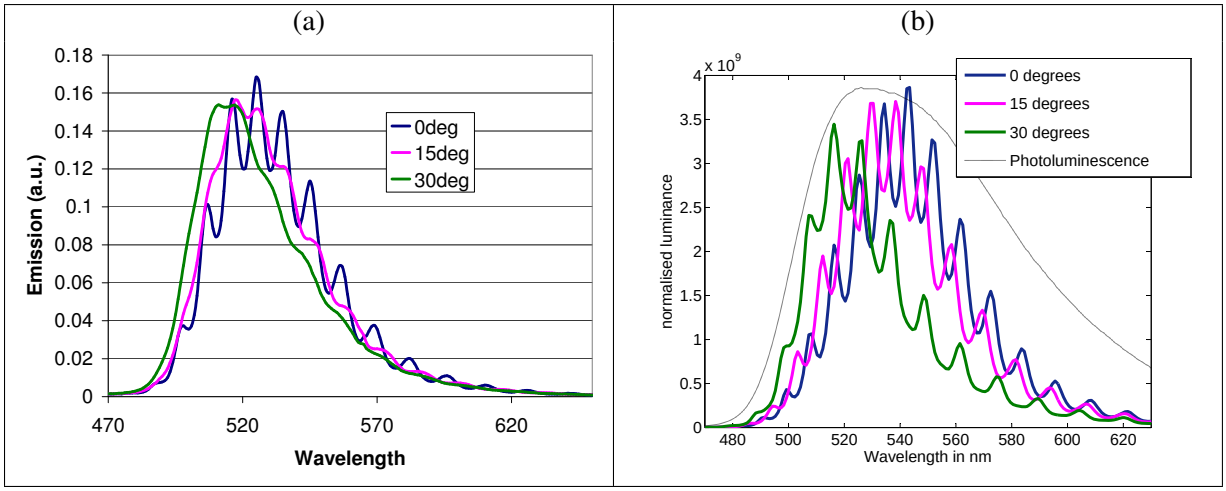

Figure 4.38: (a) Modeled and (b) Experimental results for a Top Emitting OLED with air gap

a number of different ETL thicknesses, and then the experimental results plotted alongside (Fig: 4.43). The red points indicate an ETL thickness of around 121 nm, compared with the experimental expectation of 120nm

The accuracy for the thickness of the layers as deposited was in the order of 5%, and so the devices showed overall good matching with the theoretical predictions, for a range of angles. The model was also compared to other similar stacks with more optimal ETL thicknesses (Figs: 4.41 and 4.41) and good agreement was still seen, indicating the accuracy of the model.

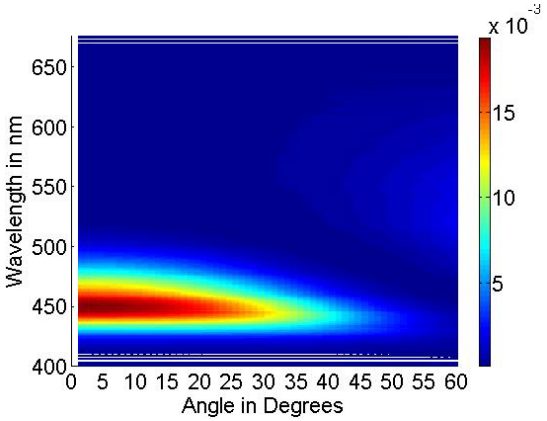

Figure 4.39: Theoretical Peak splitting of device

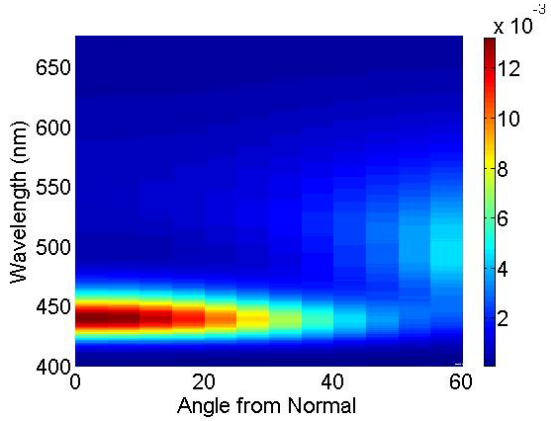

Figure 4.40: Experimental Peak splitting of device

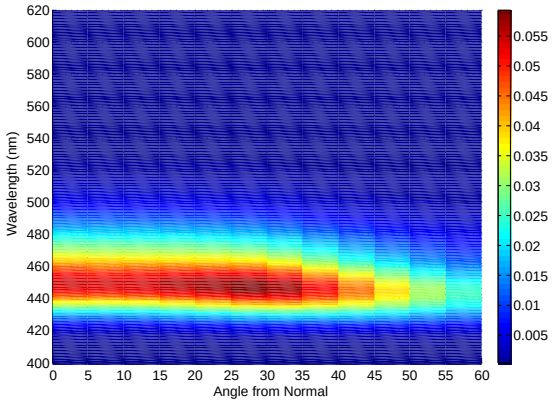

Figure 4.41: Emission from device with 150nm ETL

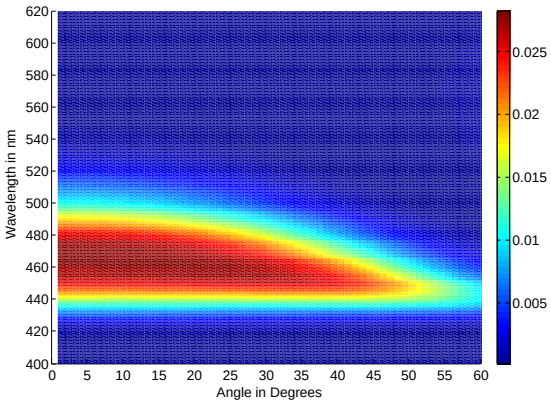

Figure 4.42: Modeled 150nm ETL device

Bibliography

[1] J.C. Maxwell. *A Treatise on Electricity and Magnetism*. Oxford, 1873.

[2] M. Born and E. Wolf. *Principles of Optics (7th (Expanded) Ed.)*. Cambridge University Press, 1999.

[3] P. Yeh. *Optical Waves in Layered Media*. New York: Wiley, 1988.

[4] R.R. Chance, A. Prock, and R. Silbey. Molecular fluorescence and energy transfer near interfaces. *Adv. Chem. Phys.*, 37:1, 1978.

[5] J. Blochwitz, M. Pfeiffer, T. Fritz, and K. Leo. Low voltage organic light emitting diodes featuring doped phthalocyanine as hole transport material. *Appl. Phys. Lett.*, 73:729, 1998.

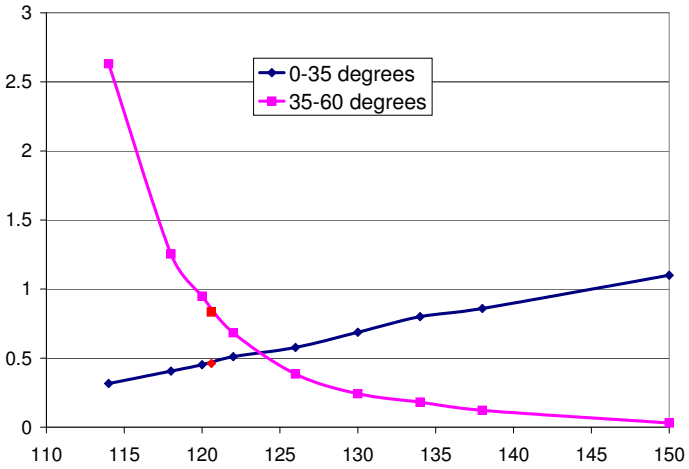

Figure 4.43: Theoretical Ratios (line) compared to Experimental Ratios (red points)

[6] C.W. Tang and S. Van Slyke. Organic electroluminescent diodes. *Appl. Phys. Lett.*, 51:913, 1987.

[7] A.R. Schlatmann, D. Wilms Floet, A. Hilberer, F. Garten, P.J.M. Smulders, T.M. Klapwijk, and G. Hadziioannou. Indium contamination from the indium-tin-oxide electrode in polymer light-emitting diodes. *Appl. Phys. Lett.*, 69:1764, 1996.

[8] J. Zhao, S. Xie, S. Han, Z. Yang, L. Ye, and T. Yang. Organic light-emitting diodes with AZO films as electrodes. *Synth. Met.*, 114:251, 2000.

[9] D. Xu, Z. Deng, Y. Xu, J. Xiao, X. Liang, Z. Pei, and C. Sun. An anode with aluminium doped on zinc oxide thin films for organic light emitting devices. *Phys. Lett. A.*, 346:148, 2005.

[10] X. Jiang, F.L. Wong, M.K. Fung, and S.T. Lee. Aluminium-doped zinc oxide films as transparent conductive electrode for organic light-emitting devices. *Appl. Phys. Lett.*, 83:1875, 2003.

[11] Wen-Fa Wu and Bi-Shiou Chiou. Properties of radio-frequency magnetron sputtered ITO films without in-situ substrate heating and post-deposition annealing. *Thin Solid Films*, 247:201, 1994.

[12] M.G. Mason, L. S. Hung, C. W. Tang, S.T. Lee, K.W. Wong, and M. Wang. Characterization of treated indiumtinoxide surfaces used in electroluminescent devices. *J. Appl. Phys.*, 86:1688, 1999.

[13] D. Hill, K. Leo, G. He, and Q. Huang. Analysis of spatial coherence of organic light-emitting devices through investigation of interference effects observed in top-emitting devices. *Appl. Phys. Lett.*, 90:Online, 2007.

Chapter 5

Ray Tracing Model

5.1 Theory

5.1.1 Basic Model Overview

The model is a ray tracing simulation of structured substrates, which have been proposed as a method of improving the outcoupling of light [1, 2, 3]. The light output is generated from either experimental measurements or theoretical modelling, and the spectral and angular properties of the emitter are inserted into a storage object. The device is described as a grid of points, each containing the layer thicknesses and optical properties of the layers at that grid location, and the position of the interfaces are described by triangular facets with the heights at the points indicated on the grid (Fig: 5.1). The rays are traced from a point on the surface to the interaction triangle where the reflected and transmitted components are calculated, and then themselves either traced to the next possible interaction location or, in the case of edge emission, dumped. Inclusion of polarization effects has been found to be of negligible effect, and so here will be ignored [4]. Many currently studied models are based on the principle of perfectly reflecting edges. This allows for the modelling of large devices with limited structural data, however these are limited in that they cannot model surface spreading of light from complex structures. The final light output is stored in a number of possible ways, either as total light output from each location on the grid, to the integrated angular output

over the whole device. The location of the emitted ray is determined through Monte-Carlo methods. The structure is built either from a mathematical description, or by intentionally determining the thickness of each layer at each point. This method of description has some limitations however, principally that it cannot describe devices with vertical edges, or devices where the layer thickness is zero over extended areas.

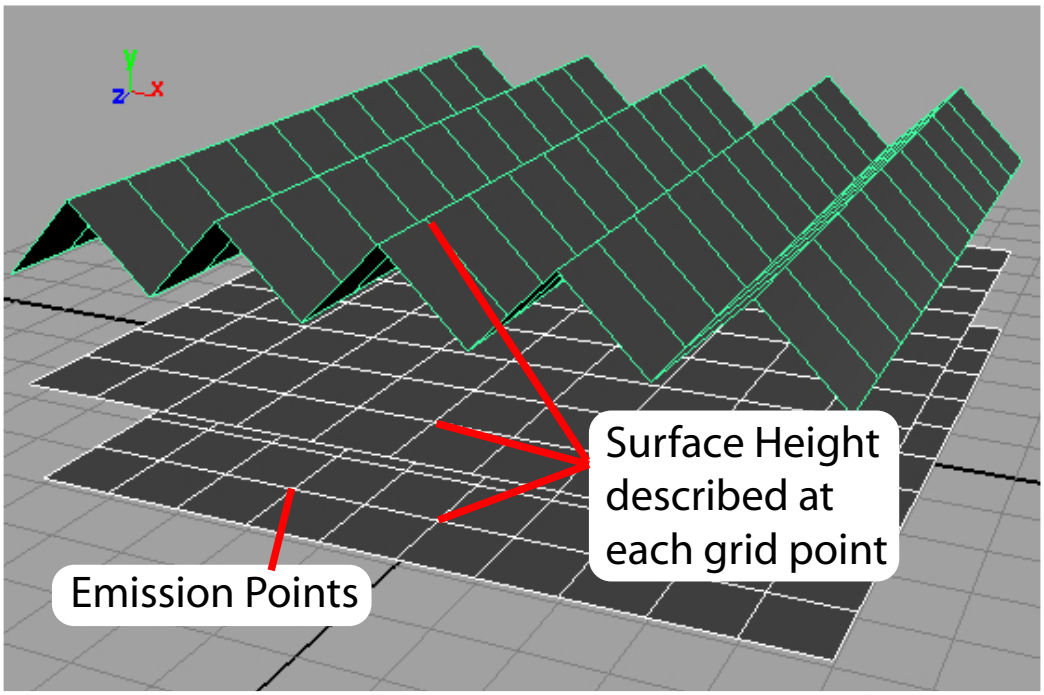

Figure 5.1: Diagram of Grid Describing Substrate Layers

Where light is incident on the area between grid points, the interaction is calculated by breaking the surface between the four grid points into two triangles, and determining the interaction through trigonometric means. The particular arrangement of triangles is important since it affects the shapes formed, particularly where the structure sizes are described in numbers of grid points on the order of 1. For example, if we consider 9 points, with the outer 8 points in the same flat plane, and the central point raised, then for two different ways of splitting the triangles, two quite different surface shapes are realized (Fig: 5.2).

Fig: 5.2a shows the arrangement in which all squares are cut in the same direction, in this case

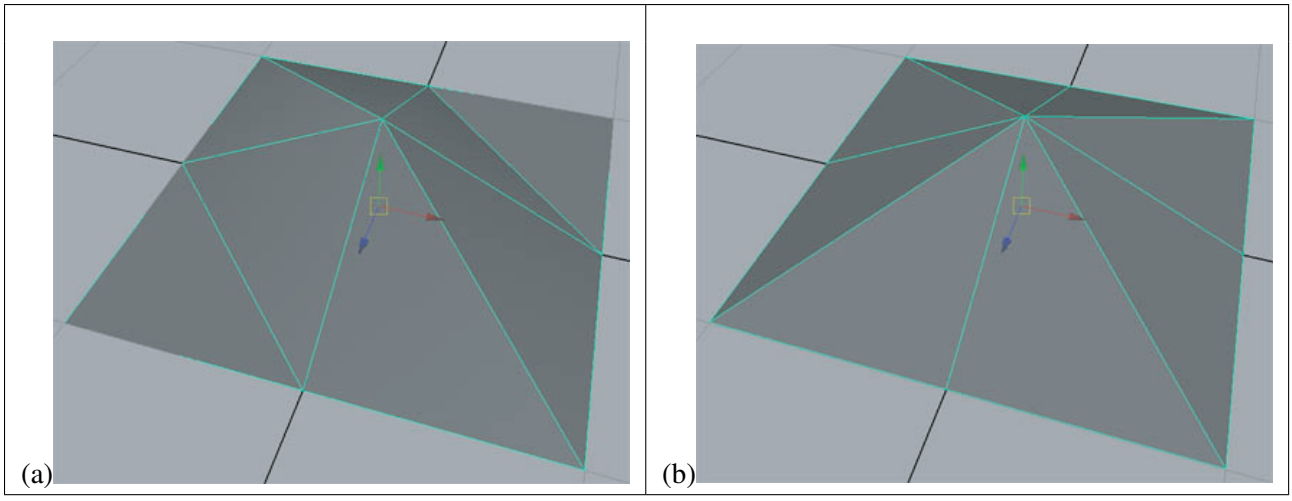

Figure 5.2: Two different surface triangle arrangements

from the top left to bottom right corner. Lifting the central vertex creates an irregular hexagon with 2 90^o corners and 45^o corners. Fig: 5.2b shows the arrangement in which the cut alternates between top left to bottom right, and top right to bottom left, for each adjacent square, creating the cross-hatch pattern. In this case, lifting the central vertex results in a square based pyramid of side-length 2 units. Since the aim of this model is to describe devices such as square based pyramids, arrangement (b) has been chosen as a default, although in principle it is possible to alter this.

5.1.2 Monte Carlo

Monte Carlo methods utilize a sequence of pseudo-random numbers generated in an iterative procedure in order to statistically sample a number of possibilities, or create randomized features. This model employs the Monte-Carlo method in two distinct areas; in the emission location of the rays, and in the surface properties, when modelling roughened devices. Generation of random numbers however can be problematic, and when using available functions such as the rand() function in C++, it is important to ensure that an even distribution is actually achieved. There are a number of cases where it is possible to inadvertently generate a non-even distribution of numbers. Issues regarding the uses of random number generators are covered more fully in Appendix C.1.

Monte Carlo Emission Position

Since the light is described initially as being emitted from each grid point, this limits the range of possible interaction angles (Fig: 5.3). If however the emission rays are randomly scattered over the area of the square, then the full range of possible interaction angles can be determined. The effects of this are quite clearly visible in a plot of the angular outputs (Fig: 5.4).

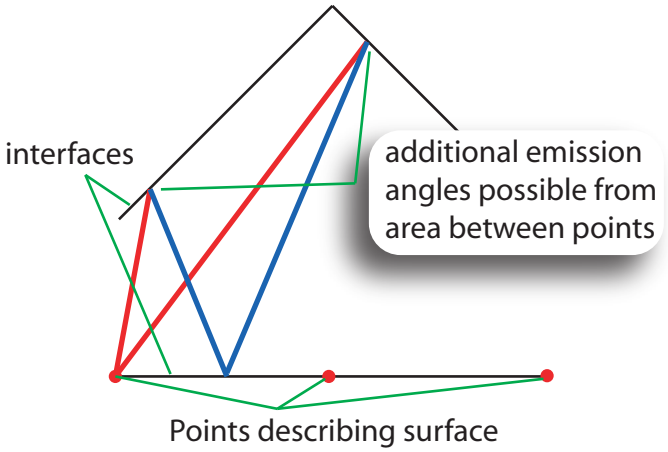

Figure 5.3: Limitation of Interaction Angles

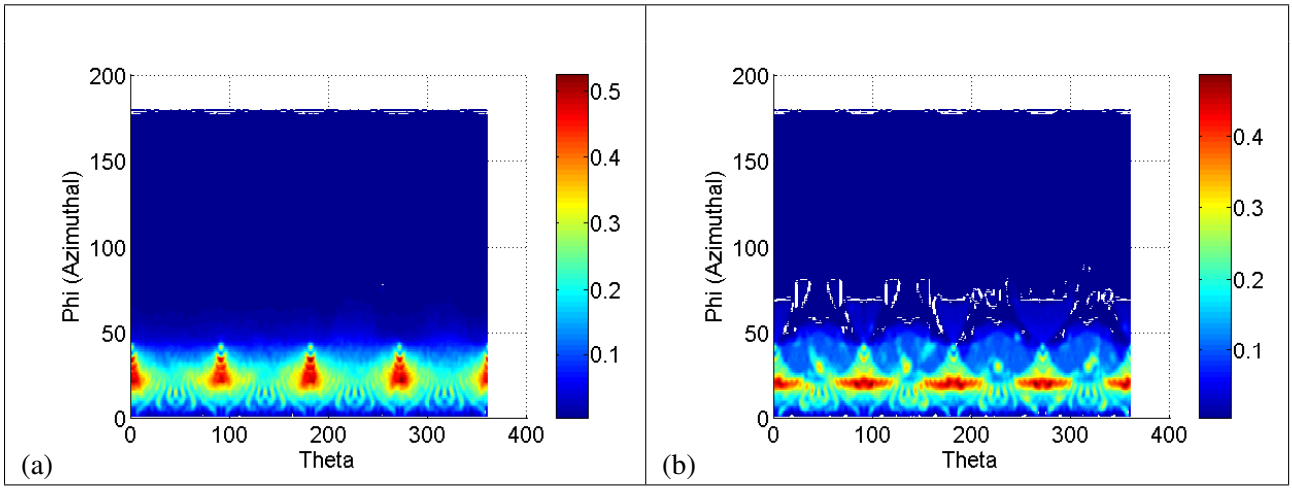

Figure 5.4: Emission (a)With and (b)Without Monte Carlo Positioning

Monte Carlo Surface Roughness

Description of roughened surfaces is more complex than repeated, regular surfaces, since to describe a roughened surface accurately would require many more polygons to cover the detail of the surface, which may contain a wide distribution of angles, and ranges of roughening of particular patches of the surface. The scale of the roughening may also be very small compared to the scale of the rest of the device, necessitating a very large array of points to accurately describe the interactions. Where the angles are relatively low however, and where the probability of multiple interactions with the same surface are correspondingly low, an alternate method of modelling surface roughening is possible. As the ray interacts with an interface, the angle of interaction is calculated from the ray vector and the vector normal to the interface surface. Perturbation of the surface normal alters the reflection angle of the ray. The perturbation can be generated using a Monte Carlo method. The limitations on this method are that the perturbation cannot be high, such that there would be multiple interactions with a polygon, since this would also require positional and depth information, which cannot be provided using this method. These multiple interactions are more likely to occur for high perturbation angles, and angles at which the light glances the interface at close to perpendicular to the interface normal. The model can create perturbations of either linear distributions, or normal distribution, using the polar version of the Box-Muller transform (Appendix C.1).

5.1.3 Grid Location

In order to model finite sized devices, or devices in which multiple emitters are used in different locations, it is necessary to limit the area of the grid covered by the device. At each grid point, there is an emitting object that contains the emission properties for that region of the display. If all the light is emitted from only these points however, there will be a large number of possible interaction angles that will not be represented. This can be dealt with by describing each feature of the device by many polygons and emission points, however this would be extremely processor intensive and impractical, hence the fractional distance of any particular emitted ray is generated randomly in order to ensure that the rays are well dispersed in each square described by the grid points. In

order to ensure that this method produces results in agreement with the alternate possibility of large grids, and that the spread of points is good, and hence not dependent on the starting number seed, a number of models have been produced and compared.

5.1.4 Interface Physics

For optical structures in which the device thickness is substantially thicker than the wavelength of light, diffraction effects can be ignored, and the light can be treated as rays. In the ray model, the distances between interfaces are calculated and then interactions with the interfaces calculated using appropriate solutions of Maxwell's Equations in the Fresnell Equations (Equations 3.4, 3.5, 3.6 and 3.7 on page 28) and Snell's Law.

For the metal-dielectric interfaces, the reflection angle is trivially calculated, and any transmitted light is considered to be absorbed. Calculation of the reflection coefficients however is complicated by the complex refractive index of the medium. While the formula remain essentially the same, the algorithm has to be altered, both to conserve computer time, and also to render the equation in a manner which is readable by the computer. See Appendix B

For dielectric layers, these are simply solved, however for materials such as metal interfaces, the angles and refractive indices are complex. For the purpose of the ray tracing model, the light transmitted through metallic layers is ignored, as the attenuation of metal layers is high, and so most of the light is absorbed within distances of the order of the wavelength of light, meaning that any light transmitted must be dealt with using thin film optics. It is possible in principle to replace the interaction on these interfaces with a thin film model in order to more accurately represent reflection and transmission from such layers. The reflections and transmissions from metallic and dielectric interfaces are dealt with separately.

In order to check the ray-tracing code, a number of basic tests were carried out. The simplest is to model an infinitely large flat plane. The result from this can be determined analytically and then compared to the ray-traced result. (Fig: 5.5) shows the analytical result for an infinitely large plane. All the light above the angle of total internal reflection is lost, amounting to a cumulative

light escape of 64% for a Lambertian emission into the substrate. For other emission distributions the figure will vary slightly from this value. Since the model does not assume perfectly reflecting edges, this percentage result will not appear correct initially, since 75% of the light will be emitted immediately outside the device. The emitted light from this initial device is 25% of the expected result for an infinitely large plane. Increasing the grid size improves the accuracy of the result. (Fig: 5.6). For these cases, all of the light emitted into the direction of the plane and not immediately away from it that is incident on the plane lies within the escape cone of the light, so the emission appears to be correct. For thicker devices however, where light that would be inside the escape cone, but passes right across the plane, there would be an increasingly significant cutting out of this light, as is seen in (Fig: 5.7). The amount of recycled light in these cases is not significant since only around 4% is reflected for low angles and above the angle of total internal reflection, all light is lost. The addition of Monte-Carlo placement of the ray emission point makes no significant difference, as the ray to surface-normal angle will remain the same regardless of emission position. A slight difference is observed, but this is due to some additional light being lost immediately from the device that would not have been lost if emitted from the grid point, and some that would have been lost now being reflected, creating a slight directional bias.

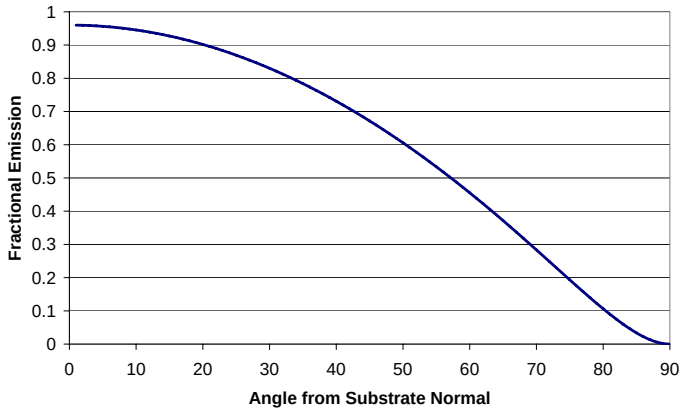

Figure 5.5: Analytically Calculated Light output for Infinitely Large Plane

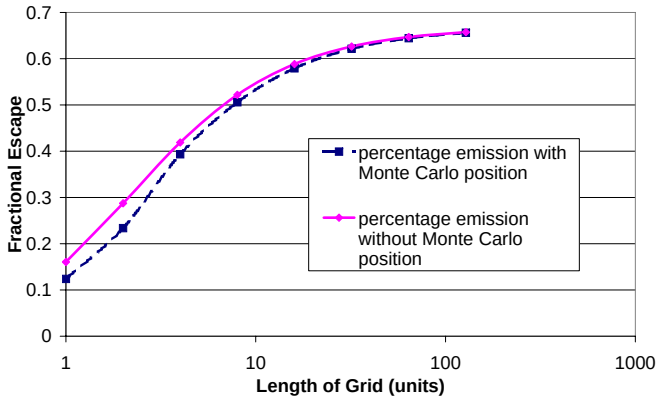

Figure 5.6: Improvement in Accuracy with Increased Grid Size

5.2 2 Dimensional model for simple rhombic structures

While some of the light trapped in the structure will be lost to absorption on the metal interfaces, for devices in which the ratio of substrate width to substrate thickness is high, the majority of light will be lost to edge emission, due to the small number of reflections from the metal surface before reaching the edge. Where the substrate is very thin but large, significantly more will be lost to absorption. For an OLED on a silver cathode, up to 95% of the light incident on the cathode is reflected, though this is affected by the layer structure. The intention of the work in this section is to find whether for devices of reasonable dimensions, a major part of the light waveguided in the substrate can be coupled out to the edge of the device. Constructing a simple 2 dimensional model of the structure allows the modelling of the adjustment of the edge properties in order to efficiently outcouple light. In this case the edges are treated as silvered surfaces, so that no light is coupled out of them. Emission only occurs through a single surface on the glass, with the OLED being treated as a silver surface.

5.2.1 Model

The model describes the device in terms of its fundamental parameters, such a thickness, refractive index, attenuation, OLED reflectivity and descriptions of end properties. The emission from the

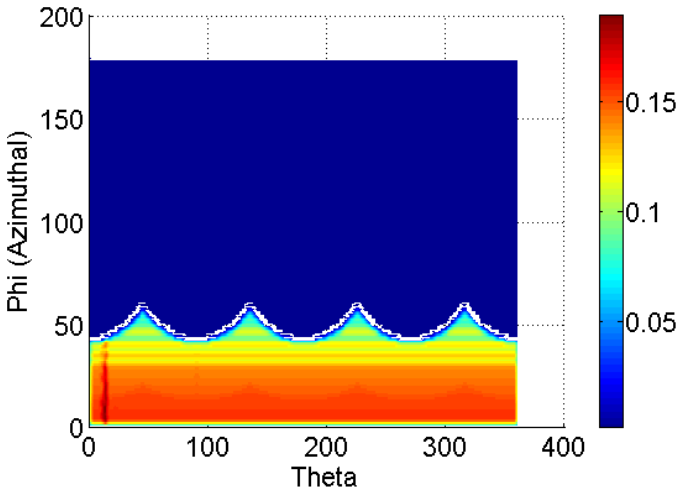

Figure 5.7: Cutting of Light from Escape cone for small, thick structures

OLED itself is treated as either a Lambertian emitter, or an emitter adjusted to take into account the various OLED emission properties. Interaction with the edges is based on application of Snell's Law and the Fresnel equations.

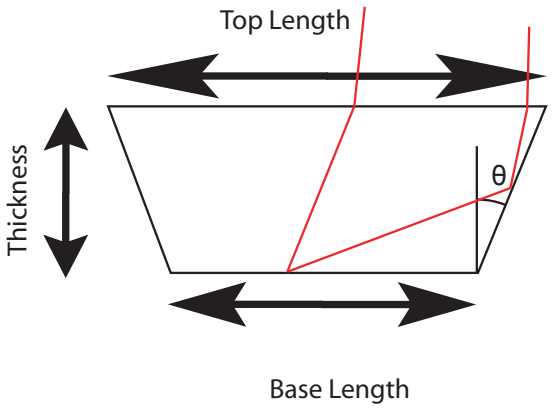

Figure 5.8: Basic Device Description

Fig 5.8 shows a schematic of the emitting device. The OLED emits into the thick substrate, for which the base length and top angles are set. The light is emitted from the top edge, and is then stored by fractional position along the top edge and emission angle. Multiple reflections are allowed. Negative angles of θ allow for a bottom that is larger than the top. The straight edge can also be exchanged for other edge structures, such as a parabolic chamfer.

The model allows for adjustment of a number of parameters in order to tailor the device to requirements.

5.2.2 Results

The main parameters to be investigated are, the attenuation in the substrate material A, the reflectivity of the OLED R_o, the reflectivity of the edges R_e the angle of the edges to the OLED normal θ and the base length to thickness ratio X is used. Analysis of these will determine the dominant factors in determining the device emission. To provide a control, a device with $A = 0$, $R_o = 1$ and $R_e = 0$ is chosen. The edge angle θ is chosen to be 45^o. While this does not have an effect on the quantity of the emission of the device since it is above the critical angle of the device, it does affect the appearance of the light emitted from near the edges of the device, as will be explained later. This effectively describes an infinitely large device, with no additional device losses, other than those due to total internal reflection. The amount of light escaping is compared to the light emitted from the OLED layer. The output of a device for a Lambertian emitter is 66% of the total emission into the glass. The profile of the emission with position and angle are shown in Figure 5.9. The "Chessboard" appearance of this result is a function of the angle and the base length/thickness ratio, and is caused by the variations in reflected and emitted light as the detector moves along the surface.

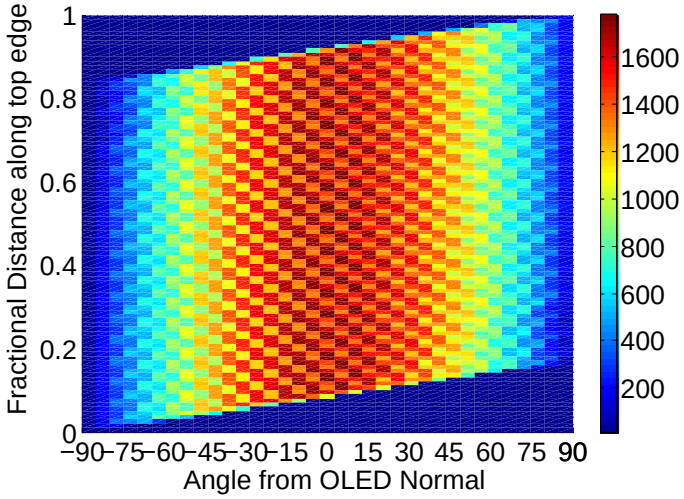

Figure 5.9: Simple Flat Device

The first factor to take into account will be the reflective edges and reflectivity of the base. The

angles are chosen for a range from -80^o to 80^o, and the reflection of the base and edges are also varied over a range as indicated (Fig: 5.10). In all cases the reflection from the edge is 100%. The ratio X is chosen to be 10. For this device, the total escape against angle are plotted in Figure 5.10, and for a range of base reflections. From this we find that the optimal edge angle for emission is 50^o. The edge emission is then varied over the range of values from 80% to 100% to analyze the effect on the emission (Fig: 5.11), and again for a range of angles to ensure that the optimal angle does not change. The ratio X is varied as shown in figure 5.12. At this stage none of the varied parameters are dependant on the actual values of the size of the device. Provided the device is kept in scale, nothing changes in the emission properties. The glass however is not perfectly transparent, and this is taken into account as percentage of light absorbed per unit length, in Figure 5.13, again for a variety of angles and absorptions of base reflectivity, to ensure that the optimal angles do not change. The same form is seen in all of the graphs, with an initial peak at around 30^o and the second peak at 50^o. It is clear from these that the peak emission angle remains at 50^o regardless of the other properties, and so further examination will take place at this angle only.

While it is apparent that the performance of the device will suffer with reduced interface reflection and increased material absorbance, it is not immediately clear what the effect will be on the particular form of the emission pattern. For a device with no edge reflection, the emission has already been shown (Fig: 5.9). Where there is edge emission however, the form of the ends changes as is outlined in (Fig: 5.14), for a standard device with $\theta = 50^o$ $X = 10:1$, $A = 0$ and $R_o = R_e = 0.8$.

The emission from this device is essentially the same as the device with no edge reflection over the bulk of the device, however there is significant additional outcoupling at the edges of the device, in the region of the angled edge. The triangular gap in the outcoupling free model is due to the absence of light being emitted from the edge of the top toward the centre of the device, but additional outcoupling occurs from this region due to reflections. The emission is shown for a number of different properties; different edge angle, different edge reflection, different base reflection and material absorbance of 6%, and a very low ratio X of 1:1 in order to show the effects of these different parameters on the outcoupling of light. Figures 5.15 to 5.19 refer to a standard

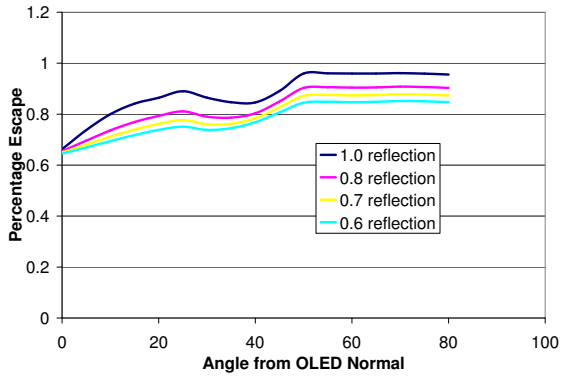

Figure 5.10: Escape against Angle

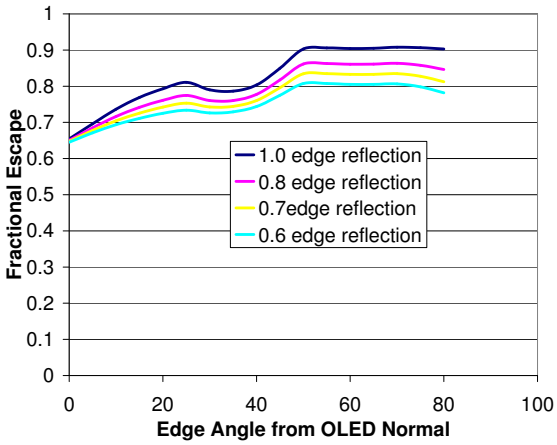

Figure 5.11: Escape against Edge Reflection

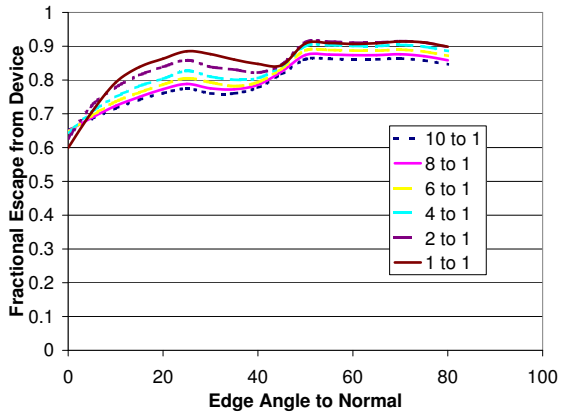

Figure 5.12: Base Length: Thickness ratio variation

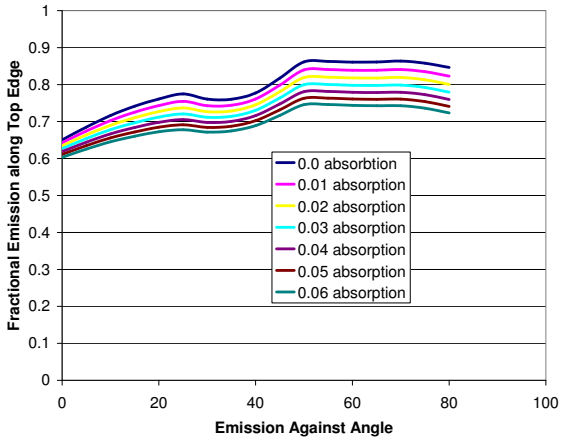

Figure 5.13: Variation of Absorption per unit length.

device as above, with identical properties, except where otherwise stated.

While the height scale of all the graphs is in arbitrary units, they are all normalized to the same value (the amount of light inserted into the device) with the exception of (Fig: 5.19, which has proportionally less light due to the small ratio. As can be seen, the reduction in reflectance and increase in absorbance reduces the light emission, as light is lost on reflection or transmission through the glass respectively. The effect of adjusting the angular properties of the edge is more subtle however, and involves the shifting of the emitted light peak to a different angle, and results in different amounts of light escaping after a first-pass reflection. The peak is at 50 degrees as a

result of two factors. Firstly, the light that is wave guided will all exist within the range of angles above θ_c, which for the glass modelled above is 42^o. On interaction with the edge, this light will be rotated through 50^o and hence will be immediately outcoupled. The sum of the angles is thus close to 90^o, but not perfectly so. The perturbation is due to the increasing reflection in light from the interface as seen when calculating the reflection with the Fresnel Equations, at angles close to the critical angle. The second factor, is that the chamfer angle is above the critical angle, and so does not interfere at all with the light that would escape immediately, unlike the lesser peak at 30^o, which also outcoupled light, but less so due to the additional loss of light that would otherwise have escaped had it hit the escape surface directly.

Fig 5.20 shows the emission for the full range of angles. Even negative angles (where the top surface is smaller than the bottom) see additional outcoupling, however the effect is not so pronounced, due to more light being reflected from the edge and OLED before escaping. The device with the low ratio X of 1:1 shows the greatest departure from the normal behaviour, due to the multiple interactions with the outcoupled light before escape through the top edge. This results in additional losses due to these reflections, degrading device performance in terms of both emission and control of angular properties. This effect depends on the particular angles of the edges, as can be seen in Figure 5.21, where additional losses occur for 5, 50 and 75 degrees, but not for 25^o within the range of ratios shown.

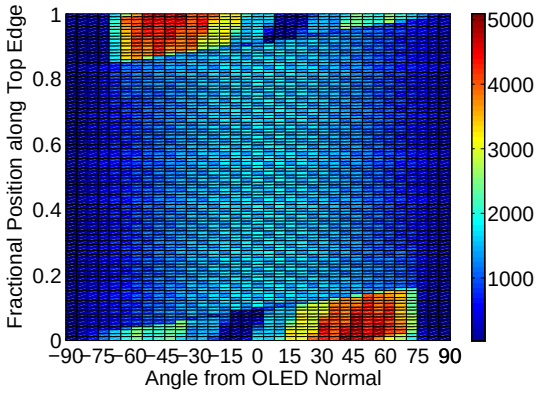

Figure 5.14: Standard Device

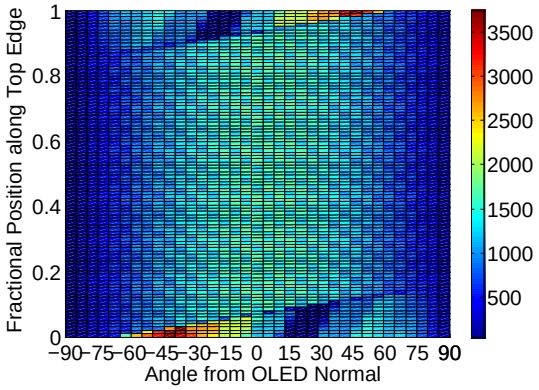

Figure 5.15: Standard device with 40 degree edge

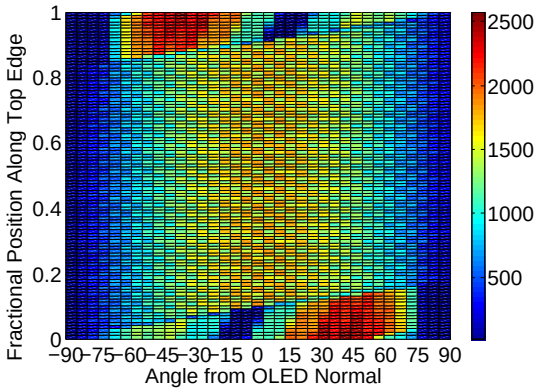

Figure 5.16: Standard device with 70% edge reflection

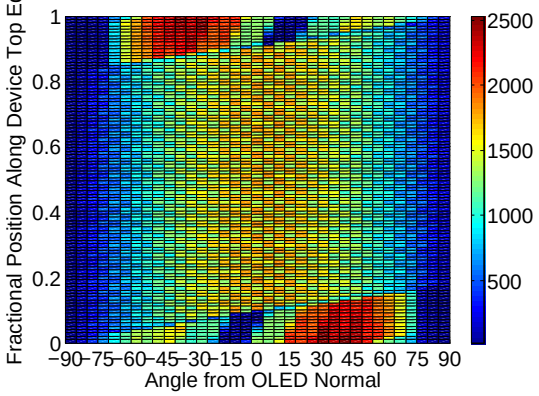

Figure 5.17: Standard device with 70% base reflection

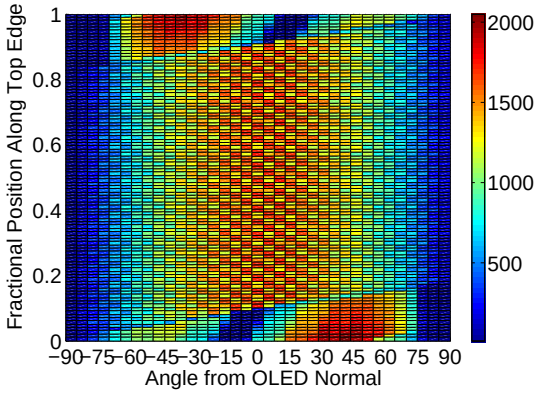

Figure 5.18: Standard device with Absorbance of 6% per Unit Length

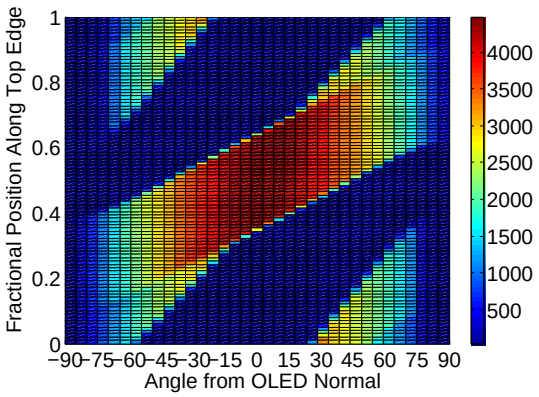

Figure 5.19: Standard device with ratio X of 1:1

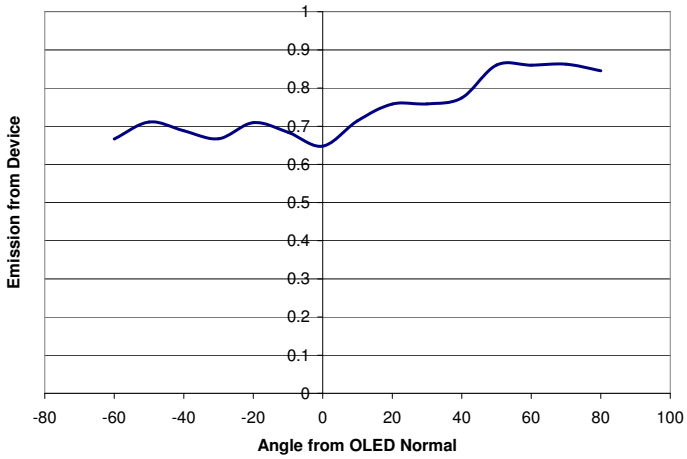

Figure 5.20: Variation of Emission against Angle for a full range of positive and negative angles

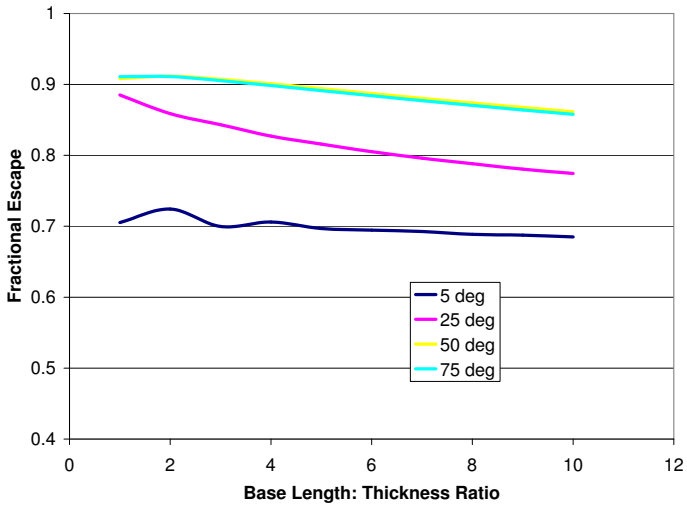

Figure 5.21: Variation of Ratio against Emission

5.2.3 Experimental Analysis of Outcoupling using Chamfered Edge.

A chamfered glass layer was made using a glass of refractive index $n = 1.5$ and absorbance of $6\%cm^{-1}$ was constructed, 0.8cm thick, with a base length of 8.6cm and an edge chamfering angle of 50^o. The acute angle was smoothed slightly for reasons of both safety and robustness. The centre of the glass was first masked, and then the edges were then coated in an 80nm layer of silver, in a Leybold LAB500 chamber using electron beam evaporation. The evaporation rate began at 10Åin order to ensure a homogeneous distribution of silver and small crystal size, then the rate was slowed to 1.5Å. The thickness of the layer was approximately 80nm over the sides. 2 notches were left on opposite sides to provide an area for manual handling of the glass. The metal layer was measured to have a transmission of 20^o. The OLED chosen was a white emitting OLED with a side length of 8.5cm, closely matching the base length of the glass. The outcoupling layer was connected to the OLED substrate using a Zeiss index matching oil, of refractive index $n = 1.516$ at 20^oC and then allowed to rest until the oil had spread to cover the whole OLED. The OLED was measured in an Autronic Melchers DMS100 Goniometer, over a 70^o range, and for a variety of different device positions, directly above the very edge of the device (Fig: 5.22), through the edge of the OLED and over the OLED.

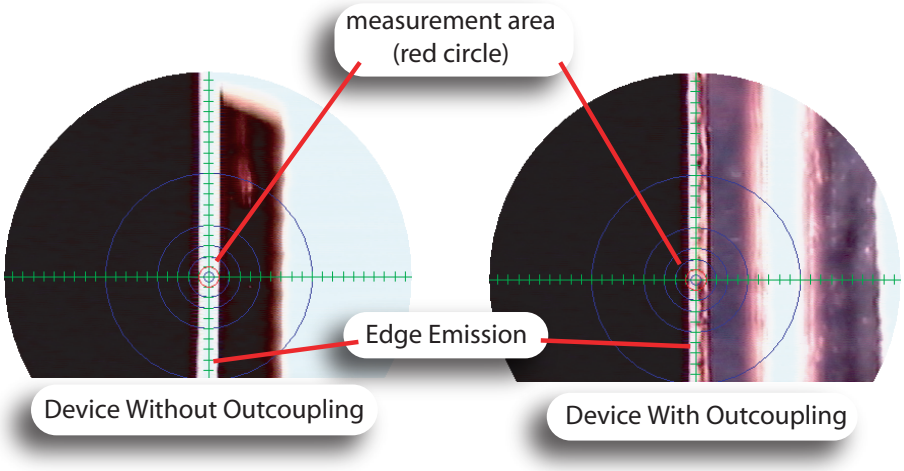

Figure 5.22: Emission through edge of device (1) without and (2) with outcoupling glass

The angular resolution was measured in 1^o increments. The emission from the edge, both with and without the outcoupling glass attached to the OLED was measured. For pictorial representation, the glass was also attached to an RGB emitter, with partial cover of the outcoupling oil in order to clearly show the outcoupling effects.

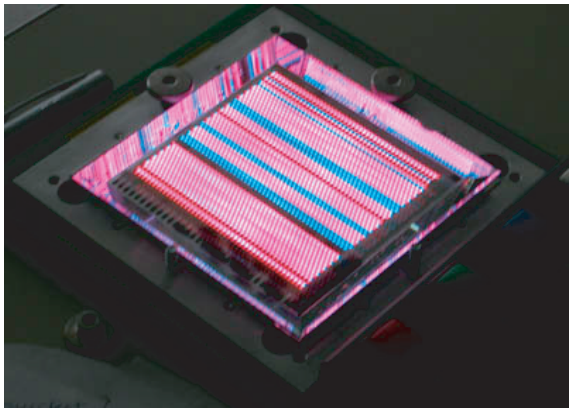

Figure 5.23: Outcoupled Light

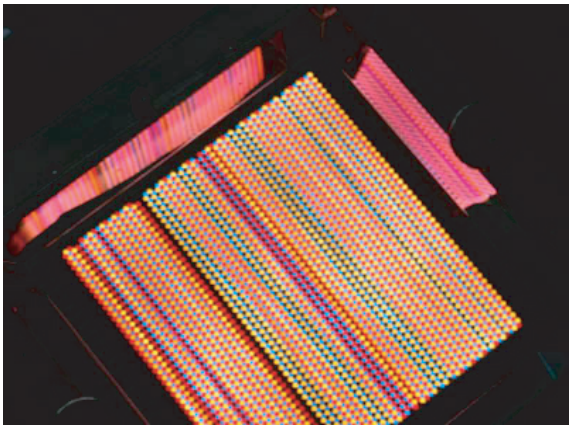

Figure 5.24: Outcoupled Light from Half Coupled OLED

In (Fig: 5.23) The reflected light from the chamfered edges is clearly observed. (Fig: 5.24) shows that where the index matching oil is not present, the outcoupled light is not observed. This is due to a thin layer of air between the two glass interfaces, resulting in no waveguided light escaping from the OLED substrate to the chamfered glass.

Goniometer Limits

Due to mechanical limitations (Fig: 5.25) it was not possible to measure the entire 140^0 range over a single point, however the symmetry of the system allows the results to be paired together so that measurements from the right side should match the negative angles from 0 to -70^o in the modelled results, and the measurements from the left match the positive 0 to 70^o results. Also due to the requirement of a finite spot size, it was not possible to measure right to the edge of the top surface. The results were then modified by multiplying by $\cos(\theta)$ in order to compensate for the Lambert Cosine Law, already taken into account in the model.

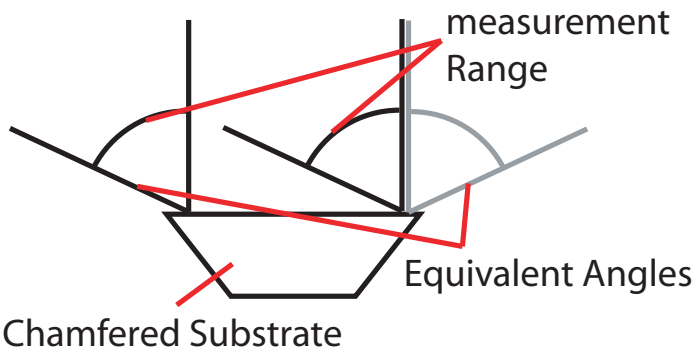

Figure 5.25: Limits and Equivalence of Goniometer Measurements

5.2.4 Comparison of Experimental and Theoretical Results

The same device was simulated, and the results compared (Figs 5.26 and 5.27)

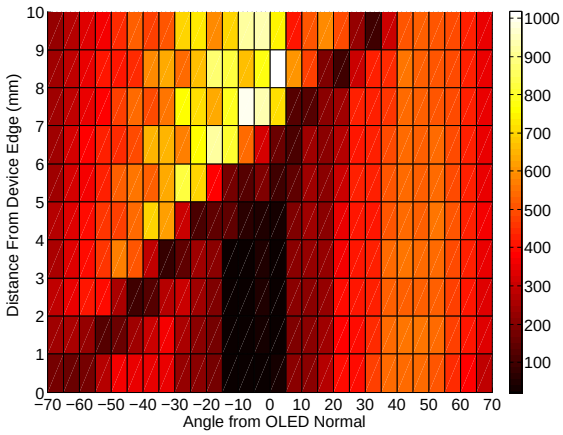

Figure 5.26: Experimental Measurements

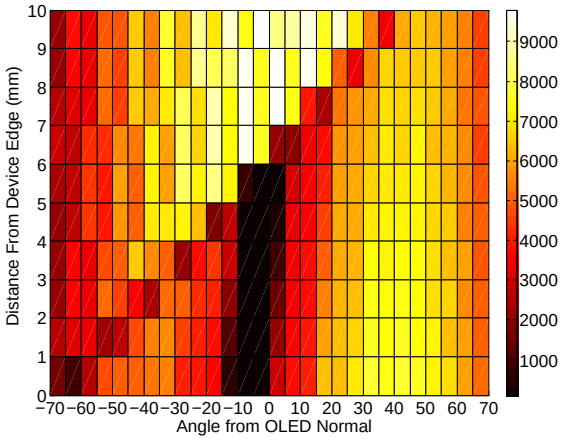

Figure 5.27: Modeled Device

The height units for the modelled data are arbitrary units, and for the experimental data show $cd \cdot m^{-2}$. The results are in broad agreement in form, though there are some differences which will be highlighted. The experimental data appears to peak more, due to a couple of abnormal peaks in brightness at 5 and -5^o. The gap in the forward emitting region of the outcoupling zone is also more pronounced in the experimental model, due to having to match the two sides of the device together to make one angular description, as described in 5.2.3. The calculated improvement in outcoupling

for this device is 12%, from 60^o to 72^o. This is relatively low, for this sample, but the low increase is due to the high attenuation in the glass, the thickness of the edge silvering allowing a relatively large amount of transmission, and the low reflectivity of the OLED.

5.2.5 Discussion and Conclusion

The reflective chamfered edges offer a good opportunity to improve device performance while having little impact on the complexity of the device as a whole. The OLED used in this test while highly reflective, was not designed for its reflective properties, and so addition of extra layers to improve the reflectivity can result in better overall device performance in terms of lighting applications. The simplicity of this method would also allow OLEDs to be deposited directly onto the substrate, totally avoiding wave guiding losses through the edges of the glass as observed in Fig 5.22.

While relatively low, even a fairly modest improvement in device parameters would result in a good overall enhancement, improving the reflectivity of the OLED and edge to 80% and 90% respectively and a reduction of the losses in the glass to 3% per unit length would improve device performance to 83%.

Further possibilities for improvement of device performance could involve etching in the central regions of the device. Due to absorbance and losses in reflection from the OLED surface, light passing through large distances of glass and reflecting multiple times will be greatly diminished, and outcoupling these at an earlier opportunity could result in additional gains.

5.3 3D Model for structured substrates

In order to outcouple light from a substrate into air, a number of methods of surface structuring have been proposed [2, 1]. However due to the various symmetries of these structures, there are often directional preferences to the light emission, and distortion of the images along alternate axes. One possibility is a more randomized surface roughening, which would have the advantage of widening

the escape cone of the light, while not suffering from the directional bias of conventionally structured substrates. Implementing this into the model is relatively simple, and involves a perturbation on the surface normal of the polygons describing the surface (Fig:5.28).

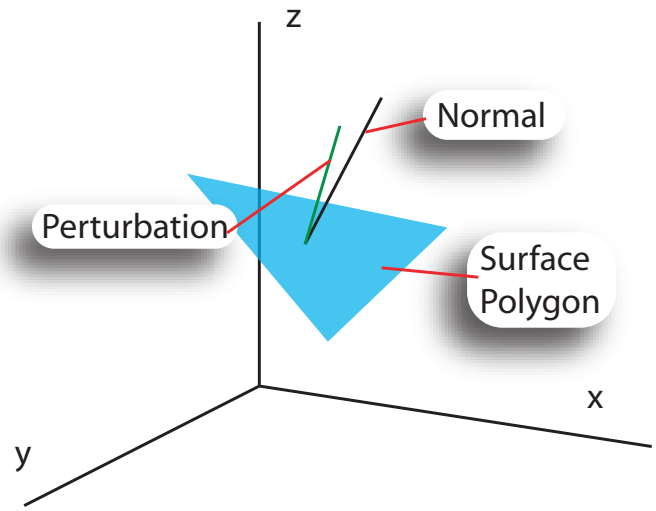

Figure 5.28: Perturbation to Surface Normal of Polygon

This perturbation makes the assumption that multiple interactions with a particular polygon will not occur. Since while an adjustment to the surface normal is made, there is no alteration to the position of the polygon. This means that this approach is not suitable to describe surfaces where the roughening is very deep or sharp, or to describe the multiple interfaces of structures such as pyramid arrays or microlens arrays, where multiple interactions over the scale of the structure are expected. As a result, rays transmitted or reflected at very high glancing angles to the surface are subject to inaccuracy. The gross surface structures however are still described by the polygonal model, allowing superimposition of roughened surfaces over the structures surface, or the simple inclusion of additionally roughened interfaces, for example, between the substrate and an additional outcoupling layer, or alternatively as backing layers behind the emitter. There are three main parameters to consider when modelling randomly structured surfaces. The first is the percentage cover of the randomization. This allows for areas to be unperturbed. The presence of perturbation at a point may be considered to be random, if the thickness of the substrate is such that the lateral distance travelled

by the ray after the reflection from the roughened layer to its next interaction with the roughened layer is larger than the mean feature size of the roughened portions of the display. The next is the range of angles over which the normal may be perturbed; smoother surfaces will see a smaller range of possible perturbation angles than rougher surfaces. The final parameter is the distribution of the angles, which coupled with the range of angles, allows a more detailed description of the jaggedness of the surface. The depth of the features is not included for the reasons described above. To include depth would require precise modelling of the structure in terms of polygonal elements, which would be excessively processor intensive and impractical.

5.3.1 Experimental Description

In order to ensure repeatability of results, the OLED substrates were not patterned directly. Instead 0.8mm thick plain glass sheets were roughened using a Matthes ST700PS sandblaster using a coarse sand at a variety of pressures and for a variety of time spans, and then these were connected to IPMS produced 4 quadrant OLEDs, with a quadrant size of 8mm square, in a variety of combinations, with and without index matching oil. Where the oil was used, it was using a Zeiss index matching fluid (n=1.518 at 23^o). An untreated glass sheet was also used as a control. The sheets were then analyzed in a number of positions using a profilometer and a Veeco NT1100 White Light Interferometer, over patches of area $150 \times 200\mu m$ in order to determine the properties of the roughening (Fig: 5.29), and analysed more directly under a microscope in order to determine the approximate area cover of the roughening. The results for the measurements are shown in table 5.1 where 'Pressure' and 'Time' relate to the sandblaster settings during production, 'Ra' and 'Rt' are the valley to peak heights and peak to peak distances respectively. θ_c is the rms angle of the roughness and $\delta\theta$ is the spread, and finally the Percentage cover is the percentage of the particular devices that were roughened.

OLEDs of different colours were used, giving a broad colour spectrum over which to test the devices. The devices were then analysed for a variety of angles in an Autronic Melchers DMS 401 Goniometer up to an angle of 70^o with a measuring spot size of 2mm. Angles higher than 70^o were not possible due to the geometry of the OLED and Goniometer (Fig 5.25 and Appendix A).

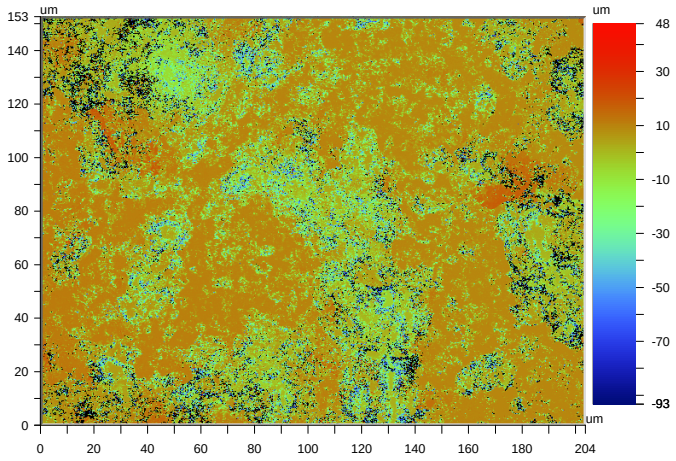

Figure 5.29: White Light profile of Roughened Substrate

Key Physical Properties of Roughened Devices						
Device	Pressure (bar)	Ra (μm)	Rt (μm)	θ_c (^{o})	$\delta\theta$ (^{o})	Percentage Cover
Plain	0	0	0	0	0	0
Light	2	10.2	137	4	2	17
Medium	2.5	16.0	138.2	6.5	4.5	60
Heavy	3	14.3	137.2	5	4	78

Table 5.1: Key Physical Properties of Roughened Devices

As the angle to the OLED plate increases, the measuring spot covers a correspondingly larger area of the OLED. Under low angle circumstances this can be taken into account, however for higher angles, multiple reflections within the OLED substrate become a significant issue, since there will be increased, and not easily calculable drop-off at high angles.

5.4 Comparison and Conclusion

The analysis shows that the mean valley widths, depths and thus perturbation angles do not vary strongly with the different production methods. The main diagnostic difference between the sampled devices centres on the percentage cover of the roughened areas, varying between 15% and 75% roughness. Entering these parameters into the ray tracer shows that the monte carlo normal

perturbation method functions as expected. The model agrees with the measured spreads of angles and coverage at higher angles, however it appears in general rougher than the emitted light. This is due to a number of factors, principally the relatively low number of rays used to describe the device in the model. A further error occurs in the model at low angles, this is an artefact of the perturbation which results in light incident at low angles being lost

Figure 5.30: Emission from Roughened Devices.

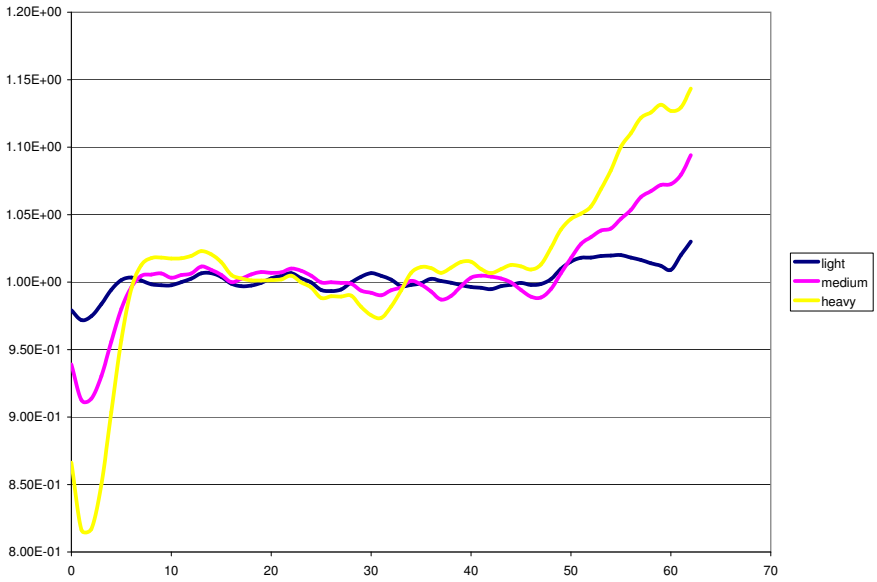

Figure 5.31: Simulation of Produced Devices.

5.4.1 Emission from Hemicylindrical Prism

Since the emission from the OLED may be waveguided, it is possible to pick a structure in which no waveguiding can take place. One example of this is a hemispherical substrate, with the OLED at

the very centre - for all points on the glass air interface, the OLED is in the line of the normal. If the OLED, or areas of the OLED, for example in a large area substrate, are positioned away from the focal point of the prism, then there may be varying amounts of waveguiding, such as "whispering gallery" modes, in which repeated glancing reflections guide the light along the interface. Eventually the light in these modes will be lost due to absorption in the substrate, and losses on reflection from the metal cathode and losses in the OLED materials. While the substrate is cumbersome and impractical for real world usage, it provides a useful test bed, since it is easily described. A red 2x1mm OLED was mounted in the goniometer, and analysed to measure initial output, and then a hemicylindrical prism was attached and the emission analysed again. One additional complexity due to the thickness of the prism (radius 2cm) was that the focal point of the goniometer appeared to move. In general the centre of rotation of the goniometer is set as close as possible to the plane of the OLED itself. Due to the refractive index of the material, for higher angles this results in the measuring spot pointing at different areas of the OLED as the angle is changed, however for thin substrates this difference is negligible and remains well within the boundary of the emitting region. In order to maintain the same optical distance between the detector and the OLED, one would expect to have to take into account the optical thickness of the substrate. For such a thick substrate however, this is not possible. The system was lined up with the rotational point centred on the OLED and then the prism added afterwards. The hemicylindrical prism was chosen over a hemisphere, since positioning is much simpler, as the goniometer rotates only in a single plane - within this plane the symmetries are the same in both cases. The OLED is then modelled in the Ray Tracer, both for the flat substrate emission and the emission through the prism. The emitting area from the model was only considered in a small patch in the centre of the substrate, since this is the optimal emitting region. For the purpose of discussion, two axes will be defined, the hemicylinder will be prismatic in the x axis; that is for a given value of y, the height of the prism will be the same for all x (Fig: 5.32). The circular angle ϕ is oriented such that $\phi = 0$ and $\phi = 180$ are oriented in the positive and negative y direction respectively.

In principle, barring a small amount lost to reflection from the air glass interface and subsequent

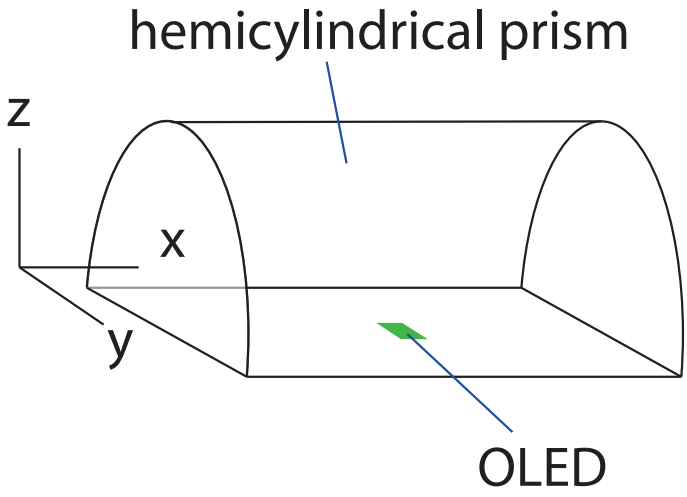

Figure 5.32: Orientation of Hemicylindrical Prism

reflections from the OLED surface (a maximum of about 4% for a prism glass refractive index of $n = 1.5$ all the light emitted into $\phi = 0$ and $\phi = 180$ should be emitted. Light emitted along the x axis at $\phi = 90$ and $\phi = 270$ should be emitted with the same properties as a flat device, since this is the point at which the normal of the prism-air interface is the same as the normal of the OLED, as is the case in all directions for a flat plane. The results can be seen in figures 5.33 and 5.34. The improvement in emission in the forward direction is close to 1.5, and drops toward the higher angles.

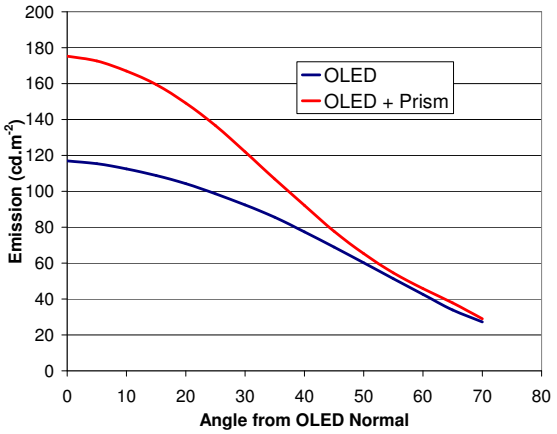

Figure 5.33: Comparison of Emission With and Without Hemicylindrical Prism

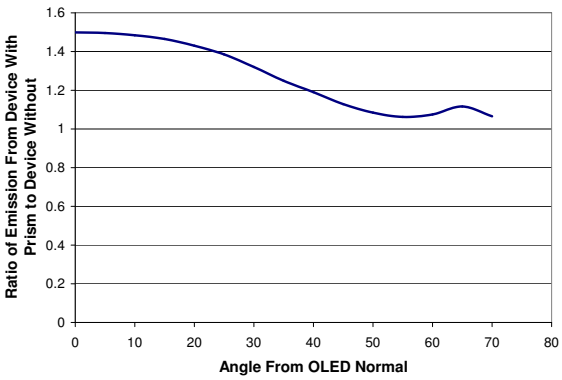

Figure 5.34: Ratio of Emission With:Without Prism

Bibliography

[1] H.J. Peng, Y.L. Ho, C.F. Qiu, M. Wong, and H.S. Kwok. Coupling efficiency enhancement of organic light emitting devices with refractive microlens array on high index glass substrate. *SID Digest 04*, 1:158, 2004.

[2] S. Tanaka, Y. Kawakami, and Y. Naito. Improvement of the external extraction efficiency of OLED by using a pyramid array. *Proceedings of SPIE*, 5519:184, 2004.

[3] P. Melpegiano, S. Sinesi, G. Rotaris, M. Antonipieri, F. Cicoira, M.A. Loi, M. Muccini, R. Zamboni, M.T. Gale, and S. Westenhöfer. Optical coupling of flexible microstructured organic light sources for automotive applications. *Synth. Met.*, 139:913, 2003.

[4] S.M.P. Blom, H.P.M. Huck, H.J. Cornelissen, and H. Greiner. Towards a polarized light-emitting backlight: micro-structured anisotropic layers. *Journal of the SID*, 10:209, 2002.

Chapter 6

Conclusion and Outlook

For OLED devices, it is in principle possible to maximize the light outcoupling by adjustment of the layer stack to optimize it's properties according to particular emitters. Due to the broad band emission properties, and the increasing requirements to enable devices to emit white light, or cope with emission of RGB light for displays this matter is complicated somewhat due to the highly wavelength dependent nature of the OLEDs. Also critical is the sensitivity of the device structure to variations in the thickness of the layer stack. As was observed in Sections 4.7.3 and 4.7.4 on variations in the thickness of the Hole Transport Layer (HTL) and Electron Transport Layer (ETL) respectively, the emission can be sensitive to a change in thickness of just a few tens of nm. Due to the proximity of the emitting layer to the metal cathode, this effect is significantly more pronounced for variations in the thickness of the ETL, and additional layers such as Hole Blocking Layers (HBL) between the emitter and cathode. The variation as expected is oscillatory, with the emission varying between better and worse for increasing thicknesses. While the interference properties are not significant for the thick substrate, due to the low spatial and temporal coherence of the OLED, they may still cause significant issues under certain scenarios, such as the result of the air gap between the OLED and encapsulation layer as seen in 4.8. In this case the glass plate was oriented in such a way that an interference structure was set up, resembling a Fabry-Perot (FP) etalon. In the forward direction, this resulted in strong interference effects in a number of devices, and in all cases

the interference strength diminished rapidly with angle. This differs from a number of reported applications and studies of FP effects, which use the OLED itself, and two metallic electrodes, one of which is generally transparent, in order to to tune and adjust the outcoupling properties of the OLED [1]. While it was only possible to carry out a limited analysis of the etalon, due to the haphazard way in which they were produced, it still demonstrated an interesting result, which could be used to further probe the properties of the OLEDs, and possibly even may be used as an aspect of an angular sensor or other devices, after the effects have been more clearly studied and quantified. Outcoupling from the OLED into air faces a number of issues, depending on the particular purposes of the device. For display applications, it is necessary to preserve the pixel quality of the display. That is, there must be little spreading of the light over the area of the OLED. This can present a problem for patterned substrates, as their primary method of improvement of light outcoupling is through recycling of the light; reflecting the light from the substrate-air interface to the OLED and back in such a way that on the subsequent interactions it may meet a surface in which outcoupling is possible. Improvement of outcoupling using thin film layers deposited on top of the substrate and modifying the substrate air interface is in principle possible, but the thin film stacks are in general angularly and wavelength dependent. For OLED devices, with their broad spectral range, these methods are not always appropriate. For lighting applications, the complexities are not as great. The visual quality of the light is not usually of any great importance and so particular distributions of light over the area of the OLED are not required. Due to the near-Lambertian nature of the emission, the light is emitted as such that the brightness of the display remains constant, regardless of viewing angle. This means that the majority of the light is emitted toward the forward direction, however significant light is still emitted at higher angles, and for angles above the critical angle this light is lost into the device. A number of methods have been proposed to outcouple this light, such as structured substrates, however these suffer from the problem that they take light that would normally have been emitted directly, and couple it back into the device, resulting in one or more reflections from the OLED. As the reflectivity of the OLED is often quite low (in the region of 60-70%) this can result in a large loss of light, counteracting much of the gains seen. An alternative was presented

whereby only the waveguided light could reach a region in which it was outcoupled, and this region did not affect the outcoupling of the escaping modes. This results in an increase in light emission without the losses associated with other methods. Again this method suffered however from light loss due to multiple reflections of the waveguided light from the OLED and also absorption losses in the material, however with improvement in substrate choice and possible improvement in OLED reflectivity, these problems could be reduced. While an improvement in these properties would also benefit structured substrates, this solution has the advantage that it requires very little modification to the glass substrate onto which the device is deposited, and also requires no additional techniques for manufacture, such as stamping or etching processes required for polymer and glass outcoupling structures respectively.

The work on outcoupling can be split into two broad sections; outcoupling for displays and lighting applications, where displays may be any kind of information display from signage to video monitors. In both cases the efficiency of outcoupling can be improved further by careful material selection, limiting the waveguiding to modes in which the light will not be rapidly attenuated due to absorption and reflection, for example in the OLED layers. For lighting applications, It would be useful to focus on the improvement of reflection of the OLED stack, so that for light recycling methods of outcoupling as outlined in chapter 5 are limited less by the path the light must take before escape, and can thus be focussed more strongly on light distribution. This approach however is not so suitable for display applications, as higher contrast is required between light and dark regions of the display, and this will be lost with high reflectivity. For this, the main focus must be on ensuring that light incident on the device is not reflected, whereas internally generated light escapes.

Bibliography

[1] C.J. Lee, R.B. Pode, D.G. Moon, J.I. Han, N.H. Park, S.H. Baik, and S.S. Ju. On the problem of microcavity effects on the top emitting OLED with semitransparent metal cathode. *physica status solidi*, 201:1022, 2003.

Acknowledgements

I would like to thank the Fraunhofer IPMS, Dresden for the opportunity to work there, and more specifically the OMS group headed by Jörg Amelung and Prof. K. Leo, as well as the BMBF for financial support. My thanks also go to my colleagues there with whom I had many fruitful conversations and of course Prof. K. Leo for his encouragement as well as supervising me and checking the many revisions of this thesis. I'd like to thank Klaus Luber and the people working on the inline for making many devices for me to study, as well as Qiang Huang and Gufeng He for the interesting Top Emitting devices made at the University.

My thanks also go out to my Dad, family and friends , who have helped me keep my sanity and to Andrew Copland who put up with my endless questions on floating point errors and pointers to functions.

I have endless appreciation for my wife Liang Qiao, without whose help, discussions, pushing, love and cups of tea, I really couldn't have done it.

This is also for my Mum and those who couldn't make it this far, I'm sorry you couldn't be here to enjoy this.

Appendix A

Measurement Limitations using the Autronic Melchers Goniometer

A.1 Spot Size and Multiple Reflections

The Autronic Melchers DMS 401 Goniometer (AMG) is the primary device for measuring the emission properties of the OLEDs, allowing the measurement of the spectral radiance from particular areas of the OLED at different angles. A spot size is chosen, using the supplied software, and after a calibration measurement, the AMG then finds the spectral radiance for a range of variable parameters, such as voltage, current, angle or position on the OLED. No adjustments to the measurements are made for angle, and so at some angle to the OLED, the AMG measuring spot covers an area of $A/\cos(\theta)$ where A is the area of the spot (Fig: A.1), and theta is the angle of the detector to the normal of the OLED plane. For higher angles there is an increase in the amount of internally reflected light, and hence an increase in the amount of light escaping after having been reflected from the substrate air interface, and from the OLED, one or more times. This then presents an additional area for finite area OLEDs, since higher angles can receive a lower number of reflections before straying off the area of the OLED (Fig: A.2). This effect is particularly noticeable when the same spot size is used for OLEDs of different size. Four devices of different sizes, all deposited on a

single substrate in the same run (so ensuring the uniformity of their properties), were analysed, with a measuring spot of 0.5*mm* radius for a range of angles from 0 to 65^o. The devices were all square devices, with edges measuring from the largest to the smallest, 9*mm*, 4.5*mm*, 2.25*mm* and 1.125*mm*. The latter was the limiting factor in the angle, since it was not possible to angle the goniometer such that the entire measuring spot remained on the area of the OLED. The results are presented in Fig: A.3, and show clearly that this measurement issue presents a problem if not taken into account.

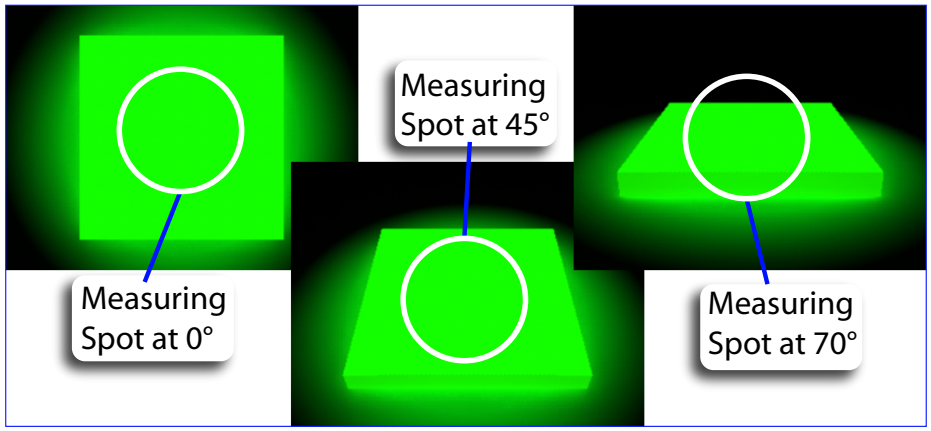

Figure A.1: Schematic of Area of Spot Superimposed on OLED area

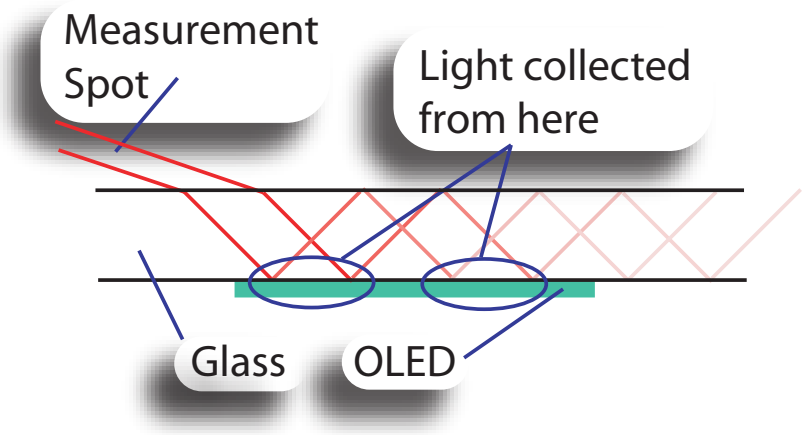

Figure A.2: Multiple reflections within OLED substrate

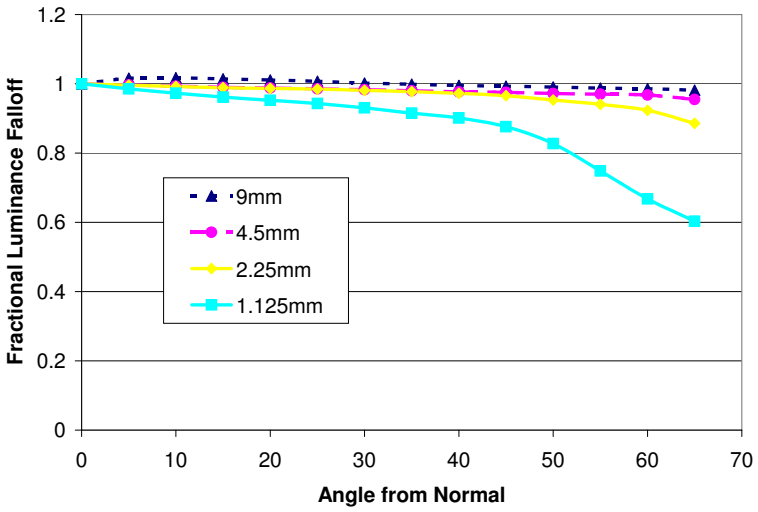

Figure A.3: Detected light from different sized OLEDs, all using a 1mm diameter spot

It is not feasible to take this drop-off effect into account when calculating the efficiencies and other relevant values of the OLEDs, since it depends on precise knowledge of the position of the spot over the OLED at all times, and would not have an analytic solution. Hence it is important to avoid this problem, and ensure that even at high angles, the position of the spot is such that this effect is minimized.

A.2 Accuracy of Device Efficiency using Autronic Melchers Goniometer

When analysing the emission from the device as a whole it is typical to assume a Lambertian emission, in which the luminous intensity appears to drop off like $\cos(\theta)$. It is well known however that the OLED is not actually a perfect Lambertian emitter as a result of the angular effects of the thin film stack.

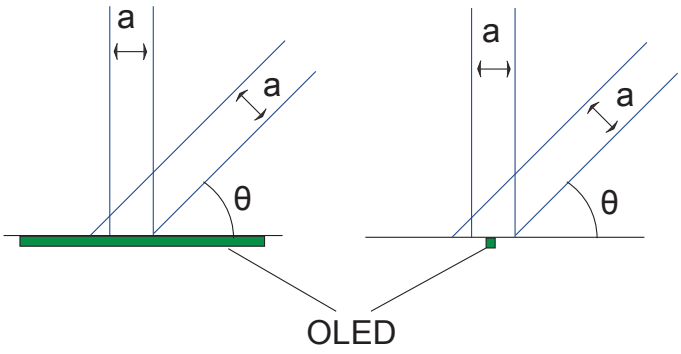

Figure A.4: Area of large and small OLEDs observed at different angles

There are two main ways to measure the devices using the Autronic that give importantly different values. Firstly one may, if the device is small, position the entire device under the measuring spot and then change the angle (Fig: A.4). For this measurement type, a Lambertian device appears as a diminishing $L_0 \cos(\theta)$ where L is the Luminance at the device normal. Alternatively a small spot on a large device may be analysed (Fig: A.4). For this case, when the spot does not cut the edges of the device a Lambertian device would appear as a constant luminance, since while the emission from any point is decaying like $L_0 \cos(\theta)$, the area of the device being measured changes like $^{a}/_{\cos(\theta)}$ where a is the area of the measuring spot. The latter method has been chosen for measurement since the device has an area of 10x10mm and so will not fit completely under the measuring spot. In order to calculate properly the power efficiency, one must then multiply the output by $\cos(\theta)$ in order to factor back in the constant device area under examination, since the integrating sphere measures the complete device.

Theory

The power efficiency of a device η of a device can be calculated from the luminant flux of a device M, and the power of the device by

$$\eta_E(ext) = \frac{M}{JV} \tag{A.1}$$

where J and V are the operating current and voltage respectively.

The luminance at an angle θ is a function of the luminance at the normal to the device L_0 and some function of the device angle $f(\theta)$

$$L(\theta) = L_0 f(\theta) \tag{A.2}$$

Integrating this over a hemisphere gives the total luminant flux

$$M = \int_0^{\frac{\pi}{2}} 2\pi L(\theta) \sin(\theta) d\theta \tag{A.3}$$

for a Lambertian emitter, $f(\theta) = \cos(\theta)$, however a correction factor K is required for non Lambertian devices, where

$$K_L = \frac{M}{M_0} = 2 \int_0^{\frac{\pi}{2}} f(\theta) \sin(\theta) d\theta \tag{A.4}$$

The final corrected power output is

$$\eta_E(ext) = K_L \frac{\pi L_0}{JV} \tag{A.5}$$

Experimental Method

At the Fraunhofer IPMS, the devices were tested three times in order to ensure stable device functioning, particularly given the hot and humid conditions in the laboratory on the first two runs. The

first run was completed one day after the devices arrived, the second three days after and the third seven days afterwards. The first run was carried out from 0-70 degrees, and the second and third from 0-80 degrees (the limit of the Autronic). The devices displayed stable characteristics over all three runs, with device 7 showing a slight deviation at high angles on run 2 that was not replicated in run 3. This is most likely due to experimental error, and the measurement spot running slightly off the OLED. Given that all three sets of data are approximately the same, the analysis will only be performed on the third set of data.

The VIPER evaluation program can evaluate the data in a number of ways, and can output the data either in terms of raw emission spectra against angle, or can calculate the luminance of the device in cd/m^2. In this case it was necessary to integrate directly from the spectral information, the units of which are $Wm^{-2}sr^{-1}nm^{-1}$.

For this particular device, there is a modification such that more light escapes the device than would be expected from a Lambertian emitter; this is common in these devices as a result of micro-cavity effects suppressing forward emission.

Results

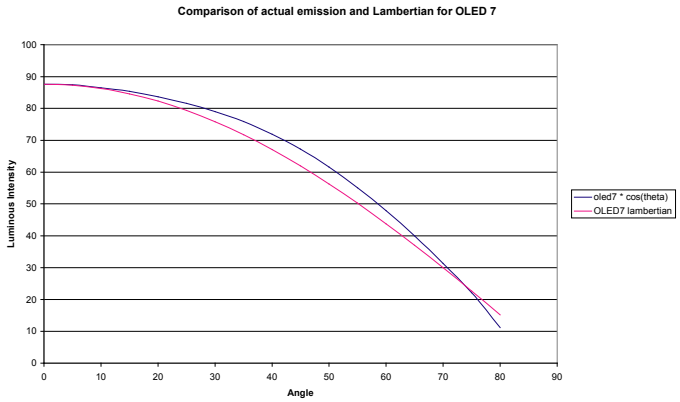

Figure A.5: Comparison of actual and assumed Luminous Intensities with angle

Fig A.5 shows the difference between the Luminous Intensities for the Lambertian and the real

measured emission, with the Lambertian calculated from the same Normal value as the measured emission.

The integrations and hence the numerical efficiency function $f(\theta)$ are numerically integrated for each of the 17 measured points from 0 to 90^o.

This allows us to find the true external power luminous efficiency $K_L\eta_E$):

Corrections to Run 3			
Device Number	Correction Factor	(η_E) (lm/W)	($K_L\eta_E$) (lm/W)
7	1.029	50.7	52.3
8	1.040	51.7	53.3
9	1.031	50.6	52.1

Table A.1: Correction Factors for OLEDs

With each of the devices running at 0.2mA at a voltage of approximately 2.6V.

For these devices, the correction factor is small, in the order of 4% for all three devices, with some slight change between each measurement.

Appendix B

Fresnel Algorithms

The Fresnel equations (Equations 3.4, 3.5, 3.6 and 3.7 on page 28) are used to describe the interaction of the EM field with the boundary, and their derivation is well documented. The four equations describe the reflection and transmission at the boundaries of two interfaces, for both perpendicularly and parallel polarized light (Fig: 3.4).

In order to calculate the reflection and transmission coefficients, one requires to know the incident angle θ_1 and the refracted angle θ_2. These can be found from Snell's law

$$n_1 \sin(\theta_1) = n_2 \sin(\theta_2) \tag{B.1}$$

where n_1 and n_2 are the refractive indices in the incident and refracted medium.

For the purposes of solution then, it is necessary to find the values of theta, both for incident as well as reflected and refracted components. For the case of total internal reflection, which occurs when the incident angle is at the critical angle θ_c (when the refracted angle is 90^o, found from $\frac{n_1}{n_2}\sin(\theta_1) = 1$) or higher, then there is no refracted component, and so the reflection is simply treated as total internal reflection, with no losses on the boundary.

For metals however the treatment is not as simple. Since the refractive indices of the two media n_1 and n_2 are actually complex; $n = \Re n - i\Im n$, the resultant transmitted angle deduced from Snell's

law must also be complex. While the actual transmitted light is rapidly absorbed in the metal and thus will not be considered within this model, it is still necessary to find the reflection coefficients. Since the refracted angle θ' is never used other than in the form $\cos(\theta')$ or $\sin(\theta')$, it is not necessary to calculate θ'. $\sin(\theta')$ is found from Snell's Law, and $\cos(\theta')$ is found using the identity

$$\cos^2 A + \sin^2 A = 1 \tag{B.2}$$

and ensuring that the correct root is chosen:

$$\cos(\theta') = \sqrt{1 - \sin^2(\theta')} \tag{B.3}$$

Appendix C

Monte Carlo Methods

C.1 Random Number Generation

C++ functions such as rand() generate a reasonably uniform pseudo-random distribution of numbers between 0 and some maximum number, defined as RAND_MAX (an integer value of 32767 in Visual C++). When using these values to generate random numbers within a certain range, it is important to take certain factors into account. Where the code is generating large numbers of random numbers, it is important to minimize the time required to adjust the random number from that generated, to the range required. Two simple methods are the conversion of the random integer and RAND_MAX to a float, find the ratio and then multiply by the maximum required value. Alternatively utilize the modulo operator, setting the value to the maximum value required and then having the remainder set to be the required number. The problems with these methods are that, in the first, it requires a larger number of function calls, in converting between integer and float. The complexities for the latter are slightly complex, and are best explained with an example.

Efficient Use of Modulo Operator to find Random Number in Desired Range

If RAND_MAX is a number like 256 and the required range is between 0 and 99, we would find the random number using

```
rand() % 100;
```

The problem is that since RAND_MAX is not divisible by the required range (100) this would create an increased likelihood of returning the numbers between 0 and 56. In order to solve this problem, it is best to form a do-while loop, and when the value is outside the largest number divisible into RAND_MAX (200) then the loop is repeated:

```
int x;
int max = (RAND_MAX - (RAND_MAX % range));

do
{
        x = rand();

} (while x < max);
```

The probability of repeat depends on the ratio of RAND_MAX to (RAND_MAX % range), where this probability is high, an alternate method is preferable, but where low, this method is suitable.

Finding Normal Distribution

The normal, or Gaussian Distribution is one often seen in randomly generated natural systems, and as such is an important distribution for generation of random numbers. Random number generators such as rand() however are incapable of producing such a distribution directly, and so the distribution must be converted to a normal distribution. The basic equation for the normal distribution is found in (Eqn: C.1). An important conversion function between white and normal distributions is the Box-Muller transform (Equations: C.2,C.3)[1].

$$y = \frac{1}{\sigma\sqrt{2\pi}} \exp\left(-\frac{(x-\mu)^2}{2\sigma^2}\right) \tag{C.1}$$

$$y_1 = \sqrt{-2 \times \ln(x_1)} \times \cos(2 \times \pi \times x_2) \tag{C.2}$$

$$y_2 = \sqrt{-2 \times \ln(x_1)} \times \sin(2 \times \pi \times x_2) \tag{C.3}$$

However due to the sines, cosines and square roots, this would require a large number of calls to the maths library, slowing the program significantly for large numbers of required random numbers. Instead, the polar form is far more efficient, firstly converting two random numbers between 0 and 1 into an even distribution over a circle, and then generating the output:

```
float tx,ty,r,output;
float rm = float(RAND_MAX);

do
{
        tx = (2.0f*(float(rand())/rm)) - 1.0f;
        ty = (2.0f*(float(rand())/rm)) - 1.0f;
        r = (tx*tx) + (ty*ty);
} while ( r > 1.0f || r == 0.0f);

output =  GaussCenter + (GaussSigma * ty * sqrt ((-2.0f*log(r))/r));
```

Where GaussCenter is the centre of the Normal Distribution and GaussSigma is the RMS value.

Bibliography

[1] G. E. P. Box and M. E. Muller. A note on the generation of random normal deviates. *Ann. Math. Stat.*, page 610, 1958.

C.2 Monte Carlo Grid Sampling

For a 64x64 grid, there are a total of 4096 grid points, each containing 360x90, or 32400 rays. This leads to a significant processor load particularly for larger grids, as the total number of grid points increases rapidly. An alternative to calculating for every grid point, but still retaining the general detail of the grid, is to randomly sample different grid points. Using the methods of random Number Generation described in Appendix C.1, the X and Y locations over the grid were sampled for different numbers of attempts, with the results recorded in Fig: C.1. Taking the whole grid to be the most accurate representation of the Structured substrate, the similarities were compared simply by summing the total emission and finding the ratio.

Sampled Points	Completion Time (hr:min:sec)	Escape Ratio (Sampled:Whole Grid)
1	< 00:00:01	0.845
5	00:00:05	0.834
10	00:00:11	0.939
50	00:00:55	0.997
100	00:01:55	1.003
all	01:15:00	1

Table C.1: Analysis of Different Numbers of Sampled Grid Points

As we can see, one of the most prominent differences is in the relative strengths of the different peaks. As the device is described as a simple 2x2 prism with the central point as a raised point, and this structure repeated over the entire device, these differences are due to the different numbers of samples of each of the four squares describing the prism. As the sample number is increased, the fluctuation in this sample number becomes small compared to the total number of times the prism is sampled, however, the larger the surface structure features, the more prominent this effect (Fig: C.2 but again, as the number of samples increases, this distortion diminishes.

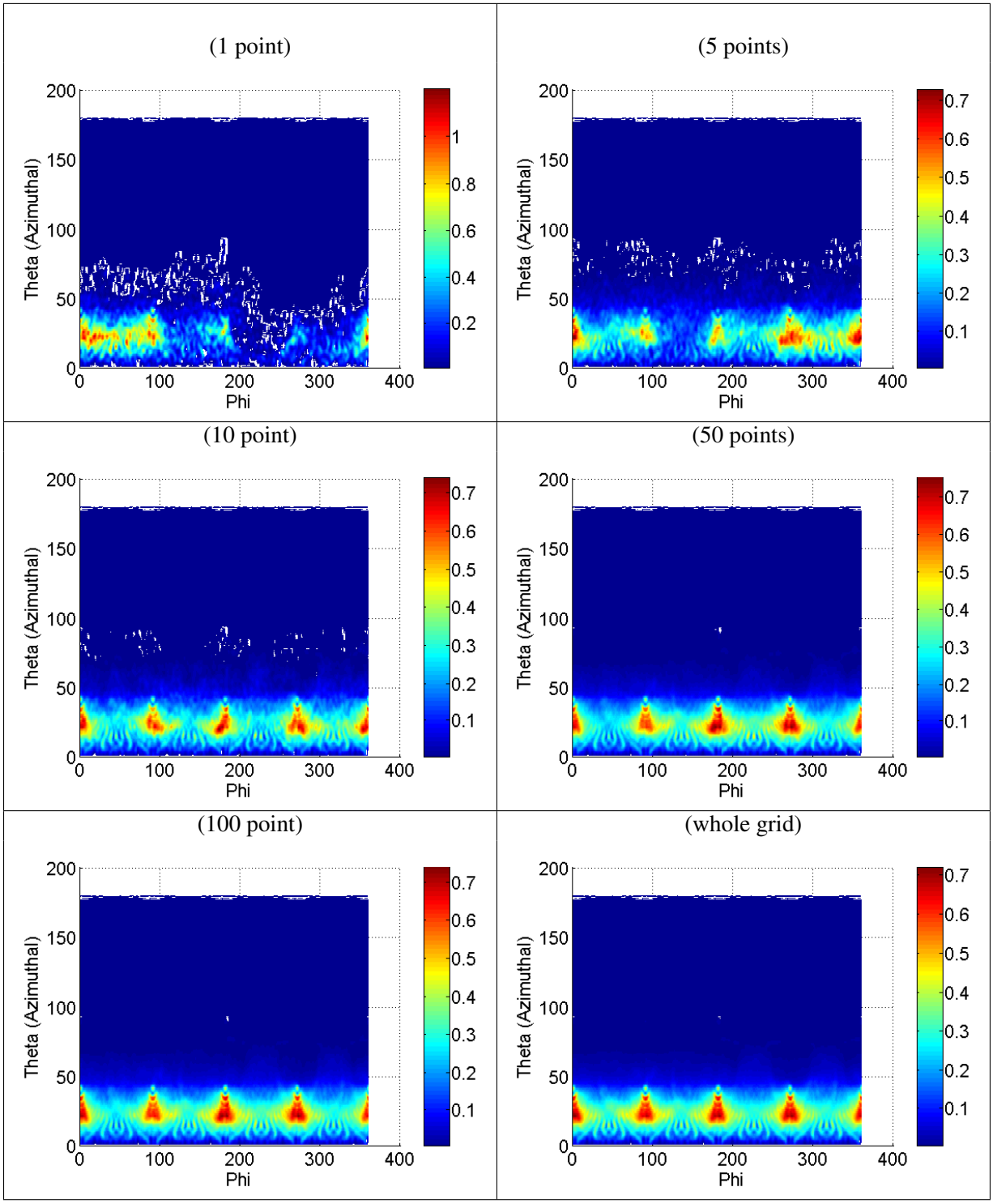

Figure C.1: Angular output for different numbers of sampled grid points.

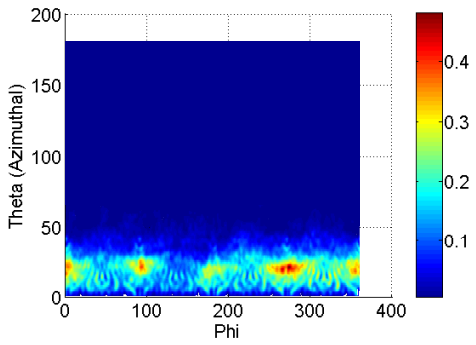

Figure C.2: 4x4 square pyramid with 10 sampled points.

Appendix D

Images and License Information

Several images and graphs in the course of this work were taken from http://www.wikipedia.com. All images submitted to Wikipedia are public domain, and the submitter has agreed to the following terms (available on Wikipedia)

I, the author of this work, hereby release it into the public domain. This applies worldwide.

In case this is not legally possible:

I grant anyone the right to use this work for any purpose, without any conditions, unless such conditions are required by law.

Appendix E

Acronyms

E.1 Common Acronyms

CCD	Charge Coupled Device
CRT	Cathode Ray Tube
CIE	Commission Internationale L'Eclairage
HDTV	High Definition Television (modern international television standard)
LCD	Liquid Crystal Display
LED	Light Emitting Diode
NTSC	National Television Standards Committee (US and Asia television standard)
OLED	Organic Light Emitting Diode
PAL	Phase Alternating Line (European television standard)
TFT	Thin Film Transistor

E.2 Common Chemical Acronyms

Alq_3 aluminum tris(8-hydroxyquinoline)

ITO Tin doped Indium Oxide

YAG Yttrium Aluminium Garnet

ZAO Aluminium doped Zinc Oxide)

Appendix F

Important Definitions

Basic Definitions

- Lambertian: A Lambertian emitter is one for which the luminance of the emitter is the same regardless of viewing angle.
- Radiometry: Radiometry is related to the measurement of light, especially that in the visible region of the Spectrum. Unlike Photometry it does not take into account the response of the eye, and focuses purely on the direct analysis of the electromagnetic energy.
- Photometry: Photometry is the measurement of the visual aspect of light, taking into account the response of the human eye to the different wavelengths of light.

Units

Basic Units

- Nit: a nit is a non SI unit of luminance. It is equal to one Candela per square metre ($1\ cd \cdot m^{-2}$)
- Steradian: The Steradian is the SI unit of solid angle, and is the 3D equivalent of the 2D

Radian. It is defined as the solid angle subtended at the centre of a sphere of radius r, by a portion of the sphere having area r^2

- Watt: One Joule of energy per second ($J \cdot s^{-1}$)

Radiometric Units

- Radiance: The Radiance is the power per unit solid angle per unit projected source area. Radiance is measured in watts per steradian per square metre ($W \cdot sr^{-1} \cdot m{-}2$) and is also the spectral radiance integrated over all wavelengths.

- Radiant Intensity: The radiant intensity is the power of the source measured in Watts per steradian ($W \cdot sr^{-1}$)

- Spectral Radiance: The Spectral Radiance is the power per solid angle per unit projected source area per Herz: It is commonly measured as ($W \cdot sr^{-1} \cdot m{-}2 \cdot nm{-}1$)

Photometric Units

- Candela: The candela is the unit of luminous intensity of a source which, in a given direction emits monochromatic light of frequency $540x10^{12}$ Hz with a radiant intensity of 1/683 watts per steradian. The frequency chosen is the peak frequency of the human eye, and the 1/683 term is an arbitrary number chosen to maintain consistency with the defunct definition of the candela.

- Luminance: Luminance describes the amount of light emitted from a particular area. It is a photometric measure of the density of luminous intensity in a given direction. the SI units for luminosity are candelas per square metre $cd \cdot m^{-2}$

- Luminous Flux: Using the 1931 CIE Photopic Luminosity Function, which converts radiant

energy into luminous (visible) energy, the luminous flux can be calculated as in formula F.1

$$L = 683.002 \int_0^{\infty} \bar{y}(\lambda)\, J(\lambda)\, d\lambda \tag{F.1}$$

where $\bar{y}$ is the numerical standard luminosity function (Fig: (F.1[1]) and $J(\lambda)$ is the spectral intensity of the radiation.

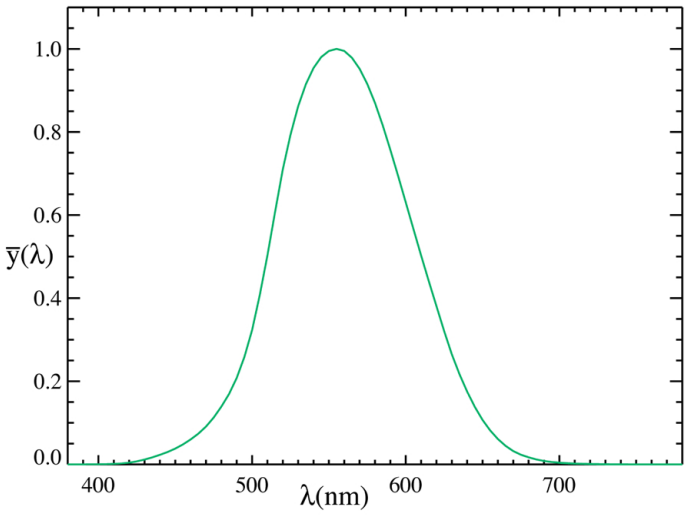

Figure F.1: The 1931 CIE Photopic Luminosity Function

- Luminous Intensity: The Luminous Intensity is a measure of the perceived power emitted by a source in a particular direction. Since the perceived power by the human eye varies with wavelength, the Luminous intensity for different frequencies will change even if the radiant intensity remains the same.

[1]Image obtained from http://www.wikipedia.com. Further info in Appendix D